LRP 738/02 November 2002

Papers Presented at the

19th IAEA Fusion Energy Conference

Lyon, France, October 14 - 19, 2002

available in colour on the web at
http ://crppwww.epfl.ch/conferences

ISSN 0458-5895

LIST OF CONTENTS

An Overview of Recent Results from the TCV Tokamak

T.P. Goodman 1), S.M. Ahmed 1), S. Alberti 1), Y. Andrèbe 1), C. Angioni 2), K. Appert 1), G. Arnoux 1), R. Behn 1), P. Blanchard 1), P. Bosshard 1), Y. Camenen 1), R. Chavan 1), S. Coda 1), I. Condrea 1), A. Degeling 1), B.P. Duval 1), P. Etienne 1), D. Fasel 1), A. Fasoli 1), J.-Y. Favez 1), I. Furno 3), M. Henderson 1), F. Hofmann 1), J.-P. Hogge 1), J. Horacek 1), P. Isoz 1), B. Joye 1), A. Karpushov 1), I. Klimanov 1), P. Lavanchy 1), J.B. Lister 1), X. Llobet 1), J.-C. Magnin 1), A. Manini 2), B. Marlétaz 1), P. Marmillod 1), Y. Martin 1), An. Martynov 1), J.-M. Mayor 1), J. Mlynar 1), J.-M. Moret 1), E. Nelson-Melby 1), P. Nikkola 1), P.J. Paris 1), A. Perez 1), Y. Peysson 4), R.A. Pitts 1), A. Pochelon 1), L. Porte 1), D. Raju 5), H. Reimerdes 6), O. Sauter 1), A. Scarabosio 1), E. Scavino 1), S.H. Seo 1), U. Siravo 1), A. Sushkov 7), G. Tonetti 1), M.Q. Tran 1), H. Weisen 1), M. Wischmeier 1), A. Zabolotsky 1), G. Zhuang 1)

1) Centre de Recherches en Physique des Plasmas, Association EURATOM - Confédération Suisse, Ecole Polytechnique Fédérale de Lausanne, CH-1015 Lausanne, Switzerland
2) Max-Planck-Institute für Plasmaphysik, Garching bei München, Germany
3) Los Alamos National Laboratory, USA
4) DRFC-CEA Cadarche, France
5) Institute for Plasma Research, Bhat, Gandhinagar-382 428, Gujarat, India
6) General Atomics, San Diego, USA
7) RRC Kurchatov, Moscow, Russia

e-mail contact of main author: Timothy.Goodman@epfl.ch

Abstract. The TCV tokamak (R=0.88 m, a < 0.24 m, B < 1.54 T) program is based on flexible plasma shaping and heating for studies of confinement, transport, control and power exhaust. Recent advances in fully-sustained off-axis electron cyclotron (EC) current drive (CD) scenarios have allowed the creation of plasmas with high bootstrap fraction, steady-state reversed central shear and an electron internal transport barrier. High elongation plasmas, $\kappa = 2.5$, are produced at low normalized current using far off-axis EC heating (ECH) and ECCD to broaden the current profile. Third harmonic heating is used to heat the plasma center where the second harmonic is in cut-off. Both second and third harmonic heating are used to heat H-mode plasmas, at the edge and center, respectively. The ELM frequency is decreased by the additional power but in separate experiments can be controlled by locking to an external perturbation current in the internal coils of TCV. Spatially resolved current profiles are measured at the inner and outer divertor targets by Langmuir probe arrays during ELMs. The strong, reasonably balanced currents are thought to be thermoelectric in origin.

1. Introduction

Stable plasmas in which all of the current was driven by electron cyclotron current drive (ECCD) were first obtained in TCV (Tokamak à Configuration Variable) in 1999 [1]. Subsequently, 2.0s plasmas of up to 210kA were fully sustained using the complete installation of six, 82.7 GHz, 0.5 MW, 2.0 s gyrotrons coupling to the second harmonic X-mode (X2) [2]. In an extension of earlier results [3, 4], two pairs of gyrotrons operated in succession produced stable, 100kA, 4s discharges.

It was shown that when ECCD was concentrated at the plasma center, the plasma pressure and current profiles which resulted were unstable to ideal MHD modes. The modes appeared as the current profile relaxed to the new shape determined by the ECCD source. When the power was increased using additional gyrotrons, it was necessary to broaden the deposition profile to ensure stability. This deposition broadening resulted in a lower overall efficiency as more of

the power was deposited in regions of lower temperature, higher trapping and therefore lower efficiency [1, 2].

All of the ECCD experiments benefit to a certain extent from relatively low density (at the absorption location) due to the associated increase in current drive efficiency; as long as absorption is still completed on one side of the cold resonance and far enough from the trapped-passing boundary. The cut-off density for X2 is just over $4 \cdot 10^{19} [m^{-3}]$. Thus, for the purposes of this paper, the operational space of TCV can be crudely divided into regions of low and high density; referring to the accessibility of the X2 heating system to the plasma center. There is a smooth transition from one to the other, however, since X2 can be used at the plasma edge where the density remains low enough to allow access to the resonance.

The recent completion of the third harmonic X-mode heating system (X3), consisting of three, 118GHz, 0.5MW, 2.0s gyrotrons, has allowed operation with centrally deposited ECH in the higher density regime for the first time on TCV. Ohmic ELMing H mode studies are now extended to additionally heated discharges. In this paper, sections 2-5 deal with the lower density regime and 6-7 with the higher density regime (both Ohmic and additionally heated plasmas).

2. Scenarios Externally Sustained by Off-axis ECCD

Fully sustained ECCD driven plasmas are created by injecting co-ECCD into the current flattop of an established Ohmic plasma. After 20ms, the transformer coil current, I_{OH}, is feedback controlled at a constant current thereby precluding an external source for the inductive electric field in the plasma. The current in the shaping coils are constant in all cases of interest. Under these conditions, the total ECCD driven current is easily measured. Following the method described in Ref. 4, the derived ECCD current I_{CD} is found by subtracting the bootstrap current I_{BS} from the total plasma current, I_p.

The fully sustained ECCD driven results have now been extended to plasmas which are fully sustained only by *off-axis* co-ECCD. The non-inductive current profiles are broadened by radial diffusion of the fast particles so that some central current is still present. The off-axis deposition creates enough bootstrap current to produce a q-profile with reversed shear in the center. With the addition of counter-ECCD in the center, steep, wide, electron internal transport barriers (eITBs) are created with a subsequent increase in the bootstrap fraction to >50% [5]. The current profile is only determined by the gyrotron beam aiming, which defines the current drive and bootstrap current drive which is itself determined by the pressure profile resulting from the deposition profile and the shear dependent transport. We have obtained stable discharges lasting longer than $500\tau_E$ and 10 current diffusion times which have positive additional-power scaling for the central counter-ECCD. In general, TCV plasmas follow Rebut-Lallia-Watkins (RLW) scaling [6, 7] and we report confinement improvements relative to this value H_{RLW} [8, 9]. For these ITBs, $H_{RLW} = 4$ which is ~ 1.6 times ITER L-mode scaling. The following three subsections deal with the three important features of this scenario: *1)* radial diffusion of fast particles and the ECCD current profile, *2)* the bootstrap current, total current and resulting safety factor profiles, and *3)* the improved confinement of the eITB.

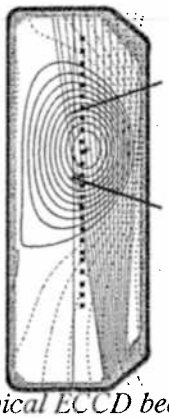

*FIG. 1. Typical ECCD beam aiming for off-axis ECCD (red, green lines), Thomson scattering measurement points (red *) and Hard X-ray camera chords (cyan lines).*

2.1. Current-Carrying Fast-Electron Diffusion

2.1.1. Direct Evidence of Fast-Electron Diffusion

An energy-resolved, multi-chord, Hard X-ray pinhole camera [10], on loan from CEA-Cadarache, is installed on the bottom of TCV. The 14 viewing chords pass vertically through the outer half of the plasma (FIG. 1). The measured photon temperature is nearly constant across the poloidal section, whereas the Abel-inverted emissivity peaks in the center (FIG. 2). Thus, direct evidence [11] for radial diffusion of fast electrons is provided by the hard X-ray camera as the beams do not pass through the plasma center and therefore cannot directly generate the fast population at that location. Measurements from the high field side, 24-channel, electron cyclotron emission (ECE) radiometer, operating in the 78-114 GHz range, are also sensitive to the fast electron population and, in conjunction with the hard X-ray results, are consistent with a suprathermal electron density of up to 25% of the total electron density [12]; derived using a bi-maxwellian temperature model.

2.1.2. Calculating the driven current

The magnitude of the driven current determined by linear calculations (e.g. TORAY-GA [13] or CQL3D [14] at artificially low power) is generally one to three times smaller than the measured (see below) driven current. Previous calculations of the current drive using the TORAY-GA ray-tracing code coupled to the quasi-linear Fokker-Planck code CQL3D, overestimated the driven current by an order of magnitude.

Diffusion and density conserving advection of the current-carrying fast electrons in physical space has been included in CQL3D with the diffusion coefficient as a free parameter [15], constrained by the experimental ECCD current, discussed above. Several models for the dependence of the diffusion on velocity have been studied: $D \propto v^{\alpha}$ with $\alpha = -1,0,1$ [16]. The details of the resulting electron velocity distribution function are different in each case. However, the particles which carry the largest part of the current generally have a velocity ~ $5\text{-}6v_{thermal}$ and for these particles, the diffusion coefficients are within a factor of three of each other for all of the models – typically 3-5 m^2/s [5]. Hard X-ray measurements place a lower bound of 1.5 m^2/s on D [11].

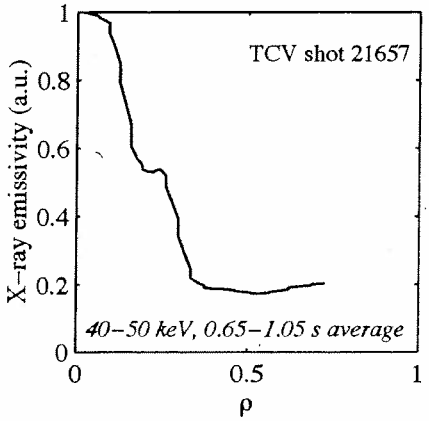

FIG. 2. Time-averaged, Abel inverted hard X-ray emission profile during 1 MW of off-axis co-ECCD; showing central emission at photon energies >40keV (T_e bulk ~ 2.7keV).

The most important consequence of diffusion is that the ECCD current profiles j_{CD} are typically flattened (or slightly hollow) towards the axis in contrast to the power deposition which is peaked off-axis. The total driven current is then, by choice of the free parameter, consistent with the measured plasma current after accounting for the bootstrap current.

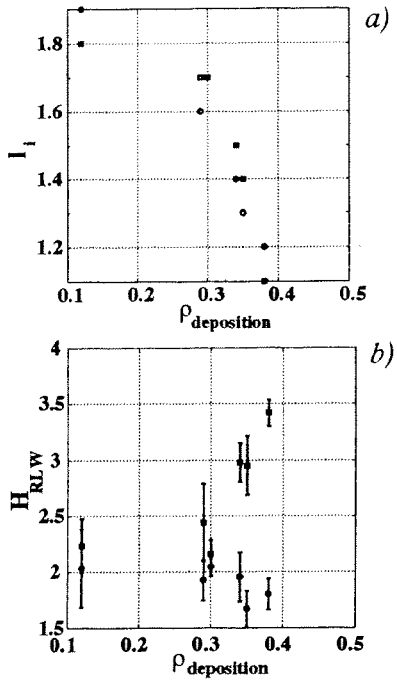

FIG. 3. a) Internal inductance decreases and b) H_{RLW} increases as the co-ECCD deposition is moved further off axis. Red points are before the addition of central counter-ECCD; blue points, after.

2.2. Importance of the Bootstrap Current

The electron temperature and density are measured by Thomson scattering at 25 points along a vertical chord in the TCV vessel (FIG. 1) every 50ms, for these discharges. The bootstrap current is calculated from the T_e and n_e profiles assuming steady state conditions [4]. The justification for this assumption is the observation that the reconstructed equilibrium parameters (e.g. internal inductance l_i and elongation κ) no longer evolve in time after a few 100ms.

During the first few 100ms of the ECCD, the power deposition is only off-axis, the density and temperature profiles tend to be flat in the plasma center, and the bootstrap current profile j_{BS} is peaked off-axis – amounting to ~20-25% of the total current. The combination of the flattened j_{CD} and j_{BS} leads to a hollow total current profile j_{TOT}. The calculated current profile and measured pressure profile is then input to the CHEASE equilibrium code to calculate the steady-state q-profile.

If the ECCD deposition is moved further off-axis, the steady-state internal inductance is reduced (FIG. 3a) and the pressure profile broadened. For deposition $\rho \equiv \sqrt{V_\psi / V_a} \approx 0.3$, where V_ψ is the volume inside a given flux surface and V_a the plasma volume, the plasmas begin to show evidence of improved confinement (H_{RLW} ~ 3.5) when power from an additional gyrotron is later added near the center (FIG. 3b). As the j_{CD} profiles are not peaked off-axis, this result shows that it is the bootstrap current that plays the key role in the ITB formation.

2.3. Steady State Electron Internal Transport Barrier

It has been shown [17, 18] that there is a gradual improvement in the H_{RLW} for these plasmas as small amounts of counter-ECCD are added near the center in order to increase the safety factor on axis. Excessive counter-ECCD leads to a disruption but, by adjusting the central launch angle, the plasma can be maintained just below the MHD stability limit. Figures 4a,b show the j_{CD}, j_{BS} and j_{TOT} profiles before (dashed curves) and after (solid curves) addition of counter-ECCD in the center and the resulting q-profile (after). The bootstrap current fraction is ~50% in this steady state discharge lasting ~$200\tau_{Ee}$ with ~ 1.6 times ITER L-mode scaling. At

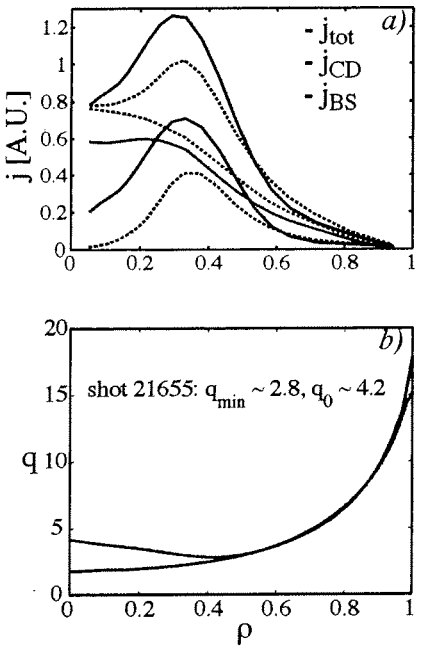

FIG. 4. a) CQL3D calculated j_{CD}, j_{BS} and j_{TOT} before (dashed) and after (solid) additional central counter-ECCD. b) The q-profile calculated by LIUQE (blue) and CHEASE (red).

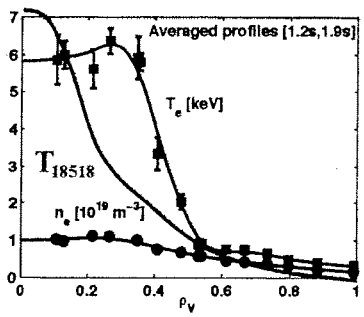

FIG. 5. Temperature profile in the ICEC (green - scaled with power) to the fully sustained, off-axis ECCD with central counter ECCD (red).

present, electron-ion coupling is low and $T_e/T_i \sim 20$ [19,18]. When the density is increased for this scenario, the current drive efficiency decreases but the bootstrap current, and especially the bootstrap fraction, increases [5].

3. The Improved Core Electron Confinement (ICEC) regime

In inductive discharges, stable regimes of improved core energy confinement were achieved ($H_{RLW} = \tau_E / (\tau_{E\ RLW})$ ~3.5) with and without sawteeth [8, 9] by a combination of off-axis ECH followed by central counter ECCD. PRETOR–ST, a1–1/2D transport code including a sawtooth crash model [20, 21], accurately simulates the measured electron temperature profiles in these discharges and indicates that the central shear is reversed [9]. The code successfully predicted that a 10% displacement of the central counter-ECCD would lead to a loss of the reversed shear and high confinement regime [3, 4]. This regime has narrower good confinement regions due to the natural peaking of the profiles caused by the residual electric field. Figure 5 shows a comparison between the ICEC regime and the off-axis driven ITBs described in section 2, above. In the ITB case, the temperature profile is wider and the foot of the barrier (where the temperature begins to deviate after the addition of the central counter-ECCD) is at larger ρ [18]. This results in a larger plasma volume in which the confinement is improved as well as the larger bootstrap fractions discussed above. Although most recent work has been carried out on the off-axis ITBs, a comparison of the two regimes should allow subtleties of non-maxwellian, hot conductivity induced enhancement of the current drive efficiency [22] to be addressed [4]. In addition, the ICEC regime yields better τ_{Ee} as I_p and n_e are larger.

4. Understanding the Control of The Sawtooth Instability

In sawtooth control experiments, 1.3MW of EC power deposited outside the q=1 produces sawtooth stabilization. To find the optimum location for stabilization, 3 gyrotron beams are swept across the region of the q=1 surface and the maximum sawtooth period is found. This technique is used to align each of the 6 independent EC launchers relative to each other to within ±3mm i.e. ~1% of the minor radius [23]. The addition of 0.45MW of EC power deposited at an optimum location just inside q=1 then destabilizes the sawteeth [21]. This demonstrates that ECH may be able to destabilize the long-period sawteeth predicted in burning plasmas.

The sawtooth period and optimum locations for stabilization and destabilization are simulated successfully [21,24] with PRETOR-ST. In experiments, current drive is always accompanied by heating. The effects of heating and current drive can be separated in the simulations which is especially useful for understanding counter-ECCD where competing effects are at play [21]. The methodology used to find both the maximum or minimum in sawtooth period is the same in the code and in the experiments: the beams are swept in order to find the optimum location.

The sawtooth model is successful in showing that the optimum for stabilization is clearly outside the q=1 surface, in agreement with the experiments, and that the minimum is inside (for the conditions of the experiment see Ref. 21). The accuracy of the simulation appears quite high; the difference between the simulated and measured sawtooth period maximum is 3% in

ρ. Nevertheless, this difference is significant given the ~1% precision in launcher alignment. The accuracy of the results depends directly on the proper knowledge of the geometry of the launchers, plasma position and on the ray-tracing. The estimated accuracy in the geometry is of the same order as the simulations. The consequence is that it is not yet possible to *predict* the fixed launching angles of the beams that would be necessary to ensure optimum stabilization of the sawteeth: sweeps are a necessity. On the other hand, the optimum for destabilization is significantly broader in ρ and may not be as difficult to predict.

An alternative methodology (similar to [4]) could be applied by assuming that the modeling has the highest accuracy then, re-calibrating the launching geometry accordingly. It would still be necessary to determine whether the launchers or the magnetic reconstruction are in error.

5. The Link between Classical and Neoclassical Tearing Modes [25]

The theoretical dependence of Δ' on island width has been confirmed in experiments in which strong central ECCD modified the Ohmic current profiles of low density discharges, leading to a tearing mode with two distinct growth phases. The tearing mode appears on a current diffusion time scale and is driven unstable by the current profile. After growing to a sufficient width, it exceeds the critical island width for rapid growth of the neoclassical tearing mode. When the ECCD is switched off the island width decreases, first on a confinement and then a resistive diffusion time scale. These results unify the theory of classical and neoclassical tearing modes and therefore, the island width evolution is well modeled using the modified Rutherford equation.

6. Type-III ELMy H-modes on TCV

With additional heating on TCV, it has been shown that the ELM frequency decreases with increasing power. This is typically taken as one of the characteristic differences between type-III and type-I ELMs [e.g. 26]. Therefore the ELMs discussed below are referred to as type-III ELMs.

The transition from L-mode to ELM-free or type-III ELMy Ohmic H-mode has been studied statistically using the 'mobile centers method'. Ranges of plasma current, density, elongation, triangularity and plasma-wall distance have been determined in which it is possible to pass reliably into the ELMy H-mode. Once the ELMy H-mode is entered through this 'gateway', the plasma parameters can be varied within a significantly wider range while maintaining the ELMs. [27]

Unstable periodic orbits (UPO) in the ELM time series have been observed showing that a deterministic, chaotic process governs the apparently random distribution of the delay between ELMs on TCV [28]. These results imply that any valid theoretical model for type-III ELMs must account for the existence of UPOs. Statistical analysis of ELM and sawtooth periods indicates frequent synchronization of the ELM to half, equal, double or triple the sawtooth frequency, depending on the elongation [29].

6.1. Divertor Target Currents During Type-III ELMs

Arrays of single Langmuir probes embedded in central column and floor graphite protection tiles and biased at zero voltage provide high spatial and temporal resolution of currents that flow to the inner and outer divertor targets during ELMing phases of single null lower (SNL)

Ohmic H-modes. Many of these discharges are characterized by long phases of extremely regular Type III ELMs, permitting a coherently averaged ELM current to be generated at each probe using the peak of the signal of a vertical viewing D_α chord at each ELM to define the zero time reference. Careful choice of the averaging period (~ 4ms for a 200Hz ELM frequency) around each ELM ensures that each is unaffected by the preceding or following event. Standard TCV operation uses positive plasma current and toroidal field, with the latter defining the ion ∇B drift direction away from the X-point for SNL equilibria. The coherent ELMs in FIG.s 6a-c show that near the strike points, large negative and positive currents flow to the inner and outer targets respectively, with the currents reaching peak values at the peak of the D_α recycling signal intensity. These currents are comparable in magnitude to the ion saturation current - the maximum current that can flow to the grounded tiles.

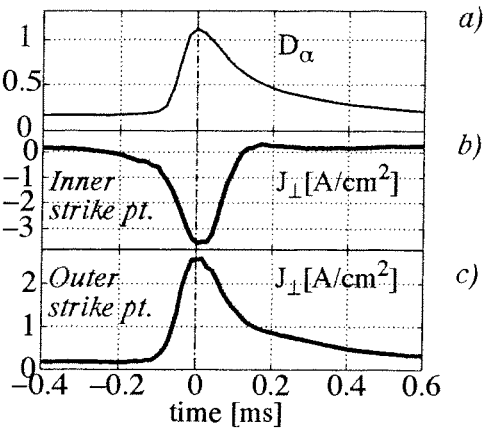

FIG. 6. Coherently averaged ELMs for D_α (a) used as the reference timing trace and perpendicular target current near the strike point at the inner (b) and outer (c) targets.

Figure 7 shows a selection of perpendicular target current profiles mapped to the outside midplane of the equilibrium and plotted as a function of distance from the separatrix for a selection of time intervals before, during and after the coherent ELM. Reasonable current balance is obtained during the ELM itself across most of the profile. The persistent, localized and unbalanced negative current feature appearing very close to the strike point at the inner target before and after the ELM is of the expected sign for a parallel current driven by the effects of the ∇B drift and the up-down asymmetry of plasma pressure. During the ELM, the broad parallel current profile is believed to be thermoelectric in origin. In L-mode, at the relatively low plasma densities common to the H-mode ELMing phase studied here, the unfavorable ∇B drift direction leads to strong in/out asymmetries in the divertor plasma parameters, with the inner target generally hotter than the outer. Though fast T_e measurements cannot be made during the ELM event itself, if the hot electrons expelled by the ELM were to accentuate the in/out T_e asymmetry, an electron thermocurrent would be expected to flow from the colder outer target to the hotter inner target. The experimental currents in FIG.s 6,7 do indeed flow in this direction. Integrating the profiles radially and toroidally yields total perpendicular target currents ~2-3 kA – of the order of 0.7% of the plasma current.

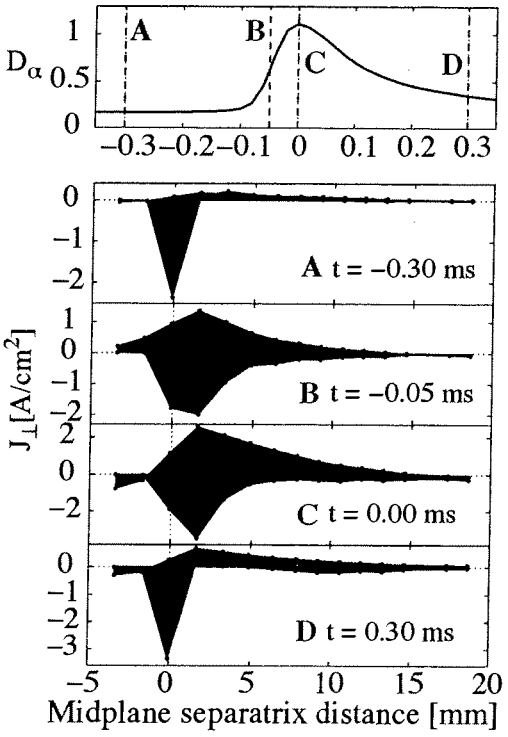

FIG. 7. Profiles of perpendicular target currents mapped to the outside magnetic midplane at various times during the coherent ELM (marked as A-D on the coherent D_α trace at top). Strong and reasonably balanced currents flow at all locations during the ELM.

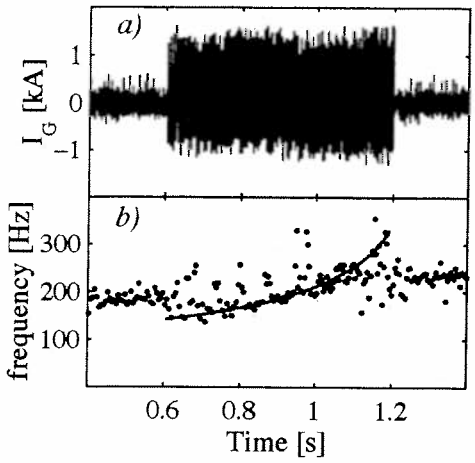

FIG. 8. a) Perturbation creating vertical motion (~±3mm) to the feedback controlled vertical stability coil current I_G. b) Frequency tracking of the ELMs (blue dots) to the drive frequency (red line).

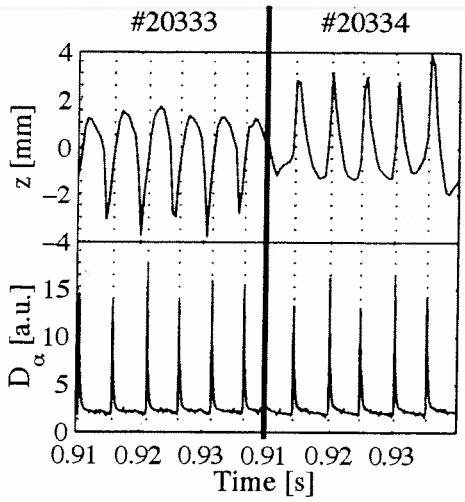

FIG. 9. Triggering of the ELM (lower traces) by the upward vertical motion (upper traces) for two shots with opposite polarity of the driving perturbation.

6.2. ELM Frequency Controlled by Vertical Plasma Motion

The ELM frequency has been experimentally locked to a modulation of the fast coil current inside the TCV vessel which was swept in frequency [30]. A 2 ms, single-cycle, square-wave voltage perturbation is used to drive a current in the internal fast coils. The resulting current pulse is roughly triangular and is added to the regular feedback control loop used to stabilize the vertical position. The additional perturbation induces a vertical motion of the plasma up to ±2-3 mm. The pulses are repeated at a swept frequency close to the natural ELM frequency of approximately 200Hz. When the amplitude is small, the phasing between the perturbation and the ELMs scrolls continuously as the frequency is swept from 143 Hz to 333 Hz over 0.6 seconds. Increasing the amplitude of the perturbation causes the ELM frequency to track the frequency of the vertical perturbations. Figure 8 shows that the ELM frequency can be both reduced or, more importantly, increased. It is also observed that during tracking, ELMs are triggered on the upward vertical motion independent of the polarity of the voltage pulses which are used to cause the perturbation. That is, if the phase of the single cycle square wave is shifted by 180°, the ELMs still occur when the plasma is moving upwards (FIG. 9). The asymmetry in the poloidal field for lower single-null diverted plasmas is such that an upward vertical motion corresponds to an induced current at the edge in the same direction as the plasma current.

6.3. ELM Frequency Modification with Additional Heating

6.3.1. Edge Heating with X2

ELMing Ohmic H-mode plasmas with central density of $n_{e0} = 1.5 \cdot 10^{20} m^{-3}$ have been heated using X2. The density cutoff of the X2 is reached near the edge of the plasma ($\rho > 0.9$) and the refraction is very strong. The heat is localized at the plasma edge and amounts to only ~40% of the beam power – the rest being absorbed or lost after multiply reflections from the inner wall of the vacuum chamber. The X2 power pulses were, therefore, kept short. The ELM frequency decrease from 200 ±40 Hz without ECH, to 140±40Hz with 0.45 MW of injected

power. Because of the large refraction this scenario is technically undesirable.

6.3.2. Central Heating with X3 [31]

A 3-gyrotron, 1.5MW, 118GHz, 2.0s third harmonic electron cyclotron resonance heating system (X3) has been installed, commissioned and brought into operation on TCV [32]. It has been used to heat plasmas at densities up to $10^{20}m^{-3}$, far exceeding the cut–off density of the X2 system. The X3 system therefore significantly extends the operational parameter space of TCV and allows additionally heated H-mode plasmas to be studied [33].

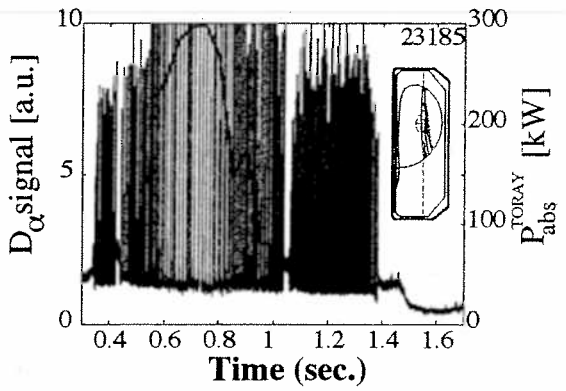

FIG. 10. The ELM frequency of the D_a signal (blue) is seen to decrease when the X3 power (red) is well absorbed during a mirror sweep. The inset shows the central ray of the beam at different times during the mirror sweep.

The X3 power is launched into TCV from the top and takes advantage of the longer path length along the resonance, especially at high κ, to compensate for the low optical depth at the third harmonic frequency. In fact, in the presence of the non-maxwellian electron distribution functions generated by X2 ECCD, it has been shown that 100% absorption can be obtained even when launching from the LFS [34]. The disadvantage of launching from the top is that the absorption is very sensitive to the injection angle and refraction. Feedback will be required to maintain the optimum heating angle. On the other hand, the launching mirror can be offset in major radius to allow incidence on the resonance from either the high or low field side. This feature should allow selective absorption on different energy regions in the electron distribution function.

ELMy H-mode plasmas with central density of $n_{e0} = 0.7 \cdot 10^{20}m^{-3}$ have been heated using up to 0.85MW (2 gyrotrons) of X3 power. Figure 10 shows the D_α time trace and the absorption of power from one X3 gyrotron, calculated by the TORAY-GA ray-tracing code, during a sweep of the launching mirror. The ELM frequency is seen to decrease as more power is absorbed and then increase again as the absorption drops due to non-optimum aiming. At the optimum angle, the absorption reaches 70%. When 0.85MW is injected at the optimum launcher angle, the ELM frequency decreases, an ELM free period ensues, a more global instability occurs which reaches the plasma center and the plasma returns to L-mode before terminating in a disruption. This can be prevented using the natural tendency of the ELM frequency to increase with decreasing density to counteract the frequency decrease with increasing power. A pre-programmed density decrease maintains the ELMy H-mode throughout the ECH pulse.

7. Extended High-κ Scenarios with ECH/ECCD

Advances have been made using both the X2 and X3 current drive / heating systems in highly shaped discharges. The aim of these experiments is to explore the region of β, I_N parameter space ($I_N = I \cdot a/B$ where I is the plasma current, a is the minor radius and B is the toroidal field) in which the so-called beta limit and current limits meet at high elongation [35]. By increasing the elongation, the current can be increased and I_N increases. The so-called current limit (q=2) is modified with elongation in such a way that it is necessary to reduce the current to obtain the

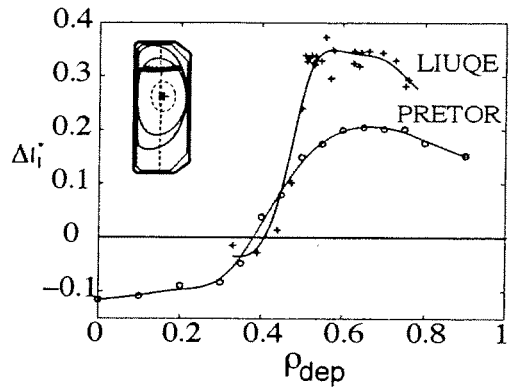

FIG. 11. Measured (blue) and calculated (red) change in the internal inductance due to ECH induced profile broadening. The inset shows two time slices of a typical shot with κ increasing due to far off axis ECH (colors are aribitrary).

highest possible beta. With Ohmic heating only the current limit has been reached [36] at low q and high κ, but it is not possible to reach the highest β–limit without additional heating. In high elongation discharges, the theoretical β-limit reaches a maximum at $I_N \sim 2$MA/mT. Thus, high elongation operation is required at lower plasma currents. This renders the high elongation plasma more vertically unstable. Current broadening with far off-axis X2 ECH/ECCD improves the stability at high κ and lower normalized current I_N.

7.1. Far Off-axis X2 heating and current drive

Plasma operation with $I_N \sim 2$MA/mT imposes technical limits on X2 accessibility in TCV due to high density and subsequent strong refraction of the beams; especially those launched near the plasma equator (2 beams) [37]. On the other hand, for efficient elongation of the plasma by current profile broadening with far-off axis X2, it is desirable to increase the density thereby maintaining high X2 absorption even when depositing nearer the plasma edge. The equatorial beams are then not usable due to refraction.

At present, highly elongated plasmas ($\kappa \sim 2.5$) with a high safety factor ($q_{edge} \sim 12$) and lower current ($I_p \sim 390$ kA, $I_N = I_p/aB = 1.03$ MA/mT) have been created using 1.35MW of far off-axis ECH [38] from 3 upper lateral launchers. The most efficient X2 heating location for current profile broadening has been determined [38] as shown in FIG. 11.

The magnitude of the change in internal inductance Δl_i^* achieved when far off-axis X2 heating is added to an Ohmic plasma (relative to the change in l_i that would be expected for the equivalent κ without heating) is plotted as a function of the deposition location, ρ_{dep} (blue curve: LIUQE). Positive Δl_i^* indicates an increase in κ with additional heating and negative Δl_i^*, a decrease. The plasma current is kept constant by feedback control and the shaping fields are also constant: the change in elongation is a result of the ECH generated profile broadening. The PRETOR transport code and DINA free-boundary evolution code calculations [39] (using the ECH heating profiles determined by TORAY-GA as additional input) show good agreement with the experiments. Both curves roll over when deposition is too far off axis. This is thought to be due to the increasingly poor confinement at large ρ. Adding either co- or counter-ECCD helps increase the efficiency of elongation [38]. The symmetry of this situation is under investigation but may be due to strong trapping effects (accentuated at large ρ). The operational space can be increased towards higher β by combining far off-axis X2 heating with central X3 heating.

7.2. Central Heating with X3

As in H-mode plasmas, the X3 system is essential for central heating of high density plasmas. The high κ increases the absorption depth yielding reasonable first pass absorption. The deposition profile is nevertheless broad. When central X3 is added to the plasmas elongated by far

off-axis X2 the current profile peaks as the central conductivity increases. By introducing an ECCD component to the X2 beams, suprathermal electrons are created which enhance the absorption of X3 [40] in a way similar to the earlier LFS X3 experiments [21]. As in the case of fully ECCD plasmas, the difference between Thomson scattering temperatures and ECE temperatures, as well as the localization of the emission during X3 modulation, indicates direct absorption of the X3 on the suprathermal population [40]. Up to 100% X3 absorption has been measured during top-launched, modulated X3 ECH experiments using the diamagnetic loop to measure the accompanying modulation of the stored plasma energy as in [21].

Before further advancing towards the β-limit, it is necessary to optimize the X3 heating scenario to avoid current peaking. To this end feed forward elongation control is used to help maintain the broadened profile when X3 is added [40].

8. Outlook

The development of fully sustained, steady state, eITB operation at high bootstrap fraction opens the way to full sustainment of the current using 100% bootstrap fraction. Investigation and control of ELMing H mode plasmas with electron heating can now be persued using the 1.5MW X3 heating system. The flexible, dual frequency, heating system of TCV can selectively excite different portions of the electron velocity distribution providing an ideal testbed for the study of ECCD physics, fast particle diffusion, thermal transport modelling and MHD instability control.

Acknowledgement: This work is partly supported by the Swiss National Science Foundation.

9. References

[1] SAUTER, O., et al., Proc. of the 26th EPS Conf. on Plasma Phys. and Control. Fusion, Maastricht, 1999, [ECA **23J** (1999) 1105], http://epsppd.epfl.ch/Maas/web/pdf/p3041.pdf; SAUTER, O., et al., Phys. Rev. Lett. **84** (2000) 3322.
[2] CODA, S., et al., Plasma Phys. Control Fusion **42** (2000) B311.
[3] GOODMAN, T.P., TCV Team, in Fusion Energy 2000 in (Proc. 18th Int. Conf. Sorrento, 2000), IAEA, Vienna (2001) CD-ROM file EXP4/09 and http://www.iaea.org/programmes/ripc/physics/fec2000/html/node1.htm.
[4] SAUTER, O., et al., Phys. Plasmas **8** (2001) 2199.
[5] GOODMAN, T.P., et al., in Proc. of the 29th EPS Conf. on Plasma Phys. and Control. Fusion, Montreux, 2002, [ECA **26B** (2002) P-2.081].
[6] REBUT, P.H., et al., Proc. 12th IAEA Conf., Nice 1988, IAEA, Vienna, **12** (1989) 191.
[7] WEISEN, H., et al., Nucl. Fusion **37** (1997) 1741.
[8] PIETRZYK, Z.A., et al., Phys. Plasmas **7**(2000) 2909.
[9] PIETRZYK, Z.A., et al., Phys. Rev. Lett. **86** 1530 (2001) 1530.
[10] PEYSSON, Y., CODA, S., IMBEAUX, F., Nucl. Instrum. and Methods in Phys. Res. A **458** (2001) 269.
[11] CODA, S., et al., in Proc. of the 29th EPS Conf. on Plasma Phys. and Control. Fus., Montreux, 2002, [ECA **26B** (2002) 0-4.03]; CODA, S., et al. Proc. of the 26th EPS Conf. on Control. Fusion and Plasma Phys., Maastricht, 1999, [ECA **23J** (1999) 1097].
[12] BLANCHARD, P., et al, Plasma Phys. Control. Fusion **44** (2002) 2231.
[13] MATSUDA, K., IEEE Trans. Plasma Sci. PS-17 (1989) 6.
[14] HARVEY, R.W., et al., Proc. of the IAEA Tech. Conf. on Advances in Simulation and Models of Thermonuclear Plasmas, Montreal, 1992, (IAEA, Vienna, 1992).

[15] HARVEY, R.W., SAUTER, O., PRATER, R. and NIKKOLA, P., Phys. Rev. Lett. **88** (2002) 205001.
[16] NIKKOLA, P., et al., to be published in Theory of Fusion Plasmas (Proc. Joint Varenna-Lausanne Int. Workshop) (Varenna 2002), edited by J.W. Connor, O. Sauter and E. Sindoni, ISPP-20 (Bologna, Editrice Compositori) (2002); NIKKOLA, P., et al., in Proceedings of the 12th Joint Workshop on ECE and ECRH, Aix-en-Provence, May 13-16, 2002 (World Scientific, Singapore, 2002) 257.
[17] SAUTER, O., et al., in Proc. of the 29th EPS Conf. on Plasma Phys. and Control. Fusion, Montreux, 2002, [ECA **26B** (2002) P-2.087].
[18] SAUTER, O., et al., this conference EX/P5-06.
[19] BOSSHARD, P., et al., Proc. of the 28th EPS Conf. on Control. Fus. and Plasma Phys., Madeira, 2001, edited by C. Silva, C. Varandas and D. Campbell [ECA **25A** (2001) 365].
[20] PORCELLI, F., BOUCHER, D., and ROSENBLUTH, M.N., Plasma Phys. Control. Fusion **38** (1996) 2163.
[21] ANGIONI, C., et al., submitted to Nucl. Fusion; ANGIONI, C., et al., in Proc. of the 29th EPS Conf. on Plasma Phys. and Control. Fusion, Montreux, 2002, [ECA **26B** (2002) P-1.118].
[22] FISCH, N.J., Phys. Fluids **28** (1985) 245.
[23] HENDERSON, M.A., et al., Fusion Eng. Des. **53** (2001) 241.
[24] GOODMAN, T.P., et al., this conference EX/P5-11.
[25] REIMERDES, H., et al., Phys. Rev. Lett. 88 (2002) 105005-1; REIMERDES, H., PhD Thesis, Lausanne Internal Report LRP 700/01 (2001).
[26] SUTTROP, W., Plasma Phys. Control. Fusion **42** (2000) A1
[27] MARTIN, Y., TCV Team, in Fusion Energy 2000 (Proc. 18th Int. Conf. Sorrento, 2000), IAEA, Vienna (2001) CD-ROM file EXP5/30 and http://www.iaea.org/programmes/ripc/physics/fec2000/html/node1.htm
[28] DEGELING, A.W., et al., Plasma Phys. Control. Fusion **43** (2001) 1671.
[29] MARTIN, Y.R., DEGELING, A.W., LISTER, J.B., Plasma Phys. Control. Fusion **44** (2002) A373.
[30] DEGELING, A.W., et al., in Proc. of the 29th EPS Conf. on Plasma Phys. and Control. Fusion, Montreux, 2002, [ECA **26B** (2002) P-2.078]
[31] PORTE, L., et al., this conference EX/P5-15.
[32] HOGGE, J-Ph., et al., in Proceedings of the 12th Joint Workshop on ECE and ECRH, Aix-en-Provence, May 13-16, 2002 (World Scientific, Singapore, 2002) 371.
[33] ALBERTI, S., et al., in Proc. of the 29th EPS Conf. on Plasma Phys. and Control. Fusion, Montreux, 2002, [ECA **26B** (2002) P-2.073].
[34] MANINI, A., et al., Plasma Phys. Control. Fusion **44** (2002) 139; GOODMAN, T.P., et al., Proc. of the 28th EPS Conf. on Control. Fus. and Plasma Phys., Madeira, 2001, edited by C. Silva, C. Varandas and D. Campbell [ECA **25A** (2001) 925]; ALBERTI, S., et al., in Fusion Energy 2000 (Proc. 18th Int. Conf. Sorrento, 2000), IAEA, Vienna (2001) CD-ROM file PD/2 and http://www.iaea.org/programmes/ripc/physics/fec2000/html/node1.htm
[35] HOFMANN, F., et al., Phys. Rev. Lett. **81** (1998) 2918.
[36] HOFMANN F. et al., Plasma Phys. Control. Fusion **43** (2001) A161.
[37] POCHELON, A., et al., Nucl. Fusion **41** (2001) 1663.
[38] CAMENEN, Y., et al., in Proceedings of the 12th Joint Workshop on ECE and ECRH, Aix-en-Provence, May 13-16, 2002 (World Scientific, Singapore, 2002) 407.
[39] RAJU, D., et al., in Proc. of the 29th EPS Conf. on Plasma Phys. and Control. Fusion, Montreux, 2002, [ECA **26B** (2002) P-2.082].
[40] POCHELON, A., et al., this conference, EX/P5-14.

Electron Cyclotron Current Drive and Suprathermal Electron Dynamics in the TCV Tokamak

S. Coda 1), S. Alberti 1), P. Blanchard 1), T.P. Goodman 1), M.A. Henderson 1), P. Nikkola 1), Y. Peysson 2), O. Sauter 1)

1) Centre de Recherches en Physique des Plasmas, Association EURATOM-Confédération Suisse, Ecole Polytechnique Fédérale de Lausanne, CRPP - EPFL, CH-1015 Lausanne, Switzerland
2) Département de Recherches sur la Fusion Contrôlée, Association EURATOM-CEA, CEA/Cadarache, 13108 Saint Paul-lez-Durance Cédex, France

e-mail contact of main author: stefano.coda@epfl.ch

Abstract - Electron cyclotron current drive (ECCD) is an important prospective tool for tailoring the current profile in next-step devices. To fill the remaining gaps between ECCD theory and experiment, especially in the efficiency and localisation of current drive, a better understanding of the physics of suprathermal electrons appears necessary. On TCV, the fast electron population is diagnosed by a multichordal, spectrometric hard X-ray camera and by a high field side ECE radiometer. The main modeling tool is the quasilinear Fokker-Planck code CQL3D, which is equipped with a radial particle transport model. Systematic studies of fast electron dynamics have been performed in TCV with modulated or pulsed electron cyclotron power, followed by coherent averaging, in an attempt to identify the roles of collisional relaxation and radial diffusion in the dynamics of the suprathermal population. A consistent picture is beginning to emerge from experiment and modeling, pointing to the crucial role of the radial diffusion of suprathermal electrons in the physics of ECCD.

1. Introduction

Electron cyclotron current drive (ECCD) is an important tool for current profile shaping in magnetically confined plasmas, thanks to the highly localised power deposition of the EC wave and the ease of external control of its deposition location and wave-number spectrum. The strong influence exerted in turn by the current profile shape on the stability of the plasma to MHD modes, as well as on its confinement properties, motivates much current ECCD research.

The development of high power, high frequency, long pulse gyrotron sources in recent years has provided the fusion community with a versatile and mature technology for next-step thermonuclear fusion devices. The TCV tokamak (R=0.88 cm, a=0.25 cm, I_p<1 MA, B_T<1.54 T) is equipped with a 4.5 MW EC heating system, powered by six second harmonic (X2, 82.7 GHz) and three third harmonic (X3, 118 GHz) 0.5 MW gyrotrons. An extremely flexible EC beam delivery system, allowing real-time poloidal and toroidal steering, matches the equally flexible plasma position and shape control system of TCV [1].

ECCD experiments have been performed in TCV with the X2 system, for a total delivered power of up to 2.8 MW in X-mode, in a wide variety of plasma shapes, with a broad range of parallel wave numbers and heating locations. In particular, steady-state, fully non-inductive discharges sustained entirely by ECCD and bootstrap current are now routine on TCV [2-4].

The high energy electron population created by ECCD is diagnosed primarily with a hard X-ray (HXR) pinhole camera, on loan from Tore Supra, and with a high field side electron cyclotron emission (ECE) system. HXR bremsstrahlung emission is detected by a linear array of CdTe detectors along 14 chords which cover the outboard half of the cross section. The radial resolution is ~2 cm on the midplane, and the energy resolution is ~7 keV [5]. Spectral pulse height

analysis is performed with eight energy bins available for each chord, with adjustable thresholds within the 10-200 keV range.

The second harmonic X-mode ECE radiometer observes the plasma along one of three possible horizontal viewlines, two on the high field side and one on the low field side, and operates in the 78-114 GHz range with 24 channels of 0.75 GHz bandwidth [6]. The EC radiation observed on the high field side is dominated by relativistically downshifted emission by the high energy end of the electron distribution function and can thus be employed to diagnose the suprathermal population.

The quasilinear Fokker-Planck code CQL3D [7] is employed to model the dynamics of the electron distribution function. The code is coupled to the TORAY-GA ray-tracing module [8] and solves the Fokker-Planck equation in two velocity and one spatial dimensions. The equation includes a quasilinear EC wave damping term, a relativistic collision operator and a model for radial diffusion, with an optional linear dependence on the parallel velocity and a particle-conserving advection term.

2. ECCD and suprathermal electrons

The ability to control the deposition location and toroidal injection angle accurately is instrumental in the application of ECCD to current profile tailoring. This high degree of control was clearly demonstrated in TCV by sustaining the non-inductive plasma current with two X2 gyrotrons at the time, and firing two sets of two gyrotrons in succession for their maximum pulse durations (2 s). As shown in Fig. 1, the TCV discharge length was thus extended to a record 4.3 s, well beyond the maximum length achievable in Ohmic conditions. Matching the powers, deposition locations and parallel wave numbers of the two sets of beams is essential for a smooth switch-over. This external control was further demonstrated by an interlaced square-wave modulation of the two clusters (180 degrees out of phase), with no visible resulting modulation of the plasma parameters.

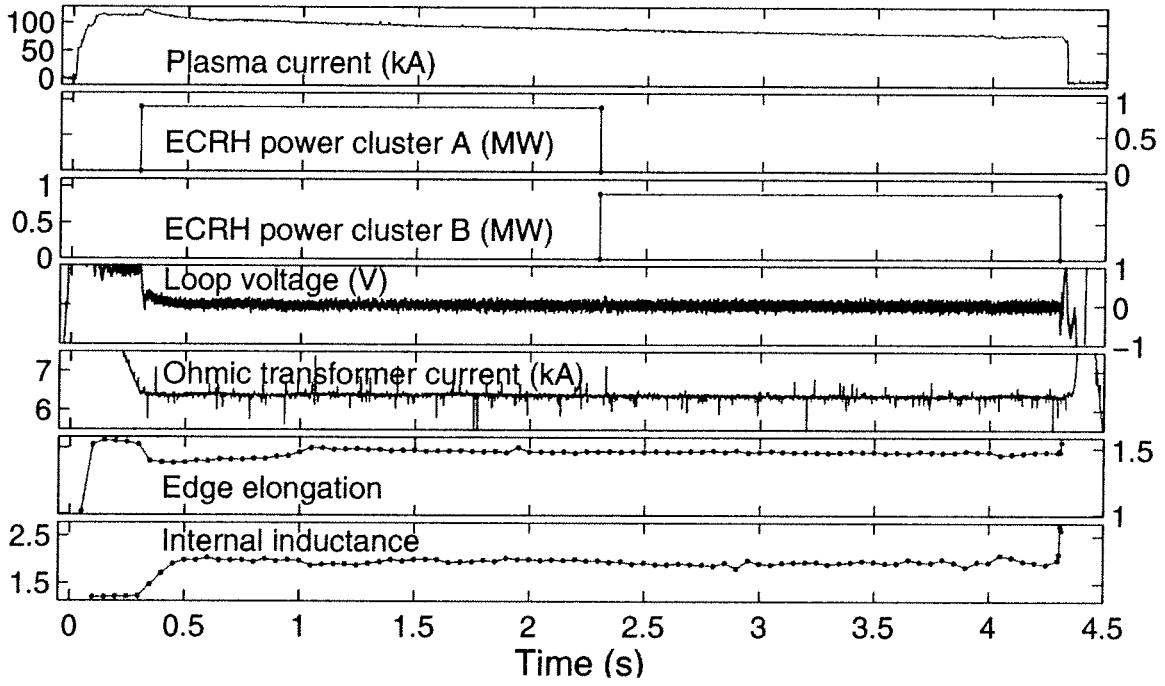

FIG. 1. TCV discharge 20881 of record length (4.3 s), sustained by 0.9 MW ECCD.

Current drive by electron cyclotron waves is theoretically predicted to operate on electrons traveling at substantially suprathermal velocities. Experimental measurements have confirmed that ECCD is accompanied by the creation and sustainment of a significant suprathermal population. Unmistakable suprathermal features are observed when the EC toroidal injection angle ϕ is nonzero, as required for ECCD: the HXR spectral distribution deviates from that of a Maxwellian plasma, and both the HXR photon temperature and the ECE radiative temperature are well in excess of the bulk plasma temperature measured by Thomson scattering [6,9,10]. By contrast, with $\phi \sim 0$ (pure heating mode) the three temperatures coincide.

The presence of a suprathermal electron population created by X2 ECCD has also been shown to engender enhanced absorption of the X3 waves over that expected for a Maxwellian plasma [11].

The energy resolved HXR measurement is a particularly sensitive indicator of the relative dynamics of the thermal and suprathermal components. In a series of recent experiments, an electron internal transport barrier (eITB) has been generated in a fully non-inductively driven plasma by applying off-axis co-ECCD at approximately mid-radius [12]. The barrier forms on a resistive diffusion time scale and is attributed to negative magnetic shear in the core. Once the barrier is formed, ECH power applied in the center increases both the energy and the confinement itself on a confinement time scale. Figure 2 clearly shows the distinct dynamics of the high and low energy components of the bremsstrahlung emission: the former originates from the suprathermal electron population, excited by the initial ECCD but essentially unaffected by the subsequent central ECH, whereas the latter is related to the temperature of the bulk population, which increases dramatically when central heating is applied.

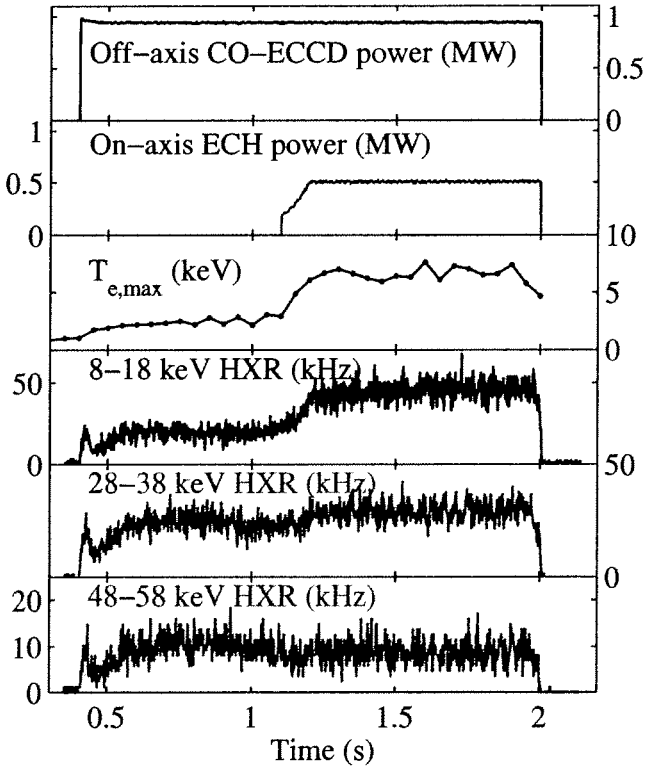

FIG. 2. Creation of an eITB with off-axis co-ECCD (TCV shot 22017). The traces shown are the powers of the two EC components, the peak electron temperature, and three energy channels of the HXR signal on a central chord.

The interpretation of ECE data is complicated by the fact that a given emission frequency corresponds to a continuum of spatial positions and electron energies, since the EC frequency depends, relativistically, on both magnetic field and energy. To deconvolve the two quantities some constraints must be applied. The approach that has shown the most promise is based on the assumption of a bi-Maxwellian electron distribution function, describing the bulk and suprathermal populations. This assumption is qualitatively supported by both HXR data and CQL3D modeling [6]. If profile shapes are assumed for the suprathermal density and temperature, the absolute values of these quantities can then be derived from the ECE data. A sensitivity study has shown that the final results do not depend strongly on the postulated profile shapes; canonical profiles have therefore been chosen, based on suggestions from the HXR data: in particular,

since the shape of the HXR spectrum is almost invariably independent of spatial location, it has appeared reasonable to assume a flat suprathermal temperature profile. If this procedure is correct, the derived suprathermal temperature should coincide with the HXR photon temperature (calculated from an exponential fit to the high energy component of the spectrum). Fair agreement has been found in the cases studied thus far. These results suggest that the suprathermal density can be up to 25% of the total electron density [6].

3. Suprathermal electron dynamics: the role of spatial diffusion in ECCD

The physical underpinnings of ECRH, particularly the absorbed power and the power deposition profile, have been validated by numerous experimental measurements [13]. Predictions for current drive have also been tested experimentally, with less uniform results: while good agreement with Fokker-Planck quasilinear theory is obtained in some devices [14], discrepancies remain in other cases. In particular, ECCD efficiency in TCV has been generally grossly overestimated by quasilinear theory, which predicted strong nonlinear enhancement by the unusually large EC power densities achieved. Linear theory, on the other hand, underestimates the driven current by factors ranging from 1 to 3.

The key to resolving these discrepancies appears to lie in the dynamics of the suprathermal electron population, as has been evidenced by CQL3D modeling of ECCD experiments. By including a diffusion coefficient D of the order of the bulk thermal diffusivity, the distribution of current-carrying fast electrons is broadened and nonlinear enhancement is strongly inhibited; with D~3 m^2/s, the experimentally measured EC-driven current can generally be reproduced. The same level of diffusivity does not change the predicted efficiency significantly in experimental situations in which nonlinear enhancement is not expected [15]. Thus a unifying picture is beginning to emerge.

The achievement of fully non-inductive discharges driven entirely by off-axis ECCD and bootstrap current, mentioned in the previous section, is a striking illustration of the effect of this suprathermal diffusivity. The value of D having been set such as to match the total driven current, the EC-driven current profile calculated by CQL3D is centrally peaked in spite of the power being deposited approximately at half-radius [16]. (It should be noted that the total current profile is nevertheless calculated to be hollow, owing to a large off-axis bootstrap current contribution.)

A direct experimental measurement of the spatial diffusivity presents formidable difficulties, as was already documented in the long history of lower hybrid current drive experiments [17]. The dynamics of suprathermal electrons are governed by several competing diffusive processes: collisional relaxation in velocity space (slowing-down and pitch-angle scattering), quasilinear rf diffusion in velocity space, and anomalous turbulence-driven diffusion in real space. There is no 'source' in the system, since the heating process itself is of a diffusive nature (albeit not energy conserving). Hence, several potentially overlapping time scales are at play, and an unambiguous determination of the complete system dynamics is difficult to conceive under controlled experimental conditions. On TCV, we have adopted the approach of applying multiple techniques aimed at providing progressively stronger constraints on these dynamics.

Two such techniques have been employed recently to exploit the specific characteristics of the HXR and ECE diagnostics, respectively. Square-wave modulation of the electron cyclotron power has been performed in order to enhance the photon statistics and thus the temporal resolution of the HXR camera by coherent averaging. Photon statistics also dictated high power lev-

els (typically 2.35 MW with 50% duty cycle), which resulted in strong modulation of the bulk plasma parameters, particularly density and temperature. Since the electron energy confinement time is of the same order as the slowing-down time for electrons travelling at 5 to 8 times the thermal velocity, a separation of the relevant time scales becomes impossible. However, information on the suprathermal dynamics is contained in the temporal evolution of the spectral distribution of the HXR signals. As mentioned in the previous section, the spectral shape in the relaxed state is nearly invariably uniform in space, even well outside the theoretical power deposition region. However, these measurements have shown for the first time that this is not the case immediately after switch-on: as shown in Fig. 3(a) for a case with central co-ECCD (ϕ=29°), the signal from a central chord is initially larger than the off-axis signal at low energy, while their roles are reversed at high energy. The on-axis spectrum does not change appreciably over time, whereas the off-axis spectrum becomes similar to the former over a period of approximately 10 ms. A corresponding relaxation of the photon temperature profile towards a flat profile is seen in Fig. 3(b) [10].

The uniformity of the photon temperature suggests spatial equilibration. Electrons of different velocities are heated in different radial positions, owing to the Doppler shift required to match the local resonance condition in a spatially varying magnetic field. Additionally, the physical parameters that govern the steady-state distribution function, i.e. the EC power density, the bulk plasma density and the bulk electron temperature, are all spatially varying functions. Therefore the resulting spectral distribution should not be spatially uniform in general, unless communication is occurring over distant regions in space, i.e. by transport of suprathermal electrons. This evidence is considerably strengthened by the temporal evolution, which shows that the initial spectrum is indeed consistent with larger resonant velocities off-axis. From the observed relaxation time we can deduce a lower bound ~1.5 m^2/s for the diffusivity in this discharge.

The higher sensitivity of the ECE system is compatible with perturbative studies. In a second experiment, we have applied short periodic ECCD pulses to the plasma and studied the ECE response by coherent averaging. Pulses longer than 0.3 ms were seen to result in a first peak,

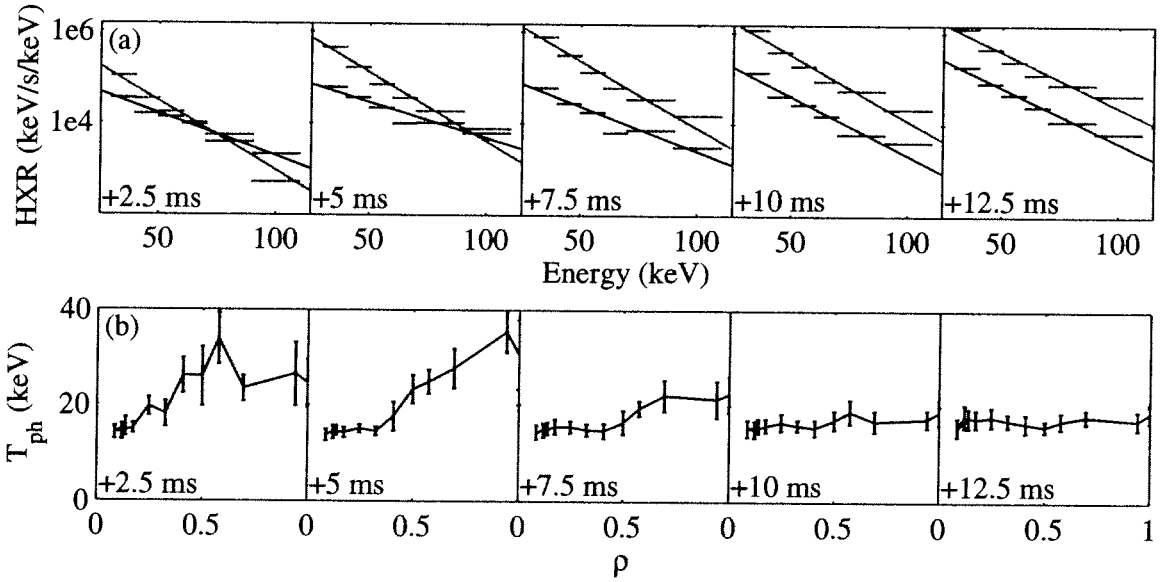

FIG. 3. TCV shot 21978: (a) HXR emissivity as a function of energy in 5 snapshots after the ECCD switch-on (t=0), for a central (red) and an off-axis (blue, ρ~0.6) chord; (b) spatial profiles of the photon temperature for the same snapshots (ρ here indicates the minimum normalized radius for each chord, i.e. the point of tangency to the flux surface) [10].

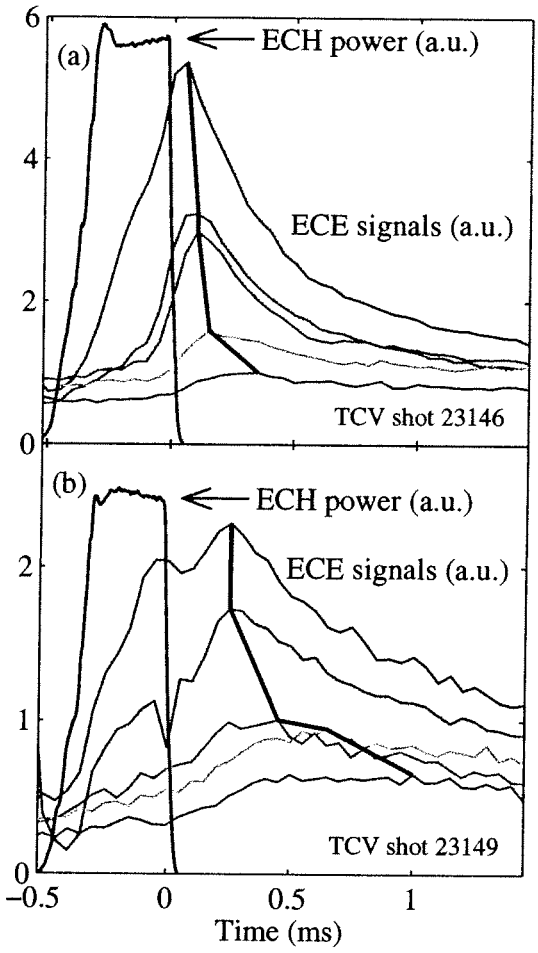

FIG. 4. Response of selected ECE signals to a short central ECCD pulse, averaged over 170 coherent pulses; the ECE frequency increases as the peak moves to later times; (a) ECE radiometer on the midplane, (b) ECE radiometer off-axis (ρ > 0.55). (See geometry in Fig. 5.)

followed by a descent and a further increase until the end of the pulse, indicating that the pulse length exceeded the characteristic rf diffusion time. To avoid this complicating effect, the pulse was thus kept to a length of 0.25-0.3 ms. The applied power was 0.45-0.9 MW with a period of 10 ms, therefore a 3% duty cycle and an average power < 27 kW, too low to affect the plasma parameters measurably. Two examples, both with central ECCD, are shown in Fig. 4, with the plasma and ECE radiometer geometries shown in Fig. 5. In the case of Fig. 4(a) the ECE chord goes through the plasma center, whereas in the case of Fig. 4(b) the smallest normalized minor radius accessed by ECE is approximately 0.55. In both cases the time to peak increases with the ECE frequency, as shown in Fig. 6. Moreover, the time lags are clearly larger when the ECE radiometer is aimed off-axis: indeed, when plotted versus the cold-resonance minor radius, the two curves connect smoothly to each other [Fig. 6(II)]. It should be remembered that an increase in frequency can be associated either to a shift towards the high field side (larger minor radius) or to an increase in electron energy; however, for equal energy and frequency, the signals from the two chords originate in different spatial regions. Thus this observation corroborates the hypothesis that a diffusive mechanism is at play and that a non-negligible fraction of the fast electrons generated by ECCD is transported far from the deposition region. A more quantitative analysis will require modeling. In particular, the time lag will generally depend on both the slowing-down time and the diffusion time: therefore the detailed dependence of the time lag on the frequency cannot uniquely provide quantitative information on the diffusion coefficient. The time to peak is, however, only one parameter of the dynamical response. The full dynamics, particularly the decay time, can provide strong constraints on the modeling. Further work is planned in this direction.

A further approach to studying the suprathermal electron relaxation phenomena consists of direct comparisons of HXR data with bremsstrahlung emission predicted by the CQL3D code for the specific geometry of our diagnostic. Without spatial diffusion, not only is the predicted current much too large, the predicted HXR signal is also far narrower spatially than the measured one. After the diffusion coefficient is adjusted to permit the code to match the total driven current, the results for the HXR emission are in much better agreement [10,15,18], generally within a factor of 3 everywhere, as exemplified by Fig. 7(a). In particular, these results provide strong evidence that the spatial uniformity of the spectral shape is a consequence of spatial transport. The shape is parametrized in Fig. 7(b) by a photon temperature, which is seen to be a strong function of minor radius in the case D=0, whereas with D=3 m^2/s a uniform temperature is recovered, which is moreover in very good quantitative agreement with the experimental values.

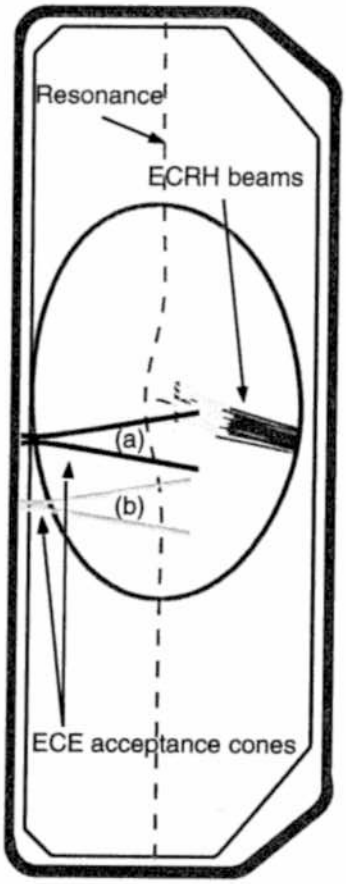

FIG. 5. Geometries of ECRH launching and ECE radiometry for the two cases shown in Fig. 5 (in reality the radiometer is fixed and the plasma and EC beams are moved).

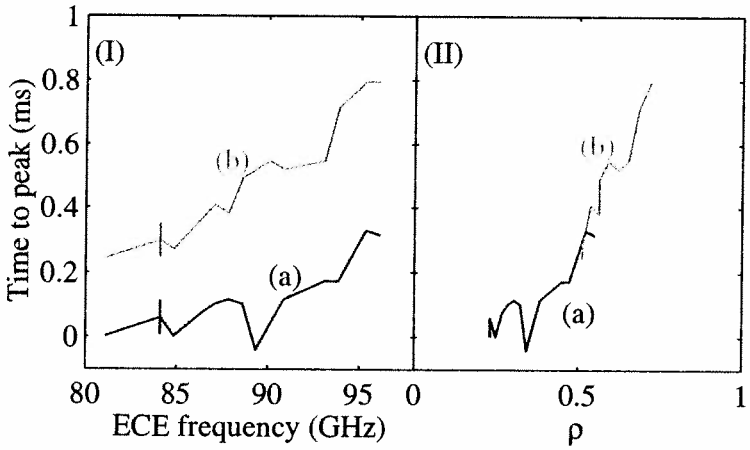

FIG. 6. Time lag from the end of the ECCD pulse to the ECE peak, for the two cases shown in Fig. 4, (I) as a function of ECE frequency, (II) as a function of the cold-resonance normalized radius.

It should be noted that the spectra are only approximately exponential; in particular, at higher energy the calculated slope in the diffusionless case becomes less steep (higher temperature) at larger radius.

4. Conclusions and outlook

ECCD is being used on TCV as a powerful tool for current and pressure profile shaping, especially with the high degree of control afforded by fully non-inductive operation, thus in the absence of an electric field, in steady state. At the same time, TCV is one of the premier test beds for fundamental inquiries into the physics of ECCD and the associated suprathermal electron dynamics, owing to a uniquely powerful and flexible ECH system and dedicated diagnostics, complemented by an advanced and flexible Fokker-Planck quasilinear code. The fundamental relaxation processes governing the suprathermal dynamics are being investigated through multiple experimental approaches and comparisons with modeling.

While strong evidence supports the conclusion that the suprathermal electrons excited by ECCD undergo cross-field diffusion at a rate comparable to that of thermal transport, much remains to be known about the dominant transport mechanism. Fokker-Planck simulations using different transport models, based on both electrostatic and electromagnetic turbulence, have thus far been inconclusive. A crucial question that must be addressed is the dependence of this transport on the ECH power density itself; it is plausible for instance to suppose a power degradation mechanism to be at play as in thermal transport, but this hypothesis has not yet been tested.

Acknowledgments

We are grateful to CEA-Cadarache for the loan of the hard X-ray camera and associated equipment, and to the entire TCV team for the operation of the tokamak and of the auxiliary heating systems. This work was supported in part by the Swiss National Science Foundation.

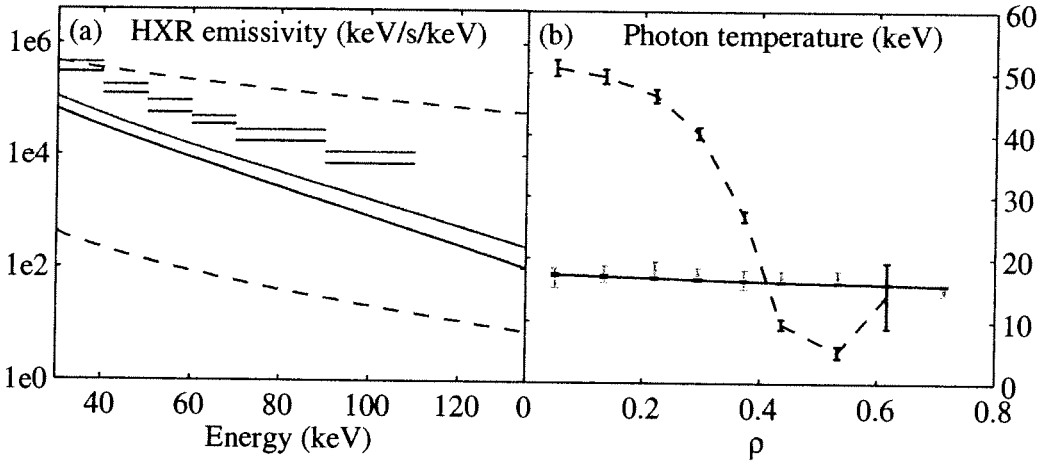

FIG. 7. TCV shot 21982: (a) HXR emissivity spectrum for a central chord (red) and a chord with a minimum ρ~0.37 (blue): experimental data (horizontal bars), CQL3D calculations with diffusivity D=3 m^2/s (solid lines) and D=0 (dashed lines); (b) photon temperature calculated from an exponential fit to the spectra in the interval 30-120 keV, as a function of radial position ρ (minimum normalized radius for each chord): experimental data (green), CQL3D data with D=3 m^2/s (solid black line) and D=0 (dashed black line).

References

[1] GOODMAN, T.P., et al., this conference (paper OV/4.2).
[2] SAUTER O., et al., Phys. Rev. Lett. **84** (2000) 3322.
[3] CODA S., et al., Plasma Phys. Control. Fusion **42** (2000) B311.
[4] SAUTER O., et al., Phys. Plasmas **8** (2001) 2199.
[5] PEYSSON Y., CODA S., IMBEAUX F., Nucl. Instrum. and Methods in Phys. Res. A **458** (2001) 269.
[6] BLANCHARD P., et al., Plasma Phys. Control. Fusion **44** (2002) 2231.
[7] HARVEY R.W., MCCOY M.G., in Proc. IAEA TCM/Advances in Simulation and Modeling in Thermonuclear Plasmas, Montreal (1992).
[8] MATSUDA K., IEEE Trans. Plasma Sci. **PS-17** (1989) 6.
[9] CODA S., et al., Proc. 26th EPS Conf. on Controlled Fusion and Plasma Physics (Maastricht 1999), Europhys. Conf. Abstr. **23J** (1999) 1097.
[10] CODA S., et al., Proc. 29th EPS Conf. on Controlled Fusion and Plasma Physics (Montreux 2002), Europhys. Conf. Abstr. **26B** (2002) (O-4.03).
[11] ALBERTI S., et al., Nucl. Fusion **42** (2002) 42.
[12] SAUTER O., et al., Proc. 29th EPS Conf. on Controlled Fusion and Plasma Physics (Montreux 2002), Europhys. Conf. Abstr. **26B** (2002) (P-2.087); GOODMAN T.P., et al., ibid. **26B** (2002) (p-2.081); SAUTER O., et al., this conference (paper EX/P5-06).
[13] See e.g. GOODMAN T.P., et al., Proc. 2nd Europhysics Topical Conf. on Radio Frequency Heating and Current Drive of Fusion Devices, Brussels, Belgium (1998), p. 245; PETTY C.C., et al., Strong microwaves in plasmas, vol. 1 (2000), p. 41.
[14] See e.g. PETTY C.C., et al., Nuclear Fusion **41** (2001) 551.
[15] HARVEY R.W., et al., Phys. Rev. Lett. **88** (2002) 205001.
[16] NIKKOLA P., et al., Proc. IAEA Tech. Committee Meeting on ECRH Physics and Technology for Fusion Devices and EC-12, Aix-en-Provence, France, 2002 (to be published).
[17] PEYSSON Y., Plasma Phys. Control. Fusion **35** (1993) B253.
[18] NIKKOLA P., et al., Proc. Joint Varenna-Lausanne Int. Workshop, Varenna, Italy, 2002, to be published in Theory of Fusion Plasmas (Editrice Compositori, Bologna, 2002).

Full Radius Linear and Nonlinear Gyrokinetic Simulations for Tokamaks and Stellarators: Zonal Flows, Applied $E \times B$ Flows, Trapped Electrons and Finite Beta

L. Villard 1), S.J. Allfrey 1), A. Bottino 1), M. Brunetti 1), G.L. Falchetto 4), V. Grandgirard 4), R. Hatzky 2), J. Nührenberg 3), A.G. Peeters 2), O. Sauter 1), S. Sorge 3), J. Vaclavik 1)

1) CRPP - EPFL, Euratom-Suisse, Lausanne, Switzerland
2) Max-Planck, Euratom-IPP, Garching, Germany
3) Max-Planck, Euratom-IPP, Greifswald, Germany
4) DRFC, Euratom-CEA, Cadarache, France

e-mail contact of main author: laurent.villard@epfl.ch

Abstract. The aim of this paper is to report on recent advances made on global gyrokinetic simulations of Ion Temperature Gradient modes (ITG) and other microinstabilities. The nonlinear development and saturation of ITG modes and the role of $E \times B$ zonal flows are studied with a global nonlinear δf formulation that retains parallel nonlinearity and thus allows for a check of the energy conservation property as a means to verify the quality of the numerical simulation. Due to an optimised loading technique the conservation property is satisfied with an unprecedented quality well into the nonlinear stage. The zonal component of the perturbation establishes a quasi-steady state with regions of ITG suppression, strongly reduced radial energy flux and steepened effective temperature profile alternating with regions of higher ITG mode amplitudes, larger radial energy flux and flattened effective temperature profile. A semi-Lagrangian approach free of statistical noise is proposed as an alternative to the nonlinear δf formulation. An Asdex-Upgrade experiment with an Internal Transport Barrier (ITB) is analysed with a global gyrokinetic code that includes trapped electron dynamics. The weakly destabilizing effect of trapped electron dynamics on ITG modes in an axisymmetric bumpy configuration modelling W7-X is shown in global linear simulations that retain the full electron dynamics. Finite β effects on microinstabilities are investigated with a linear global spectral electromagnetic gyrokinetic formulation. The radial global structure of electromagnetic modes shows a resonant behaviour with rational q values.

1. Introduction

ITG modes and other microinstabilities are the physics basis of several gyrofluid or gyrokinetic models that attempt to describe anomalous transport in magnetically confined plasmas [1] . The prominent role of zonal flows in the ITG saturation was recognized already some time ago in gyrofluid [2] and gyrokinetic [3] simulations. Through nonlinear coupling of ITG modes a component of the electric field normal to the magnetic surfaces is driven. The $E \times B$ drift of this component, in other words the zonal $E \times B$ flow, in turn reduces the level of ITG turbulence. Thus the zonal component of the perturbation appears as a regulator of the ITG turbulence. It should be ensured that the numerical discretisation scheme does not introduce spurious damping mechanisms in particular of the zonal component, which is linearly totally undamped by collisionless processes [4], since this would affect its amplitude and consequently the ITG turbulence level. At this point the check of energy and particle conservation properties [5] becomes an extremely useful and stringent test of the quality of the numerical simulation.

Methods based on the PIC δf method [6] have been widely used to solve the gyrokinetic equations. Satisfying energy conservation has proven to be technically rather difficult.

The main obstacle is to reduce the numerical noise inherent to such methods down to an acceptable level, in other words the challenge is to have a good enough statistics for the gyrocenter tracers. While the parallel nonlinearity was neglected in some works, thus relinquishing underlying energy conservation properties, it was only recently that energy conservation was demonstrated in nonlinear full-radius gyrokinetic simulations, the result of an optimised loading technique that uses the energy conservation as an indicator of the numerical quality [7, 8]. Results of the application of this method are presented in Section 2 and compared with results without optimisation. The consequences of neglecting the parallel nonlinearity are also shown. A "semi-Lagrangian" formulation is introduced as an alternative to the PIC δf approach.

More physical effects appear when not only the ion, but also the electron dynamics are taken into account. In Section 3 we show the application of a model that assumes adiabatic passing electrons and drift-kinetic trapped electrons to the study of $E \times B$ stabilisation in an Asdex-Upgrade shot with an ITB. Then a model that includes the full electron dynamics is applied to a bumpy cylindrical configuration relevant for W7-X parameters. When finite plasma β is taken into account the microinstabilities become electromagnetic in character. As the toroidal-ITG mode is stabilised with increasing β another mode, called kinetic ballooning mode [9] or Alfvénic-ITG [10], is destabilised with a threshold value below the ideal MHD ballooning limit. We show the results of a global spectral gyrokinetic approach that has allowed us to find a remarkable resonant behaviour of the AITG mode radial structure with rational q values. Finally, the main findings and possible future works are discussed in Section 4.

2. Energy conserving simulations of ITG modes and zonal $E \times B$ flows

In this Section we consider a straight cylindrical configuration. Parameters are pertinent to W7-X: $B_0 = 2.5T$, $a = 0.55m$, $T_i = 5keV$, deuterium, (thus $a = 135\rho_{Li}$), uniform density and T_e profiles, ion temperature gradient with $a/L_T = 3$ peaking at mid-radius. We solve the gyrokinetic equations for ions and a quasi-neutrality equation assuming an adiabatic electron response within cylindrical surfaces. In addition to the $E \times B$ nonlinearity the $v_{||}$ nonlinearity is retained and thus an energy conservation principle is satisfied:

$$\mathcal{E}_{kin} = \int \frac{1}{2} m_i v^2 f d\mathbf{R} d\mathbf{v}, \quad \mathcal{E}_{field} = \int \frac{q_i}{2} \left(\langle n_i \rangle - n_0 \right) \phi \, d\mathbf{x}, \quad \frac{d}{dt} \left(\mathcal{E}_{kin} + \mathcal{E}_{field} \right) = 0, \qquad (1)$$

where $\langle\rangle$ indicate a gyro-averaged quantity. A finite element, PIC, δf method is used. Pseudo-randomly chosen points in phase space, or "tracers", are evolved according to the gyrocenter trajectories. The quasi-neutrality equation is solved using a finite element method. The perturbed gyro-averaged ion density is obtained by projection onto the finite element basis. Statistical noise is inherent to the method. The use of a δf approach [6], in which only the perturbed part of the distribution function is used in solving the quasineutrality equation, greatly reduces numerical noise. However, the method can be further improved. The optimised loading technique [7] consists in choosing a distribution of the gyrocenters that minimises this statistical noise. First, a numerical simulation is run with a tracer density proportional to an equilibrium Maxwellian up to a point

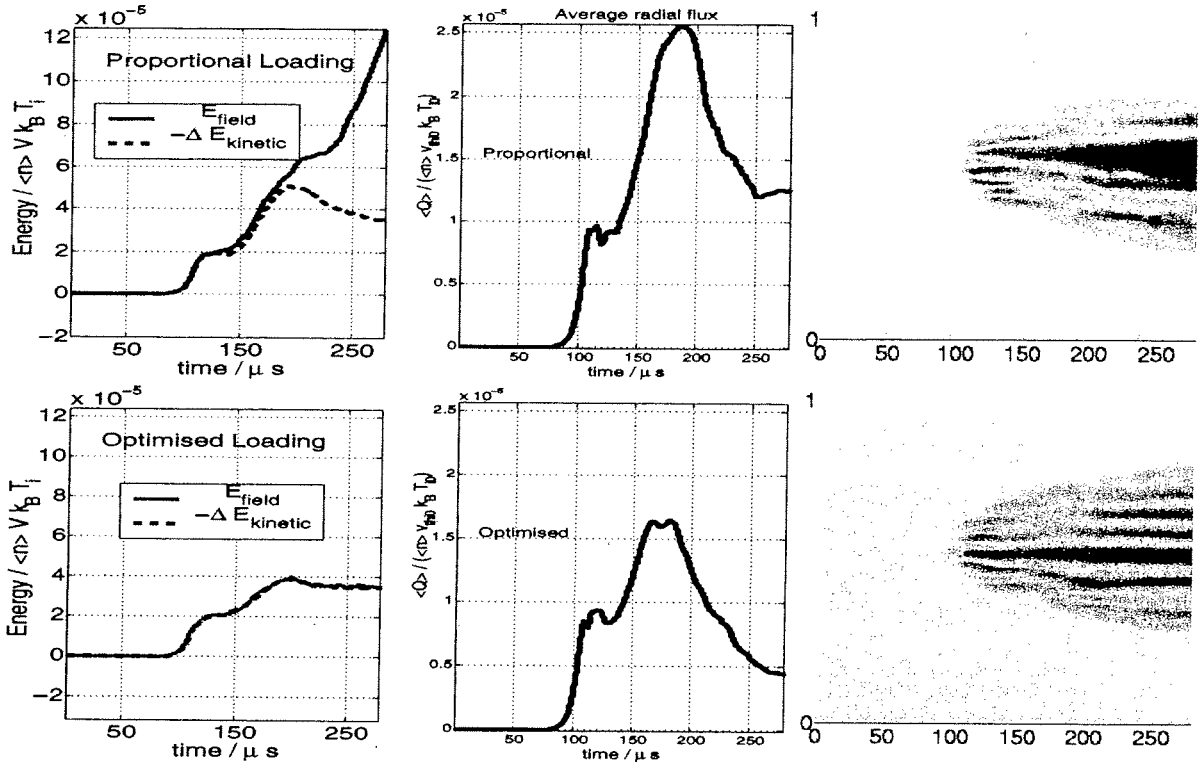

Figure 1: *Field and kinetic energy (left), average radial heat flux (middle) and zonal $E \times B$ component $E_r(r)$ versus time, for an unoptimised (proportional) loading (top) and after loading optimisation (bottom).*

before the quality of the simulation becomes poor, with the energy conservation serving as an indicator of the quality. The values of $|\delta f|$ are back-mapped to the original tracer positions and a new distribution of tracers is generated from this data. The bottom line is to increase the density of tracers in active regions of phase space. Then a new simulation is performed starting with the new tracer distribution. Eventually, the whole process can be repeated until the desired accuracy is obtained.

We show in Fig.1 the effect of the loading optimisation on the energy conservation, average radial heat flux, and zonal flows. It is obvious that the optimisation leads to an excellent energy conservation. A striking feature is that important physical quantities obtained with proportional loading start to deviate from the physically more correct results as soon as the energy is not conserved ($t > 150\mu s$): the heat flux is a factor of more than 2 too high at the end of the simulation and the regular zonal flow structure is destroyed. Snapshots around $t = 300\mu s$ of the ITG and zonal component of the electric field (Fig.2) show a remarkable structure with regions of positive E_r coinciding with suppressed ITG mode activity and regions of negative E_r in which ITG modes have a larger amplitude. The effective ion temperature profile is steepened in the supressed ITG regions and flattened in the active ITG regions.

We have confirmed the pivotal role of zonal flows in artificially supressing the zonal component: we have found a radial heat flux an order of magnitude higher. We have also investigated the consequences of neglecting the $v_{||}$ nonlinearity in the equations. The

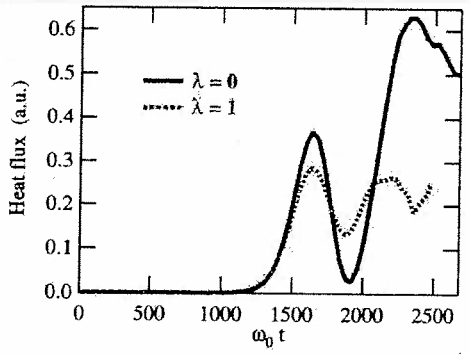

Figure 4: *Heat flux without (full line) and with (dashed line) zonal flows, obtained in a semi-Lagrangian nonlinear drift-kinetic simulation.*

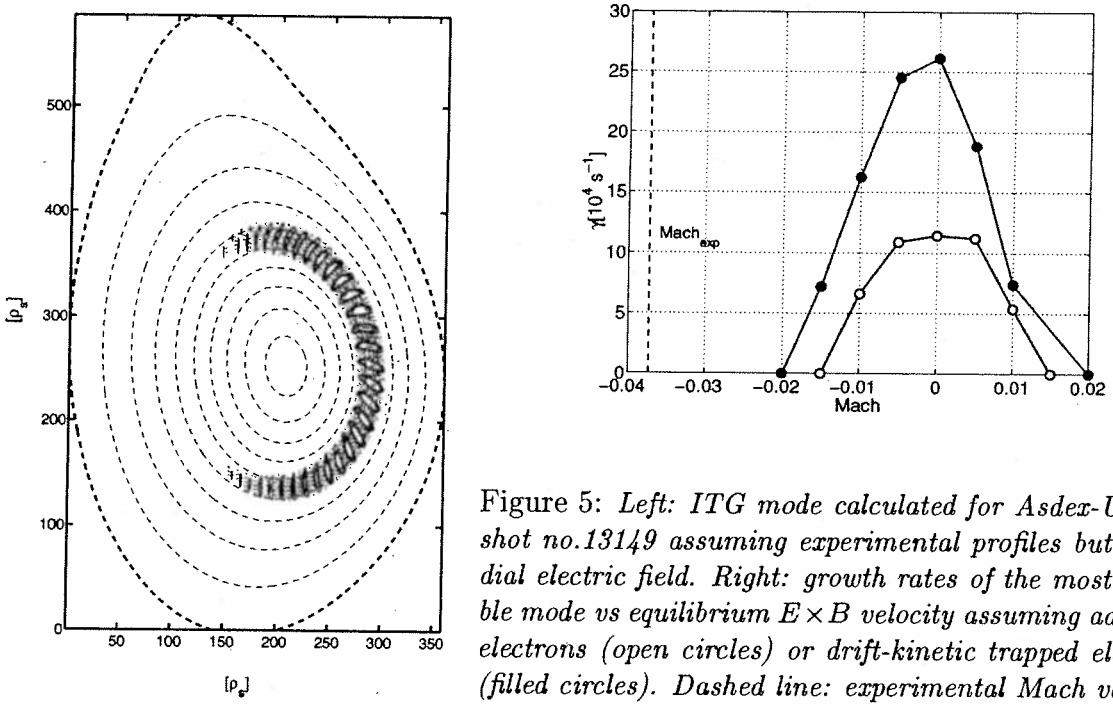

Figure 5: *Left: ITG mode calculated for Asdex-Upgrade shot no.13149 assuming experimental profiles but no radial electric field. Right: growth rates of the most unstable mode vs equilibrium $E \times B$ velocity assuming adiabatic electrons (open circles) or drift-kinetic trapped electrons (filled circles). Dashed line: experimental Mach value.*

3. Effects of non-adiabatic electron dynamics and magnetic curvature

The non uniformity of the magnetic field along the field line creates trapped particle populations and can affect microinstabilities in various ways. For example, trapped electrons tend to respond non-adiabatically and their presence is overall destabilising. In previous works it was shown that equilibrium radial electric fields and their associated $E \times B$ flows in tokamak and heliac configurations stabilize toroidal, helical and slab ITG modes with a quadratic dependence on the shearing rate, whereas trapped particle modes can be *destabilized* by $E \times B$ flows [8, 12].

We consider Asdex-Upgrade shot no.13149 in which an ITB was formed. We study the global linear stability properties with a model that includes the non-adiabatic trapped electron response and the equilibrium radial electric fields. Considering the actual (reconstructed) experimental equilibrium configuration and profiles of temperatures and density, but ignoring the radial electric field, we show in Fig.5 (left) the most unstable mode found: it is a toroidal-ITG further destabilised by trapped electrons. We then con-

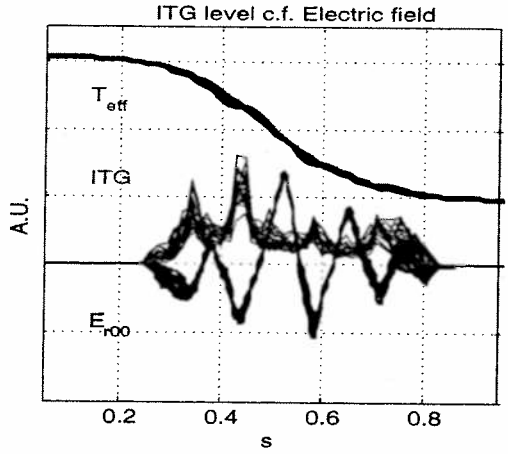

Figure 2: *Snapshots of zonal $E \times B$ flow, ITG amplitude, and effective temperature profiles well into the nonlinear stage of the optimised simulation of Fig.1 around $t = 300\mu s$.*

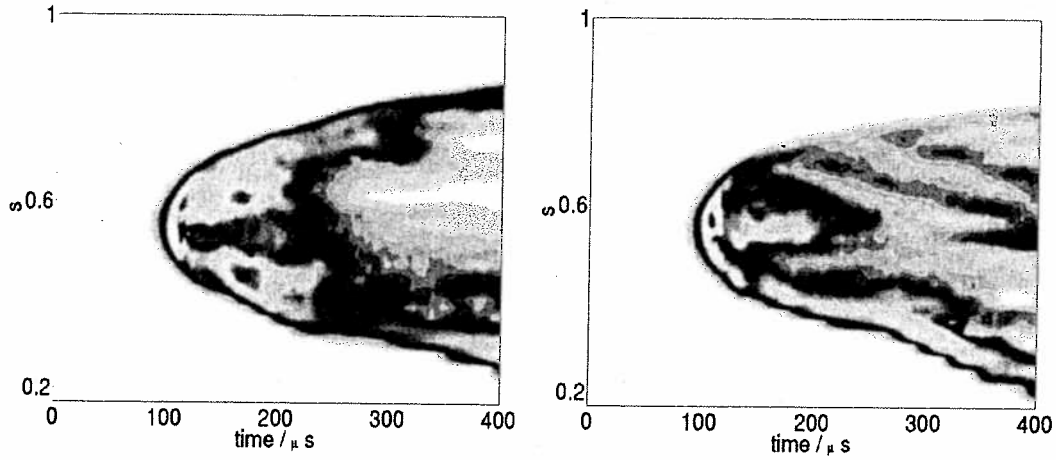

Figure 3: *Radial heat flux vs time with (left) and without (right) $v_{||}$ nonlinearity.*

main consequences are the absence of nonlinear ion Landau damping but also that the energy conservation property is missing and therefore a precious indicator of the quality of the numerics is lost. We have found that it has consequences on the nonlinear evolution: a Fourier decomposition of the field energy shows in particular that all components with $m = 0, n \neq 0$ are entirely unpopulated. The zonal $E_r(r)$ pattern is strongly affected and with it the radial heat flux (Fig.3). (Note that a similar important role of the parallel velocity nonlinearity, but on electrons, was found in the case of drift wave turbulence [11]).

An alternative to the PIC-δf method is the semi-Lagrangian approach. This method retains both an Eulerian aspect in that the phase space is discretised on a fixed grid and a Lagrangian aspect in that the gyrocenter trajectories are computed (characteristics) to obtain the evolution of the full distribution function f. Preliminary results of a new code written for the cylindrical geometry and assuming drift-kinetic ions and adiabatic electrons show that the linear properties are well reproduced, that the zonal flows indeed have a prominent role in the saturation mechanism (see Fig.4), and that the energy conservation property can be satisfied with reasonable accuracy. The qualitative behaviour of the nonlinear stage is similar to that of PIC codes, but there remains a discrepancy to be resolved in the level of saturated mode amplitudes.

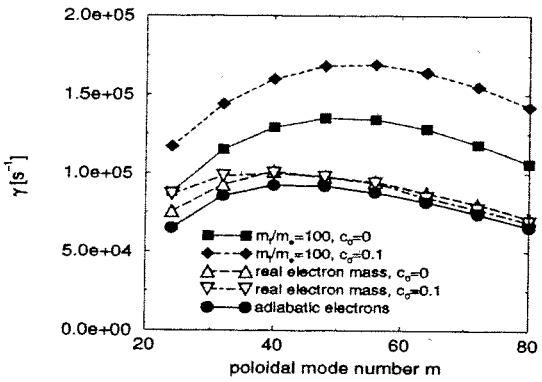

Figure 6: *Growth rates of $n = 2$ modes vs m calculated for different bumpiness parameters c_0 and ion to electron mass ratios, in a global simulation with both gyrokinetic ions and electrons, for W7-X-like parameters.*

sider the equilibrium radial electric field and study the linear growth rate as a function of the Mach number of the $E \times B$ velocity, by scaling the experimental profile by a series of constant factors. Fig.5 (right) shows that for the value inferred from experimental measurements (dashed line) the modes are completely stabilised. We have performed the computations using the assumption of a fully adiabatic electron response and repeated the calculations with adiabatic passing electrons but non-adiabatic (drift-kinetic) trapped electrons. In that experiment the inferred ion heat diffusivity was improved not only at the ITB location but in the whole volume interior to it, a region of negative shear. In order to understand this, we have performed numerical simulations with all parameters as for experiment, save for considering a temperature gradient localised around some region. Our results show that the ITG modes (including trapped electrons) are stable throughout the reversed shear region, but unstable outside.

We now consider an axisymmetric bumpy equilibrium configuration in which the dominant non uniformity of B is a mirror term.

$$\vec{B}(r,z) = B_0[\vec{e}_r N c_0/(2R_0) r sin(Nz/R_0) + \vec{e}_z(1 + c_0 cos(Nz/R_0)], \qquad (2)$$

where N is the periodicity of the system (in this case N=5). For $c_0 = 0.1$, one gets 28% trapped particles for a major radius $R_0 = 5.5m$, a minor radius $a = 0.55m$ and a field strength $B_0 = 2.5T$. These are typical parameters for the W7-X stellarator. Both ions and electrons are modelled as fully gyrokinetic. Fast electron motion introduces constraints on the time step and can increase numerical noise. The difficulty is overcome by using the optimised loading scheme which allows us to reach numerically converged results with a substantially reduced number of gyrocentre tracers. The influence of the trapped particles and non-adiabaticity is shown in Fig.6. Considering an artificial $m_i/m_e = 100$ mass ratio we observe that including the magnetic field bumpiness is overall destabilising. However, as the mass ratio is increased this destabilising effect decreases and for the physical mass ratio becomes practically negligible and very close to the adiabatic electron model prediction.

We have extended the global spectral approach of Ref.[13] to electromagnetic perturbations with a two-potential formulation $(\phi, A_\parallel)$, (thus neglecting the perturbed parallel magnetic field). All orders in ion Larmor radius are retained and non adiabatic drift-kinetic electrons are included in the model. The formulation is applied to a large aspect ratio toroidal configuration. Our results (Fig.7, left) show that as β is increased, the

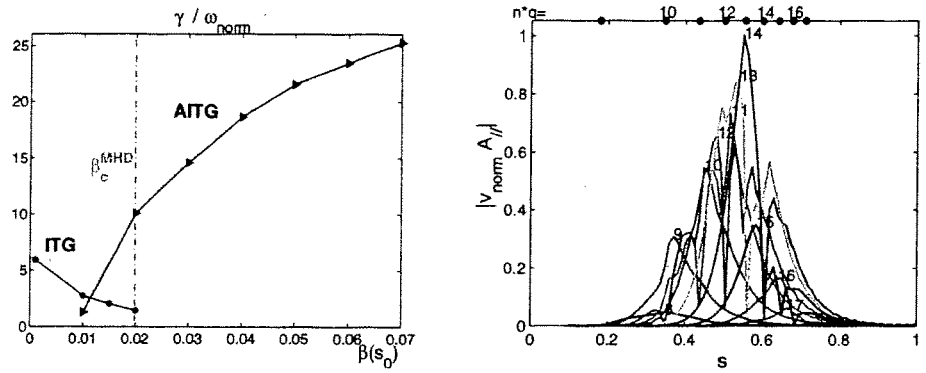

Figure 7: *Left: growth rate of ITG and Alfvénic-ITG (AITG) modes vs beta, critical β for ideal MHD ballooning (vertical line). Right: radial structure of AITG eigenmode showing resonant behaviour at rational q values indicated by the circles on top axis.*

toroidal-ITG growth rate decreases. At a β value about half the critical β limit for ideal MHD ballooning modes, another mode (AITG) is destabilised, qualitatively confirming earlier results [9, 10, 14]. The remarkable feature obtained with our global approach is the eigenmode structure. Fig.7 (right) shows the radial structure of the modulus of poloidal Fourier components of $A_{||}$. At rational q surfaces (circles on top axis) the corresponding m amplitude goes to zero with a sharp localised radial gradient. This behaviour is due to the non-adiabatic electron response: the ratio $|\omega|/k_{||}v_{the}$ varies from much smaller than unity far from the rational surfaces to larger than unity in their vicinity. We note that such a mode structure cannot be found with electron fluid models. It is of course unaccessible to local models that assume e.g. $k_{||} \approx 1/qR$ or to models based on first order ballooning approximation. The sharp radial structure implies that $k_\perp \rho_{Li} \sim 1$, and thus models that use low order expansions in $k_\perp \rho_{Li}$ may be inaccurate. Our approach overcomes all these difficulties.

4. Discussion and future directions of work

We have demonstrated the pertinence of using the energy conservation principle as an indicator of the quality of nonlinear global gyrokinetic simulations. The optimised loading technique is very effective in improving this quality. We have observed a clear correlation between the achieved accuracy of the energy conservation and that of other important physical quantities such as the heat flux or the zonal component of the perturbation. The importance of retaining the $v_{||}$ nonlinearity has also been evidenced. The pivotal role of the zonal component of the perturbation has been confirmed. We have shown how the system establishes a particular radial structure with regions of reduced heat flux alternating with regions of higher heat flux. The zonal component of the electric field, once this structure is established, stays quasi-steady on much longer time scales as compared to the inverse linear growth rates of ITG modes. The question arises as to how to use the global gyrokinetic results for transport modelling. A local diffusion coefficient can obviously not reproduce the observed structured features of heat flux. The optimised loading scheme has very recently been implemented in the toroidal version of the code and first results indicate that it does also improve the quality of the simulations.

We have shown the consistency of the presence of an ITB in an Asdex-Upgrade experiment with the $E \times B$ stabilisation. Detailed analysis of other shots but without ITB will be performed in the future. We have shown that trapped electron dynamics is only weakly destabilising ITG modes in a bumpy configuration modelling W7-X. Global gyrokinetic computations using the full 3D geometry of the equilibrium magnetic field show that ITG modes are rather weakly coupled by 3D geometrical effects in W7-X and growth rates are close to those obtained in a straight cylinder. This gives some justification for the relevance of the simplest geometry (cylinder) and the simplest electron model (adiabatic) used in our nonlinear simulations. Of course more work is needed to ascertain this hypothesis. We have shown that the inclusion of electron dynamics and electromagnetic effects creates a resonant radial structure of the unstable modes at rational q values. Further works, in particular nonlinear global electromagnetic gyrokinetic simulations, are needed before concluding this could be related to the resonant behaviour of electron transport observed in some tokamaks.

Acknowledgements. Fruitful discussions with Drs. T.S. Hahm and Y. Idomura are gratefully acknowledged. This work was partly supported by the Swiss National Science Foundation.

References

[1] DIMITS A.M., BATEMAN G., BEER M.A., et al., Phys. Plasmas **7** (2000) 969.
[2] HAMMETT G.W., BEER M.A., DORLAND W., COWLEY S.C., SMITH S.A., Plasma Phys. Controlled Fusion **35** (1993) 973.
[3] SYDORA R.D., DECYCK V.K., DAWSON J.M., Plasma Phys. Controlled Fusion **38**, (1996) A281.
[4] ROSENBLUTH M.N., HINTON F.L., Phys. Rev. Lett. **80** (1998) 724.
[5] HAHM T.S., Phys. Plasmas **3**, (1996) 4658.
[6] DIMITS A.M., LEE W.W., J. Comput. Phys. **107** (1993) 309.
[7] HATZKY R., TRAN T.M., KÖNIES A., KLEIBER R., ALLFREY S.J., Phys. Plasmas **9** (2002) 898.
[8] ALLFREY S.J., BOTTINO A., SAUTER O., VILLARD L., New Journal of Physics **4** (2002) paper no.29, http://www.njp.org.
[9] KIM J.Y., HORTON W., DONG J.Q., Phys. Fluids B **5** (1993) 4030.
[10] ZONCA F., CHEN L., DONG J.Q., SANTORO R.A., Phys. Plasmas **6** (1999) 1917.
[11] JENKO F., SCOTT B.D., Phys. Rev. Lett. **80** (1998) 4883.
[12] VILLARD L., BOTTINO A., SAUTER O., VACLAVIK J., Phys. Plasmas **9** (2002) 2684.
[13] BRUNNER S., FIVAZ M., TRAN T.M., VACLAVIK J., Phys. Plasmas **5** (1998) 3929.
[14] DONG J.Q., CHEN L., ZONCA F., Nucl. Fusion **38** (1999) 1041.

On the Potentiality of Using Ferritic/Martensitic Steels as Structural Materials for Fusion Reactors

N. Baluc

Centre of Research in Plasma Physics, Fusion Technology Materials,
Swiss Federal Institute of Technology - Lausanne,
Association EURATOM - Swiss Confederation
ODGA/105, 5232 Villigen-PSI, Switzerland

e-mail contact of author: nadine.baluc@psi.ch

Abstract. Reduced activation ferritic/martensitic (RAFM) steels are the reference as structural materials for the future fusion reactors. They have proven to be a good alternative to austenitic steels for their higher swelling resistance. However, RAFM steels exhibit irradiation-induced low temperature hardening and increase in the ductile-to-brittle transition temperature, which imposes a severe restriction on their reactor applications at temperatures below 300°C. Furthermore, a high density of small helium bubbles has been recently evidenced in specimens proton-irradiated at about 300°C to a dose of 10 dpa, which could affect their fracture mechanical behavior at intermediate temperatures. Their temperature window of use is presently limited by a drop in mechanical strength at about 600°C. So, new variants that can better resist at high temperatures, are currently being developed, mainly using a stable oxide dispersion. The potentiality of using present RAFM steels and the variants being developed for the first wall of future fusion reactors are reviewed below.

1. Introduction

In fusion reactors, the first wall and breeding-blanket components will be exposed to plasma particles and electromagnetic radiation and will suffer from irradiation by 14 MeV neutrons. The high energy neutrons will produce displacement damage (via displacement cascades) and impurities (i.e. H and/or He atoms) via transmutation nuclear reactions within structural materials. Key parameters for the first wall in fusion power reactors (fusion power: 3-4 GW, operational mode: quasi-continuous) are the following [1]: total neutron flux: 10-15x10^{14} n/cm^2.s; neutron wall loading: 2-3 MW/m^2; integrated wall load: 10-15 MWy/m^2 (100-150 dpa in steels); surface heat load: 0.1-1 MW/m^2; volume power density: 20-30 W/cm^3; maximum irradiation temperature: $\geq$ 650°C; gas production rates: 10-15 appm He/dpa, 40-50 appm H/dpa (in steels).

2. Structural Materials for First Wall and Breeding-Blanket Applications

Candidate structural materials for first wall and breeding-blanket applications have a chemical composition that is based on low activation elements (Fe, Cr, V, Ti, W, Ta). They include mainly reduced activation ferritic/martensitic (RAFM) steels, vanadium alloys and SiC/SiC ceramic composites. Among them, the RAFM steels are presently considered as the most promising structural materials, as they have achieved the greatest technical maturity, i.e. qualified fabrication routes, welding technology and a general industrial experience are already available. The RAFM steels that are currently under extensive investigation include two large casts of F82H and EUROFER 97 and laboratory casts of the series of OPTIMAX alloys. The F82H steel was developed in Japan. It is investigated as part of the IEA (International Energy Agency) Fusion Materials Internationally Coordinated Program on ferritic/martensitic steels. The F82H steel contains 7.65 wt.% Cr, 2 wt.% W, Mn, Mo, V, Ta, Si and C below 1 wt.% in sum total, and Fe for the balance. The EUROFER 97 steel was developed in Europe within the EFDA (European Fusion Development Agreement) Program. Its chemical composition is the following: 8.93 wt.% Cr, 1.07 wt.% W, Mn, Mo, V, Ta, Si

and Cr below 1 wt.% in sum total, and Fe for the balance. The RAFM steels known as OPTIMAX steels were developed by the Fusion Technology Materials (FTM) group of the Centre of Research in Plasma Physics (Association EURATOM-Swiss Confederation) [2]. They contain about 9 wt.%Cr and their detailed composition results from optimisation of previous 12 wt.% Cr steels, as MANET for instance, where Ni, Mo and Nb have been replaced by the W, V and Ta low activation elements.

3. Advantages and Drawbacks of RAFM Steels

3.1. Advantages

In addition to their favorable cost, availability and engineering data base, the RAFM steels present a lower activation than stainless steels and a better surface heat capability (4.32 KW/K.m at ambient temperature for F82H, i.e. three times that of stainless steels) due to their lower coefficient of linear thermal expansion and higher coefficient of thermal conductivity [3]. At temperatures above 300°C, the RAFM steels are expected to exhibit a good resistance to swelling (1 vol.% per 100 dpa as compared to 1 vol.% per 10 dpa in stainless steels).

3.2. Drawbacks

The RAFM steels exhibit a drop in tensile strength at about 600°C [4], a strong reduction in creep strength at temperatures above 600°C and a significant stress softening in low cycle fatigue tests. In addition, the RAFM steels have a bcc structure and, like other materials of this type, they exhibit a ductile-to-brittle transition temperature (DBTT). In the unirradiated state, the DBTT of RAFM steels lies well below room temperature, that is between -80 and -90°C for the F82H, OPTIMAX A and EUROFER 97 alloys.

3.3. Effects of Irradiation

Irradiation at temperatures below 300-350°C leads to strong hardening and loss of ductility (see Figure 1, [5]), i.e. to embrittlement. Transmission electron microscopy (TEM) observations showed that the strong radiation hardening evidenced for RAFM steels at irradiation temperatures below about 300-350°C seems to correlate with the irradiation-induced dislocation loop microstructure (size and density evolution as a function of dose) rather than with the helium amounts produced (see Figure 2, [6]). The DBTT also increases drastically, as for instance up to -5°C for OPTIMAX A neutron-irradiated at 250°C to 2.5 dpa (see Figure 3, [5]) and up to +53°C for F82H neutron-irradiated at 300°C to 2.5 dpa. Neutron irradiation at temperatures below 300°C to 100-150 dpa is expected to yield a DBTT well above room temperature. At higher irradiation temperatures, the DBTT is not expected to increase significantly [3]. The effects of high He/dpa ratio still need to be investigated. A high density of small helium bubbles (about 1nm) has been recently evidenced using TEM (see Figure 4) in specimens of the F82H steel that were irradiated in SINQ (the Swiss Spallation Neutron Source, neutron-proton mixed spectrum, gas production rates: 50 appm He/dpa and 450 appm H/dpa in steels) at about 300°C to a dose of 10 dpa [6]. The impact of such a distribution of helium bubbles on the fracture properties of the F82H steel is under investigation. Preliminary mechanical test results seem to indicate that the helium amounts produced correlate well with the fracture behaviour of RAFM steels, i.e. a larger amount of helium yields a stronger rate of increase in the DBTT, at least at irradiation temperatures below about 300°C.

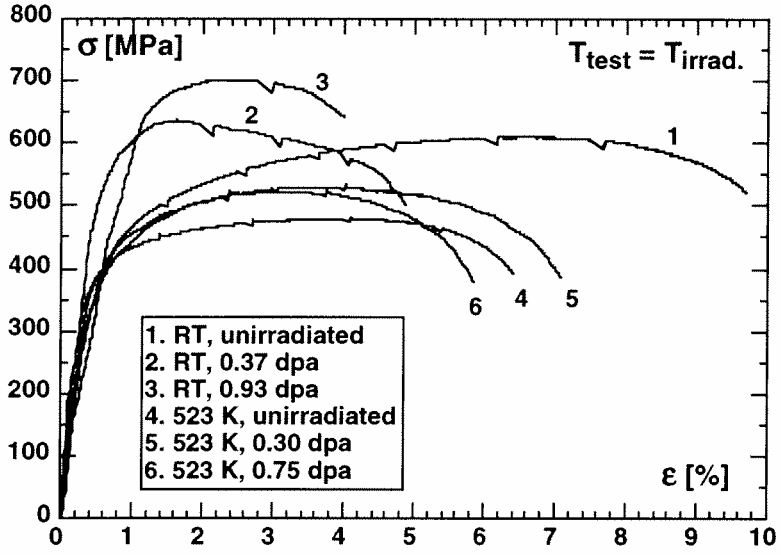

FIG. 1. Tensile stress-strain curves of unirradiated and proton-irradiated OPTIMAX A, after [5].

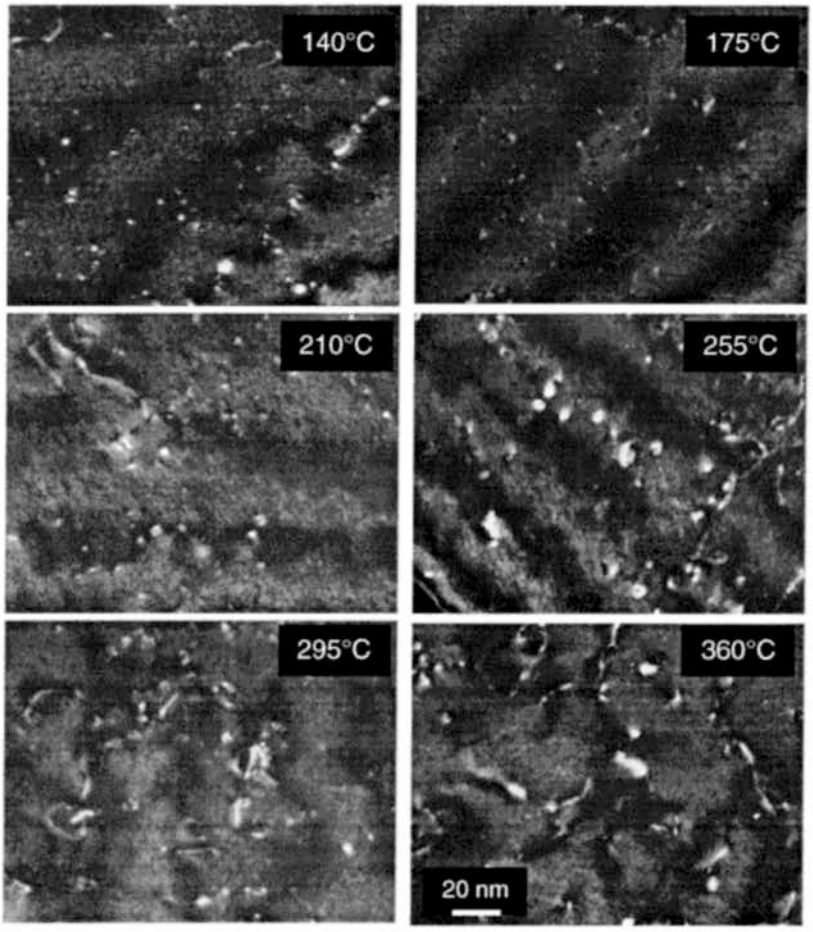

FIG. 2. Irradiation-induced dislocation loops of interstitial type in F82H irradiated in SINQ at various temperatures to about 10 dpa, after [6].

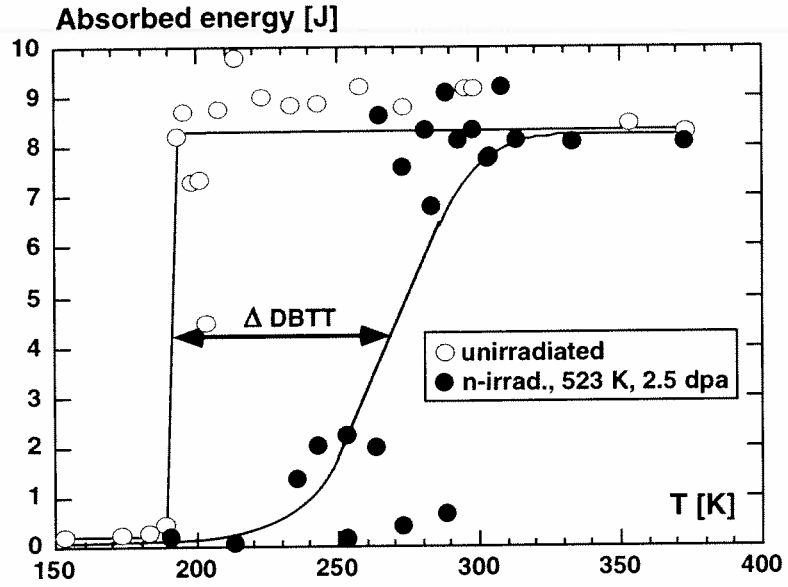

FIG. 3. Charpy impact energy versus temperature for OPTIMAX A, before and after neutron-irradiation at 250°C to 2.5 dpa, after [5].

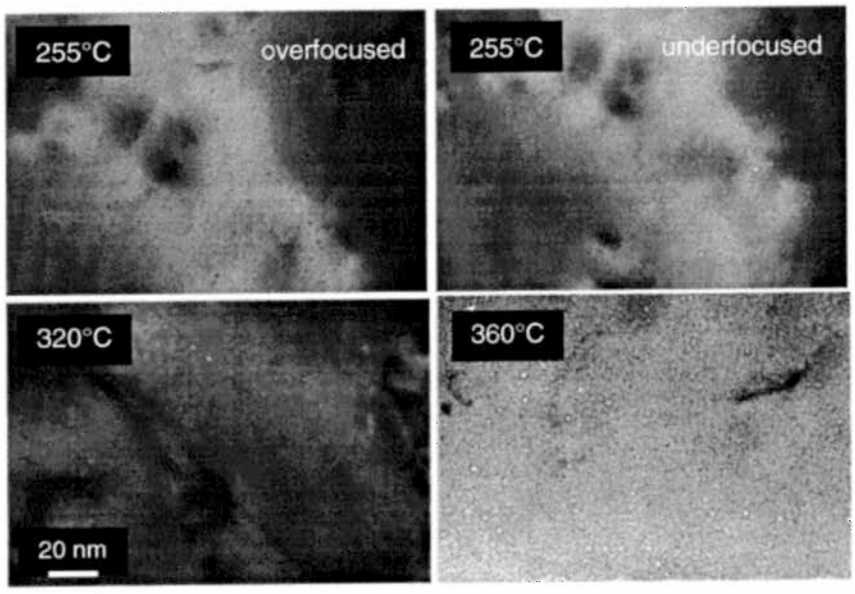

FIG. 4. Irradiation-induced helium bubbles in F82H irradiated in SINQ at various temperatures to about 10 dpa, after [6].

3.4. Summary

In summary, the temperature window of use of RAFM steels is presently approximately 350-550°C, the lower value being limited by irradiation-induced embrittlement effects and the upper limit by a strong reduction in mechanical strength. To decrease the lower temperature limit involves decreasing the DBTT before irradiation. If one may expect to lower the DBTT value by acting upon the composition and/or the impurity level, it seems unrealistic to obtain a DBTT below room temperature after neutron irradiation at temperatures below 300°C to doses of about 100-150 dpa. One way to get round this problem would consist in maintaining the temperature above 350°C and/or to anneal regularly the fusion reactor at high temperature

to recover the DBTT obtained in unirradiated conditions. On the other hand, it is expected that adding a fine dispersion of strong particles to the RAFM steels could contribute to increase the upper temperature limit. ODS (Oxide Dispersion Strengthened) steels with the EUROFER 97 as matrix material and Y_2O_3 particles as reinforcement material are currently under development in Europe in the frame of the EFDA Program. Preliminary mechanical test results [7] showed a significant shift of the mechanical strength to higher temperatures, but unfortunately they also revealed a strong increase in the unirradiated DBTT value, with respect to the EUROFER 97. Obviously, fabrication routes still need further improvement.

4. Conclusion

This paper shows the need to promote a strong dialog between reactor designers and material science experts to define a reactor concept which takes into account the constraints imposed by potential materials as well as engineering and economical considerations. While the use of existing irradiation facility such as SINQ can provide useful data on materials, the availability of an intense source of 14 MeV neutrons, such as IFMIF (International Fusion Materials Irradiation Facility), is a requisite for the final qualification of the selected materials.

5. References

[1] EHRLICH, K., 'The Development of Structural Materials for Fusion Reactors', Phil. Trans. R. Soc. Lond. A **357** (1999) 595.

[2] VICTORIA, M., et al., ,The Microstructural Stability and Mechanical Properties of Two Low Activation Martensitic Steels', (Proc. 17th ASTM Symp. on Effects of Radiation on Materials), (GELLES, D.S., Ed.), ASTM, Philadelphia (1995) 721.

[3] TAVASSOLI, F., 'Presents Limits and Improvements of Structural Materials for Fusion Reactors', J. Nucl. Mater, to appear (2002).

[4] SPÄTIG, P., BALUC, N., 'Proton Irradiation up to 1 dpa of Plate, for He Effect Testing', (Report on EFDA Task TW1-TTMS-001 deliverable 3), (2001).

[5] BALUC, N., et al., 'The Mechanical Properties and Microstructure of the OPTIMAX Series of Low Activation Ferritic-Martensitic Steels', J. Nucl. Mater. **283-287** (2000) 731.

[6] JIA, X., et al., 'The Impact of Irradiation Temperature on the Microstructure of F82H Martensitic/Ferritic Steel Irradiated in a Proton and Neutron Mixed Spectrum', J. Nucl. Mater. 305 (2002) 1.

[7] SCHÄUBLIN, R., et al., 'Microstructure and Mechanical Properties of Two ODS Ferritic/Martensitic Steels', (Proc. 10th International Conference on Fusion Reactor Materials), to appear in J. Nucl. Mater. (2002).

Recent Results from R&D on Superconductors at CRPP

P. Bruzzone, R. Wesche, B. Stepanov, M. Vogel

Centre de Recherches en Physique des Plasmas, Association Euratom-Confederation Suisse, Ecole Polytechnique Federale de Lausanne, CH-5232 Villigen-PSI, Switzerland

E-mail: pierluigi.bruzzone@psi.ch

Abstract. Prototype conductors for the ITER magnets have been tested extensively in the SULTAN facility at CRPP in the last decade. The in depth characterization of the high current carrying conductors provided a valuable feedback in the design, with performance optimization and cost reduction. From the transient stability results, the temperature margin required to withstand the plasma disruption has been found to be much smaller than originally assumed. A comparison between two specially designed conductors showed that the copper fraction in the superconducting Nb_3Sn composite can be reduced without affecting the stability, leading to a substantial reduction of the overall amount of superconducting composite to be procured for the ITER magnets. AC loss measurements carried out over a broad range of frequency, brought evidence of two regimes of losses, complementing the test results of the ITER model coils and indicating that the correct eddy currents loss to be retained in the design for plasma disruption and initiation is much smaller than the value extrapolated from the slow charge of the model coils. Other results on current distribution, cyclic load and joint performance are briefly reported.

1. Introduction

In the early eighties, the construction of a high field test facility started in Villigen (North-West Switzerland) as a joint effort of a Swiss, Italian and Dutch Team, under the sponsorship of EURATOM. The nickname SULTAN was given as an acronym of the German SUpraLeiter TestANlage. The facility evolved into a split coil of three pairs of graded, NbTi and Nb_3Sn coils with high field access for straight conductor samples, powered by a 100 kA superconducting transformer. The superimposed, pulsed field capability was also added. SULTAN is now the world wide reference test facility for large, force flow superconductors, with dc field up to 11 T, superimposed, quasi steady state, ac field up to ± 0.5 T, superimposed transient field up to 4 T, 140 ms and a broad range of operating temperature and mass flow rate [1].

During the ITER EDA and CTA, a dozen of full size conductors and joints (prototypes of model coils, inserts and busbar conductors, made of Nb_3Sn, Nb_3Al and NbTi) have been tested as a short, straight samples. Seven subsize cable-in-conduit conductor samples of NbTi and Nb_3Sn have been prepared at CRPP and tested in the frame of parametric studies. Two experiments with coiled conductor samples have been also carried out in the 600 mm bore of the SULTAN magnets, the QUELL (QUench Experiment on Long Length) [2] and the SeCRETS (Segregated Copper Ratio Experiment on Transient Stability) [3]. About half of the samples are prepared outside of CRPP by international teams from EU, JA , US and RF, who participate to the test activity in SULTAN. The sections below summarize the design relevant results from selected tests carried out recently in SULTAN.

2. Transient Field Stability and Segregation of Stabilizer

The issue of transient stability has drawn lot of attention in the ITER conductor design, leading, in the initial phase, to a very conservative attitude, e.g. retaining a temperature margin of 2 K because of the unknown behavior at plasma disruption and imposing a large copper fraction in the Nb_3Sn composite strand.

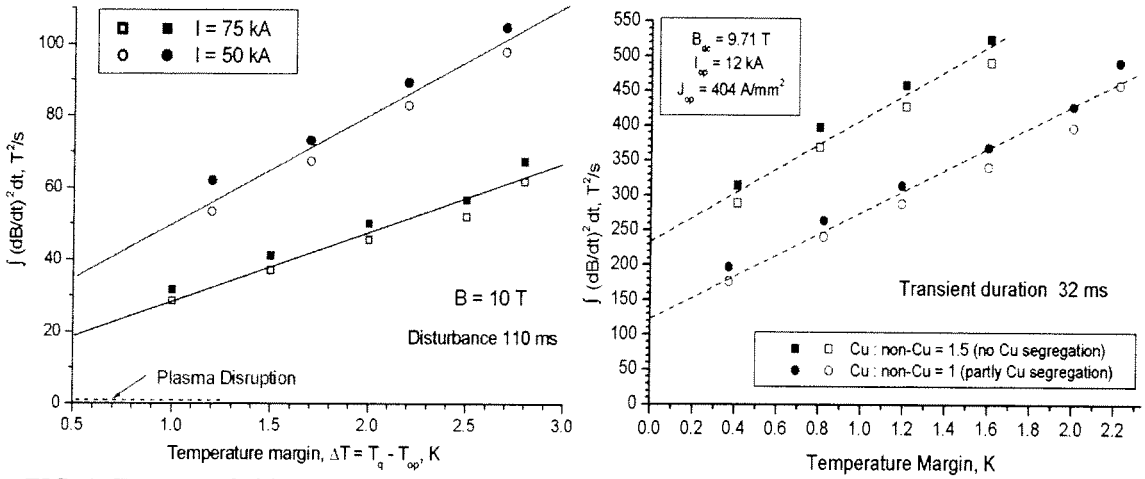

FIG. 1. Transient field stability results on a Nb_3Sn CS model coil conductor(left) and on two Nb_3Sn subsize conductors identical except the location of the stabilizer(right)

During the test in SULTAN of a model coil conductor, large field transients, well above the plasma disruption events, have been applied under relevant operating conditions, proving, see Fig 1 left, that a very marginal temperature margin is necessary to withstand a field transient like the plasma disruption [4]. Encouraged by this result, another transient field experiment has been carried out, where two Cr plated Nb_3Sn cable-in-conduit conductors (CICC) are series connected and exposed to the same pulsed field. The only difference between the two CICCs is the location of the stabilizer, either homogeneously distributed in the composite with Cu:non-Cu = 1.5, or partly segregated , with Cu:non-Cu = 1 in the composite and other Cu wires bundled in the cable. The result, see Fig. 1 right, proved that, although the segregated copper marginally contributes to transient stability, the Cu:non-Cu = 1 is largely sufficient for the ITER stability requirement [3].

Dropping the Cu:non-Cu ratio from 1.5 to 1 means to reduce by 20% the amount of strand to be procured, by keeping unchanged the "non-Cu" current carrying cross section. Besides the advantage in the procurement time scale, a large cost economy, of the order of 100 M€, is also obtained as the market price of the Nb_3Sn strand does not depend on the Cu:non-Cu ratio. The evidence that large field transient can be withstood with marginal temperature increase can be used to either reduce the overall margin (i.e. the conductor price) or to re-allocate the margin for other unexpected effects observed in the conductor and model coil test [5].

3. Stability and Heat Transfer Coefficient

The ability to effectively transfer heat from the superconducting strand to the coolant is a key feature of the cable-in-conduit conductors. The heat transfer coefficient, h, together with the stabilizer cross section, A_{cu}, and the wet perimeter, p_w, determine the "limiting" current, I_{lim},

$$I_{lim} = \sqrt{A_{cu}\, p_w\, h\, (T_c - T_{op})/\rho_{Cu}}$$

i.e. the maximum operating current at which an instantaneous disturbance (energy input) can be recovered without causing an irreversible runaway [6]. Above I_{lim}, any small disturbance, e.g. a microscopic strand movement in the cable, may cause a sudden take-off (quench) and the conductor is said to be "unstable" or to have "unstable" transition.

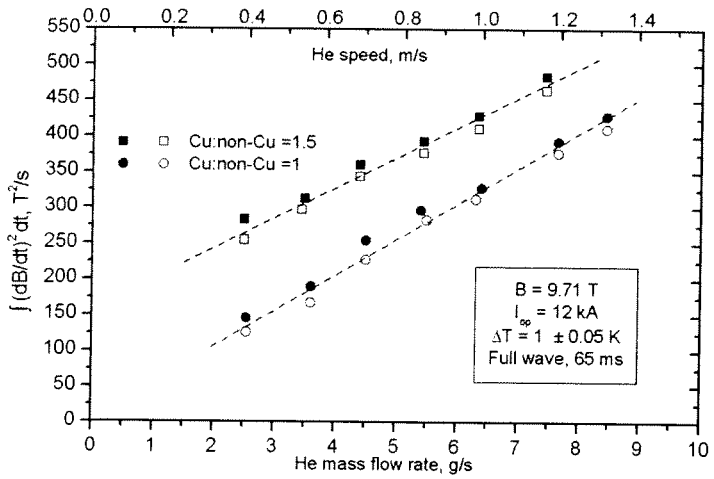

FIG. 2. Transient field stability results on two Nb_3Sn CICC as a function of the coolant speed

The heat transfer coefficient strongly depends on the helium turbulence at the strand surface (Dittus-Bölter correlation), however in the ITER design criteria, a low value of h is retained, corresponding to the quasi-stagnant helium condition (600 – 1000 W/K·m^2). In the ITER Nb_3Sn CICC, we never observed an unstable transition, even at reduced stabilizer cross section, also due to the broad transition (low n index [7]) and hence large $?T = T_c - T_{cs}$. However, the impact of the helium speed (and hence h) on the ability of the Nb_3Sn CICC to recover after an energy input was observed in the transient field stability experiment [3], see Fig.2, where the disturbance duration (65 ms) is longer than for a strand movement (< 10 ms).

In NbTi CICCs, unstable transitions are observed above a threshold current density which can be assessed as J_{lim}. Below J_{lim}, blue dots in see Fig.3, the CICC results scale satisfactorily compared to the strand J_c (green lines). Above J_{lim}, the CICC performance (red dots = I_q) deviates progressively from the strand data. The only difference between the two CICCs in Fig. 3 is the strand coating: the CICC with low resistivity coating (SnAg) has a higher threshold for unstable transition, 800 vs. 550 A/mm^2, which is an evidence of a more effective interstrand current sharing (on the other hand, the CICC with SnAg coating has much higher ac loss and hence a very poor transient field stability [8]).

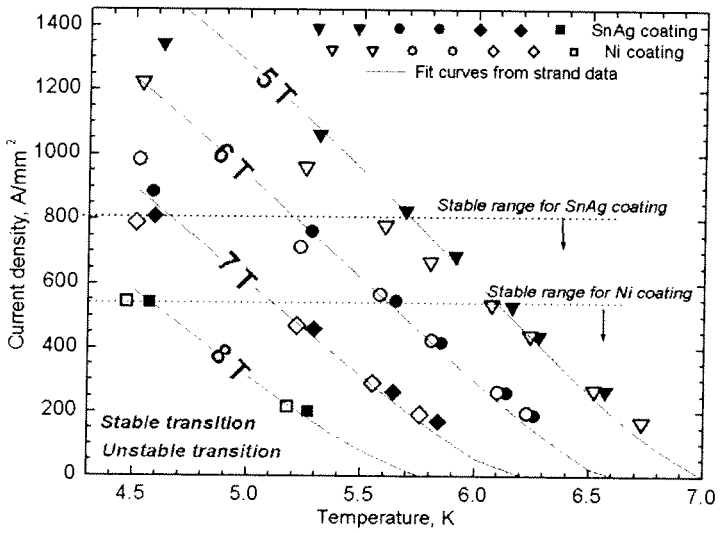

FIG. 3. DC performance of two NbTi CICCs without central hole, identical except the strand coating, revealing the threshold between stable and unstable transition

The presence of a pressure release channel in the CICC drastically reduces the coolant speed in the strand bundle area for the same overall mass flow rate. The impact on the stability is dramatic. A NbTi full size ITER conductor (with central hole) tested in SULTAN in 2002 showed a threshold for stable to unstable transition, i.e. J_{lim}, in the range of 150 A/mm^2 [9] compared to the 550- 800 A/mm^2 observed in the conductor without central hole. The effect of the coolant speed on h and hence on J_{lim} is much stronger than the Cu to non-Cu ratio. In fact, the conductor with central hole and J_{lim} ~ 150 A/mm^2 has Cu:non-Cu ~ 1.9, compared to Cu:non-Cu ~ 1.05 in the conductor without central hole and J_{lim} ~ 550 A/mm^2 (both conductors have the same void fraction and Ni strand coating).

5. AC Loss

The coupling loss characterization of a superconductor is aimed to identify the coupling loss constant, $n\tau$, to be used in the loss formulae. In large multistage CICCs, several induced current loops of different size overlap with multiple time constants. The extrapolation of the coupling loss from a low frequency range (e.g. the charge and discharge of a large coil) to a short time scale event (e.g. plasma disruption and initiation) may lead to large errors as the loops with large time constant are fully screened in short time scale events. In SULTAN, the ac loss can be measured over a broad range of frequency, from 0.03 to 6 Hz by combined calorimetric and magnetization methods [10].

For CICCs of Cr coated Nb_3Sn strands with void fraction about 36%, the loss curve in linear and logarithmic scale is shown in Fig. 4. For field changes on a time scale shorter than 4 – 5 s ($f > 0.2$ Hz), the coupling loss is very small, substantially restricted to the interfilament loss, with $n\tau$ of the order of 1 to 3 ms. This result is independent on the loading history. On the opposite, the energy loss for slow time varying field, with time scale of the order of 10 to 1000 seconds (e.g. the coil charge) is large, with not really predictable $n\tau$. After cyclic operation, the interstrand resistance increases and the large current loops may vanish locally, in the most heavily loaded sections of the winding. However, in average, the overall decrease of the coil loss after many load cycles may be not dramatic.

In NbTi, the effect of strand coating on the ac loss is investigated as a function of the load history, see Fig. 5. The two CICC samples with 336 strands are identical, except the strand coating, either Ni or low resistivity SnAg. The results indicate that the Ni coating is the best choice, with low ac loss, weakly changing upon the initial load cycles. In the SnAg coated sample, the ac loss is initially very large and keeps decreasing after a large number of cycles.

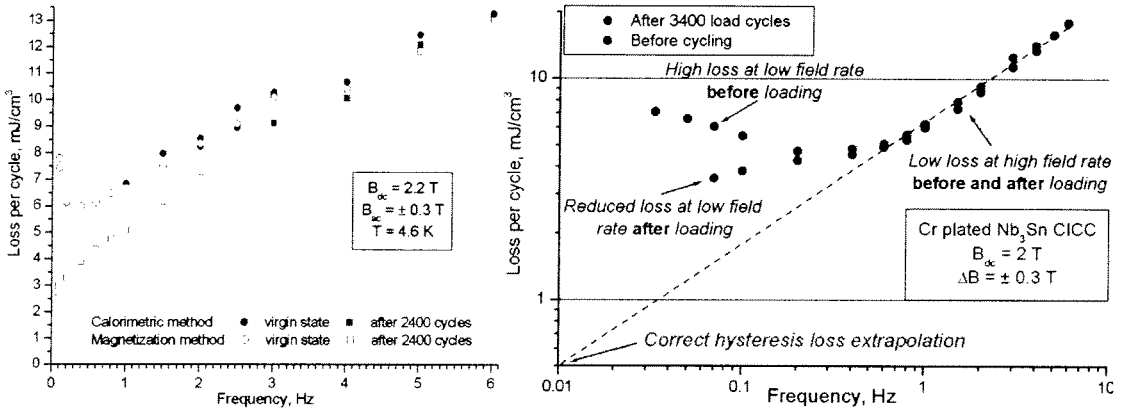

FIG. 4. AC loss in linear (left) and logarithmic scale (right) for Cr coated Nb_3Sn CICC under different load conditions

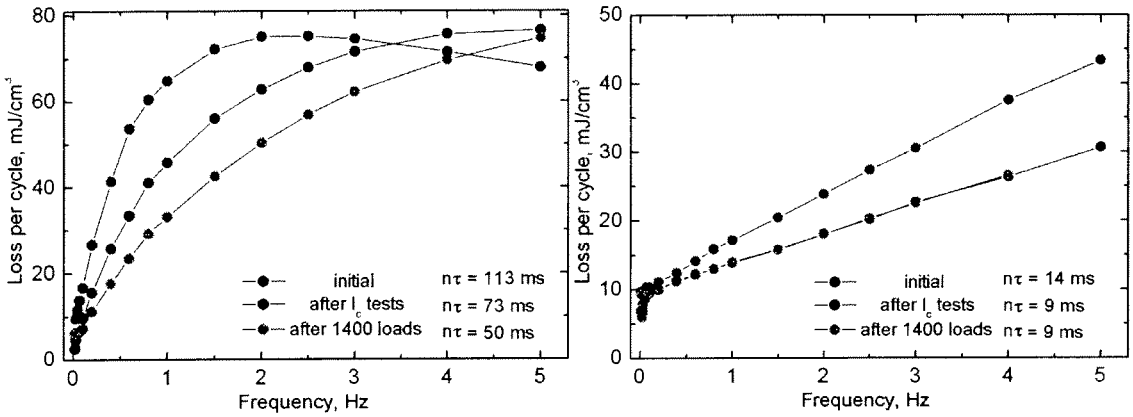

FIG. 5. AC loss of two NbTi CICC with either SnAg coating (left) or Ni coating (right) at different steps of the load history

6. Conclusion

The results obtained in several R&D tasks carried out in the SULTAN test facility have improved the knowledge of the ITER conductor behavior under realistic operating conditions. A refinement of the design criteria, leading to higher reliability and reduced cost, is obtained in the field of transient field stability (margin for plasma disruption), ac loss (actual loss constant to be retained for critical, fast events) and limiting current (impact of coolant speed on stability).

7. References

[1] BRUZZONE P., Anghel A., Fuchs A.M., Pasztor G., Stepanov B., Vogel M., Vecsey G., 'Upgrade of Operating Range for SULTAN Test Facility', IEEE Appl Supercon **12**, 520 (2002)

[2] ANGHEL A., 'QUELL Experiment: Analysis and Interpretation of the Quench Propagation Results', Cryogenics **38**, 459 (1998)

[3] BRUZZONE P., Anghel A., Fuchs A.M., Stepanov B., Vecsey G., Zapretilina E., 'Test Results of SeCRETS, a Stability Experiment about Segregated Copper in Cable-in-Conduit Conductors', IEEE Appl. Supercon **11**, 2018 (2001)

[4] BRUZZONE P., 'Stability under transverse Field Pulse of the Nb_3Sn ITER Cable-in-Conduit Conductors', IEEE Appl Supercon **10**, 1062 (2000)

[5] MITCHELL N., 'Summary, Assessment and Implications of the ITER Model Coils Test Results', presented at SOFT 22, Helsinki, September 2002

[6] BOTTURA L., 'Stability and protection of CICCs: an updated Designer's View' Cryogenics **38**, 491 (1998)

[7] BRUZZONE P., Stepanov B., Wesche R., 'The voltage current characteristic (n value) of the cable-in-conduit conductors for fusion', to be published in IEEE Appl Supercon **13**

[8] BRUZZONE P., Stepanov B., Wesche R., Vogel M., Gloor Th., 'Parametric Studies of Subsize NbTi Cable-in-conduit Superconductors for ITER FEAT', to be published in IEEE Appl Supercon **13**

[9] SALPIETRO E., 'Superconducting Coils for Fusion Devices : R&D Needs', Presentation at CHATS 2002, Karlsruhe September 2002

[10] BRUZZONE P., 'Coupling currents loss in Nb_3Sn cable-in-conduit conductors' IEEE Appl Supercon **12**, 524 (2002)

Control of the Sawtooth Instability by Electron Cyclotron Heating and Current Drive In the TCV and ASDEX Upgrade Tokamaks.

T.P. Goodman 1), A. Mück 2), C. Angioni 1), M.A. Henderson 1), O. Sauter 1), F. Ryter 2), E. Westerhof 3), H. Zohm 2) and the ASDEX Upgrade Team 2)
1) Centre de Recherches en Physique des Plasmas, Association EURATOM - Confédération Suisse, Ecole Polytechnique Fédérale de Lausanne, CH-1015 Lausanne, Switzerland
2) Max-Planck-Institut für Plasmaphysik, IPP-EURATOM Ass., 85748 Garching, Germany
3) FOM-Instituur voor Plasmafysica "Rijnhuizen", Ass. EURATOM-FOM, TEC, PO Box 1207, 3430 BE Nieuwegein, NL

e-mail contact of main author: timothy.goodman@epfl.ch

Abstract: Recently, there has been increased interest in avoiding the destabilization of NTMs by controlling the sawtooth instability which frequently provides a large enough seed island to trigger the growth of the NTM. Electron cyclotron heating (ECH) and current drive (ECCD) are prime candidates for such control as the all important deposition location can be adjusted using external control parameters alone. Sawtooth control studies have been carried out on the Tokamak à Configuration Variable (TCV) and ASDEX Upgrade tokamaks. The experiments and subsequent sawtooth period modeling help to determine the optimum locations for sawtooth period control and understand the mechanism by which this control is attained.

1. Introduction

The stabilization, or at least reduction to an insignificant amplitude, of NTMs at the q=2 and q=3/2 surfaces has been demonstrated in the past [1,2,3]. It has been shown experimentally that ion-cyclotron absorption can alter the sawtooth period. By adjusting the deposition location so as to shorten the sawtooth period, the plasma beta can be increased to higher levels than in the presence of longer sawteeth, before triggering an NTM [4].

Early experiments showed that electron cyclotron resonance absorption (ECH) near the q=1 surface can drastically alter the sawtooth period [e.g. 5]. Furthermore, TCV has shown that with absorption near the q=1 surface, electron cyclotron current drive (ECCD) driving current in the same direction as the plasma current (co-ECCD) lengthens the sawtooth period over that of pure ECH. Driving current counter to the direction to the plasma current (counter-ECCD) decreases the period. Control of the deposition location can be carried out by adjusting the magnetic field strength, to move the resonance relative to the q=1 surface itself as in the case of ICRH. However, the greatest potential advantage of ECH over ICRH is that the absorption location can be easily adjusted by changing external parameters (launcher mirrors) only, thereby becoming relevant to ITER operation.

In this paper sawtooth stabilization / destabilization refers to a lengthening / shortening of the sawtooth period; although, the sawtooth crash can also be effectively eliminated by reducing the period and/or amplitude towards zero. We show the (de)stabilization of the sawtooth instability by ECH and by co- and counter- ECCD on TCV, using real-time antenna steering; and on the ASDEX Upgrade tokamak, by adjusting the magnetic field strength. The relative merits of co- and counter-ECCD are discussed and the optimum location for stabilization is shown by modeling to be outside of the q=1 surface for co-ECCD and ECH and inside this surface for strong counter-ECCD. This is consistent with the available experimental evidence. Preliminary results of a TCV experiment looking for a theoretically predicted optimum location for destabilization are also presented.

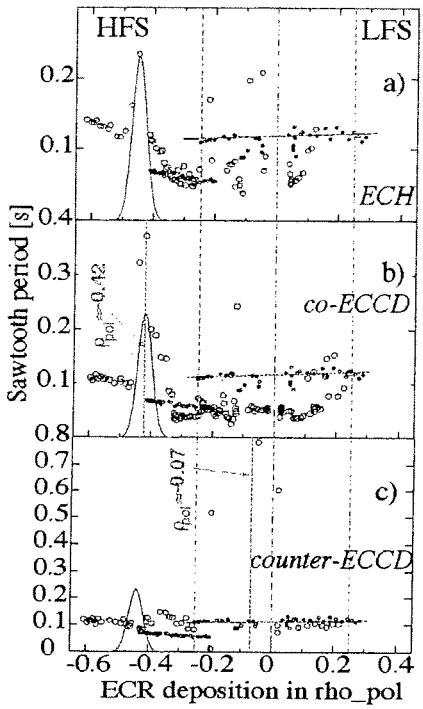

FIG. 1. Sawtooth period as a function of the deposition location for ECRH, co - and counter - CD. Vertical gray dashed lines are the HFS inversion radius, plasma center and LFS inversion radius (left to right). The locations of complete stabilization at fixed field are shown for co-CD (-0.42) and counter-CD (-0.07).

2. ASDEX Upgrade: Complete stabilization by ECCD in NBI heated plasmas [6]

In ASDEX Upgrade, stabilization has been achieved in single null, H-mode, NBI heated (ca. 5-5.3 MW), 0.8 MA plasmas using relatively low additional EC power (ca. 0.8-0.9 MW). The magnetic field is swept at a rate of ~0.1 T/s and moves the deposition location towards the LFS in time. Two gyrotrons are used with toroidal injection angles +/-15° for counter/co-ECCD, or with opposite signs for ECH. This ensures equivalent absorption locations and widths for the three cases. The results are summarized in Figures 1a-c, each showing combinations of shots with toroidal field sweeps for ECH, co- and counter- ECCD. The sawtooth period (red) is plotted versus the deposition location of the EC power in normalized radius (calculated by the TORBEAM code); $\rho_{pol} < 0$ indicates high field side (HFS) deposition. The sawtooth periods from NBI-only heated shots are shown in small points (blue), for reference. The step in the sawtooth period near the inversion radius is due to a change in the NBI sources [6]. A sample deposition profile is shown on each plot; scaled with the sawtooth period axis. It is chosen to match the sawtooth period peak height for ECH. It has been shown on TCV that when the sawtooth period is linear in ECH power density, the width of the peak in sawtooth period can be used as an approximate measure of the beam width [7, 8].

Heating and especially co-ECCD are stabilizing when absorbed near $\rho_{pol} = -0.42$; well outside of the sawtooth inversion radius of $\rho_{pol} = -0.25$. This peak in period is consistent with changing the growth rate of the shear at the q=1 surface (see below). The addition of co-ECCD further inside this peak, but still outside the inversion radius, ($|\rho_{pol}|$~0.25 - 0.35) decreases the sawtooth period relative to that measured with ECH (i.e. co-ECCD is destabilizing) while counter-ECCD increases the period. With counter-ECCD heating near $\rho_{pol} = -0.42$ produces sawtooth periods shorter than those found using ECH in accord with results on TCV. There is a broad stabilization region with near-central deposition, as shown in Figure 1c, consistent with a flattening of the central q-profile. The q=1 surface should still exist, however, as a m=1, n=1 mode is present. Complete stabilization was achieved with deposition at $\rho_{pol} = -0.07$. No direct measure of the current profile (MSE) was available for these shots.

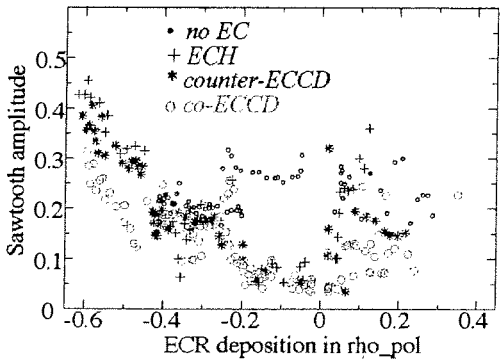

FIG. 2. Sawtooth amplitude as a function of deposition radius for the same swept magnetic field shots presented in Figure 1.

In Figure 2, the sawtooth amplitudes from the shots of Figure 1 are shown. For $\rho_{pol} < -0.42$, both the period and amplitude decrease in the order: ECH, counter-ECCD and co-ECCD. In other regions there are various sawtooth shapes similar to [9]. Note that there is a clear asymmetry between LFS and HFS deposition in both the sawtooth period and amplitude. This may be due to the generation of a larger trapped electron fraction when heating on the LFS.

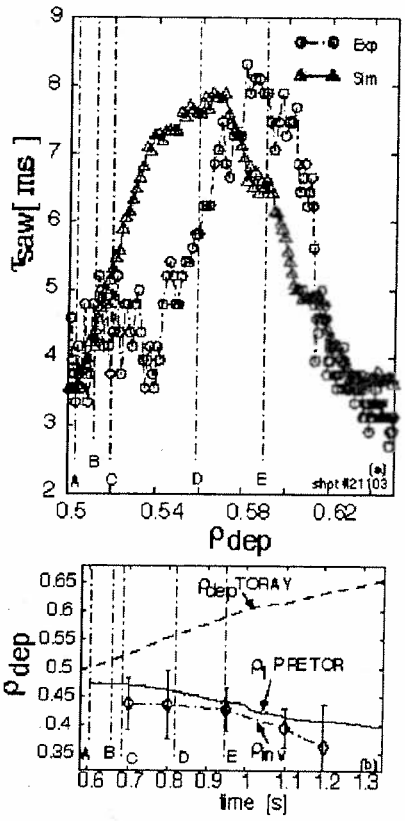

FIG. 3. Sawtooth simulations during swept ECH deposition accurately reproduces the TCV experimental sawtooth period (a) and the q-profile evolution (b). The horizontal scale of figure (a) corresponds to 15% of the plasma radius. The maximum in the sawtooth period (D/E) is found with the deposition well outside the inversion radius and the q=1 surface.

3. TCV: Optimum absorption location for sawtooth stabilization

In sweep experiments which use only external control parameters (i.e. no magnetic field sweep) and which cover the largest possible range of ρ_{dep}, it is difficult to combine several independent beams at precisely the same ρ_{dep}; especially when aiming from above and below the plasma midplane. The resonance should pass through the plasma center and thus the transverse dimension of the beam is nearly perpendicular to the flux surfaces as $\theta_{pol} \sim \pm 90°$. If the resonance is roughly tangent to the flux surface at the deposition location, (i.e $\theta_{pol} \sim 0°$ or 180°) ρ_{dep} is relatively insensitive to aiming angles and beam width.

While plasmas swept vertically through an ECH beam have been used to improve the accuracy of the LIUQE equilibrium reconstruction code [10] and therefore the ability to overlap multiple beams; some systematic discrepancies between magnetic and tomographic measurements [11] remain to be elucidated and absolute measurements below ± 5% of minor radius are not possible. Nevertheless, sweeps still provide precise, reproducible, *relative* measurements. The sensitivity of the sawtooth period to power density is used to align launchers, in situ, to within ~±10% of the beam width (i.e. ±1% minor radius) at TCV [7]. Fortunately, sawtooth period modelling can provide testable predictions based on relative measurements.

Sawtooth experiments are analyzed using the PRETOR-ST [8 and Ref.s therein] transport code, linked to a sawtooth period model first proposed to predict the sawtooth period in an ITER burning plasma. Many stabilizing terms can be taken into account, and in this form, the model has been successful in correctly simulating the sawtooth period variation during *a)* experiments with swept ECH beams in TCV [12], *b)* NBI heated plasmas in JET [13] – with fast-particle stabilization of sawteeth – and *c)* ICRH/ICCD heated JET discharges with negligible fast-particle stabilization [8]. Moreover, the code can separate the influence of current drive from that of the accompanying heating [8]. In actual experiments, both are always present simultaneously.

Figure 3 shows that the calculated deposition location for optimum sawtooth stabilization is in good agreement with the experimental results using ~1.3MW of swept ECH in a plasma of $I_p \sim 350$kA, $\kappa \sim 1.7$, $\delta \sim 0.45$ and $n_{e0} \sim 3 \cdot 10^{19} m^{-3}$. The optimum is clearly outside the experimentally measured inversion radius (from x-ray tomography) and the q=1 surface (calculated self-consistently by PRETOR-ST). As the EC absorption moves outside of the q=1 surface, the q=1 radius decreases as also seen with the LIUQE equilibrium reconstruction code.

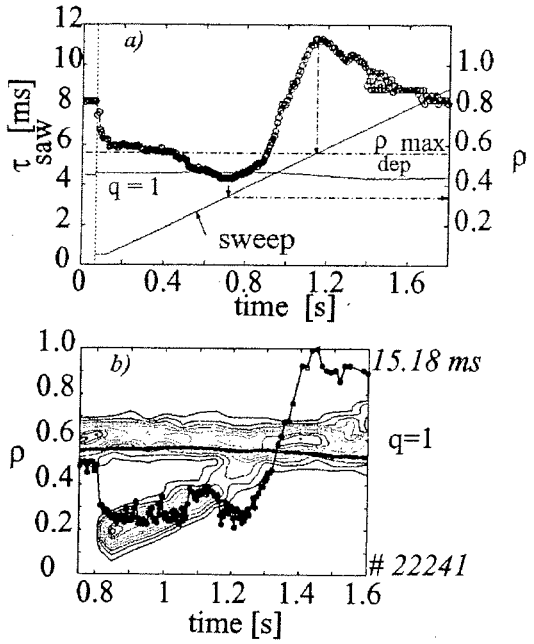

FIG. 4. a) Simulation: 1.3MW ECH fixed for optimum stabilization; 0.45MW of swept ECH. Sawtooth period, q=1 and ρ_{dep} are shown. b) Experimental sawtooth period, LIUQE q=1 (red line) and TORAY ECH power density contours: 0.9MW ECH (slight co-ECCD) fixed for optimum stabilization; 0.45MW of swept ECH (slight co-ECCD). ECH destabilizes sawteeth, inside q=1.

It is expected that the sawtooth model will show similar accord between ρ_{dep} and the sawtooth period for the ASDEX Upgrade results presented above. However, since the various NBI sources produce different sawtooth periods on ASDEX Upgrade, the model must now simultaneously simulate the effects of NBI stabilization, as well as the evolution of the shear at q=1 (s_1) and critical shear (s_{1crit}) due to ECH/ECCD: the crash condition for the later case being simply $s_1 > s_{1crit}$. While fast-particle stabilization may play a role during NBI heating, the different NBI sources have different deposition profiles and may also affect the sawteeth in the same way as the ECH. In addition, changes in the rotation profile can also affect the sawtooth period [14].

4. Predicted Optimum Location for Sawtooth Destabilization.

The stabilizing effect of Figure 3 can be eliminated by the addition of ~0.5MW of ECH absorbed at a fixed location $\rho_{dep} \sim 75\% \rho_{inversion}$ [8]; thus, ECH might be able to destabilize the long period sawteeth predicted in burning plasmas. PRETOR-ST predicts that the sawtooth period will exhibit a minimum (destabilization) at a distance inside the q=1 surface roughly equal to the Gaussian half-width of the ECH beam [8]. In the simulation, 1.35 MW are deposited at the optimum location for stabilization outside of q=1 while a fourth beam is swept from inside to outside the q=1 surface. The sawtooth period is calculated as a function of the deposition radius of the swept beam (Fig. 4a).

In a preliminary experiment to test this prediction, 0.9MW of power was used at fixed injection angle to simplify the overlap of the stabilizing beams. In addition, a small co-ECCD component due to the poloidal field is also present. This should cause the maximum found in the simulation (heating only) to shift slightly inward and the minimum slightly outward [8]. The additional co-ECCD will also increase the sawtooth period at the maximum relative to pure heating as shown on ASDEX Upgrade (Fig. 1). On TCV an additional beam was swept, similar to the simulation. The results are presented in Fig. 4b as a function of time and ρ. The EC power density contours are shown along with the LIUQE q=1 radius (thick red line). The saw-

tooth period (normalized to the maximum) is then overlaid as a function of time. Starting from the stabilized sawtooth period (t< 0.8s), *a)* the central beam is destabilizing (t>0.8s), *b*) a small minor peak is found (t~1.1s) and finally, *c*) the beam crosses the location of the other 2 beams (t>1.4s) with a further increase in the sawtooth period. Following the minor peak, a minimum is seen in the period (t~1.2s) but, the period is not shorter than that found at the start of the sweep (the sawtooth amplitude, however, exhibits a minimum only at t~1.2s).

When the central beam is added, a strong m=1, n=1 mode is present as in saturated sawteeth [9,15]. At the minor peak some similarities are seen with sawteeth interpreted as exhibiting partial magnetic reconnection [15] for which a more complete, 2D model of the sawtooth crash [16] is needed. Unfortunately, the 2D model used to match the sawtooth shape, cannot predict the sawtooth period.

5. Conclusions

Both TCV and ASDEX Upgrade show stabilization of the sawtooth period with power deposition outside of the inversion radius (and q=1 for TCV) as in the sawtooth model. The sawtooth model may be in accord with ASDEX Upgrade results showing sawtooth destabilization inside inversion radius with co-ECCD and stabilization with counter-ECCD. Modeling of ASDEX Upgrade results is still to be carried out and is complicated by simultaneous NBI heating effects. Preliminary TCV experiments to find the predicted optimum destabilization location inside q=1 show destabilization over a broad range of deposition locations and 2D sawtooth features which are out of the range of application of the sawtooth model used in PRETOR-ST.
This work was partly supported by the Swiss National Science Foundation.

6. References

[1] ZOHM, H., et al., Nuclear Fusion 39 (1999) 577.
[2] LA HAYE, R.J., et al., Phys. of Plasmas 9 (2002) 2051.
[3] ISAYAMA, A., et al., Plasma Phys. Control. Fusion 42 (2000) L37.
[4] SAUTER, O., et al., Phys. Rev. Lett. 88 (2002) 105001.
[5] HANADA, K., et al., Phys. Rev. Lett. 66 (1991) 1974.
[6] MÜCK, A., et al., in Proc. of 29th EPS Conf. on Plasma Phys. and Control. Fusion., Montreux, 2002 [ECA 26B (2002) P1.037].
[7] HENDERSON, M.A., et al., Fusion Engineering and Design, 53 (2001) 241.
[8] ANGIONI, C., et al., Submitted to Nuclear Fusion; ANGIONI, C., et al., in Proc. of 29th EPS Conf. on Plasma Phys. and Control. Fusion., Montreux, 2002 [ECA 26B (2002) P1.118].
[9] PIETRZYK, Z.A., et al., Nucl. Fusion 39 (1999) 587.
[10] GOODMAN, T.P., TCV Team, Proc. of IAEA-FEC, Sorento, 2000, [IAEA, Vienna (2001) EXP4/09].
[11] MLYNAR, J., et al., Lausanne Internal report LRP 732/02.
[12] ANGIONI, C., et al., in Theory of Fusion Plasmas, (Proc. Joint Varenna-Lausanne Int. Workshop) (Varenna 2000), edited by J.W. Connor, O. Sauter and E. Sindoni, ISPP-19 (Bologna, Editrice Compositori) (2000) 73.
[13] ANGIONI, C., et al., Plasma Phys. Control. Fusion 44, (2002) 205.
[14] GRAVES, J., et al., to be published in Theory of Fusion Plasmas (Proc. Joint Varenna-Lausanne Int. Workshop) (Varenna 2002), edited by J.W. Connor, O. Sauter and E. Sindoni, ISPP-20 (Bologna, Editrice Compositori) (2002).
[15] FURNO, I., et al., Nucl. Fusion 41 (2001) 403.
[16] PORCELLI, F., et al., Phys. Rev. Lett. 82 (1999) 1458.

ECH Power Deposition at 3rd Harmonic in high Elongation TCV Discharges Sustained by 2nd Harmonic Current Profile Broadening

A. Pochelon[1], G. Arnoux[1], Y. Camenen[1], A. Scarabosio[1], S. Alberti[1], F. Hofmann[1], A. Manini[1], R. Behn[1], P. Bosshard[1], P. Blanchard[1], S. Coda[1], T.P. Goodman[1], M.A. Henderson[1], J.-Ph. Hogge[1], A. Karpushov[1], J.-M. Moret[1], E. Nelson-Melby[1], L. Porte[1], O. Sauter[1], A. Sushkov[2], M.Q. Tran[1].

1) Centre de Recherches en Physique des Plasmas, Association EURATOM-Confédération Suisse, Ecole Polytechnique Fédérale de Lausanne EPFL, 1015 Lausanne, Switzerland
2) RRC Kurchatov, Moscow

e-mail contact of main author: Antoine.Pochelon@epfl.ch

Abstract. This paper summarises the present effort aimed at developing high elongation heated discharges and testing their confinement properties at normalised currents for which the highest ideal MHD βlimits are predicted. 2nd harmonic (X2) far off-axis ECH/CD is used to stabilise the plasma vertically at high elongation by broadening the current profile in stationary conditions (during the current flat top and over several current diffusion times). Current broadening is maximal for a power deposition in a narrow region (~a/5), for a finite toroidal injection angle and for high plasma density using upper lateral launchers to minimise refraction. In these discharges which are twice X2 overdense in the centre, 3rd harmonic (X3) is injected from a top launcher to deposit power in the centre and increase the central pressure, simultaneously with far off-axis X2. Using modulated X3, full absorption is measured by the diamagnetic probe. Absorption higher than calculated by thermal ray tracing is occasionally found, indicating absorption on the electron bulk as well as in the suprathermal electron population sometimes with a hollow deposition profile. The high sensitivity of the power coupling to the beam angle stresses the need for developing a mirror feedback scheme [1] to increase the coupling efficiency in transient heating scenarios.

1. Introduction

Plasma shaping, and in particular elongation, is a means to improve tokamak performance [2]. Highly elongated discharges tend to be vertically unstable and can only be stabilised by providing sufficient current density close to the plasma edge [3]. For Ohmic discharges, this is achieved by operating at a low safety factor q_{edge} ($2.2<\kappa<2.8$, $I_N=I_p/aB\sim2.8$-3.5MA/mT). However, in order to reach maximum β-values predicted by ideal MHD for highly elongated plasmas, one has to produce discharges at intermediate I_N values, of the order of 2MA/mT. For these values Ohmic discharges are vertically unstable, but TCV plasmas can be maintained stable by current profile broadening using far off-axis 2nd harmonic X-mode ECH/CD (X2) [4-7]. This leads to highly elongated discharges ($\kappa\sim2.48$) at low current and high safety factor ($I_N\sim1.05$MA/mT, $q_{edge}\sim10$) using 3/4 of the upper lateral port installed EC power [8]. X3 power has been coupled to the plasma in ohmic condition and in combination with X2 ECW [9-12]. In this paper we are using simultaneously far off-axis 2nd harmonic ECW for plasma shaping and 3rd harmonic (X3), with the aim of measuring and optimising the coupling of X3 power deposition.

2. Experimental set-up

TCV is equipped with 4.5MW ECH nominal power for 2s pulse length: 3MW at the 2nd harmonic and 1.5MW at the 3rd harmonic. The X2 system consists of six 475kW gyrotrons at 82.7GHz with six independent low field side (LFS) launchers, four upper lateral and two equatorial, steerable during the discharge. The X3 system consists of three 420kW gyrotrons at 118GHz using a single top launcher, also steerable during the discharge. The cut-off densities of X2 and X3 waves are 4.25 and 11.5 $10^{19}m^{-3}$ respectively.

Using power modulation techniques, the total absorbed power is measured by a diamagnetic loop (DML) [13,14], and the local deposition is measured with a 64 channels soft X-ray wire chamber (MPX) filled with Xenon, sensitive between 2-25keV (10% efficiency limits) [14,15]. The level of the suprathermal electron population is obtained by comparing HFS ECE radiation temperatures, $T_{e\,ECE}$, with the Thomson temperatures T_e [10].

3. High elongation stabilised by far off-axis ECH/CD X2

Typical time traces of a highly elongated plasma produced with off-axis ECH are shown in Fig. 1. X2 power is launched on a plasma with intermediate elongation, keeping the pre-programmed quadrupole and hexapole fields constant. The X2 power is deposited far off-axis ($\rho_{dep}=(V_{dep}/V_{max})^{1/2}>0.5$), using upper lateral launchers with a short beam path in the plasma to minimise refraction effects while the plasma reaches high elongation, Fig. 2. The local EC power deposition leads to a local increase in temperature and conductivity, hence to a broadening of the inductive current profile (ECCD and bootstrap currents are negligible, ~8% in this case). As a result, the plasma elongation κ increases on a typical current diffusion time (~0.2s). The main current profile indicator, the internal inductance l_i, decreases when the current profile is broadened or when the elongation is increased. The main contribution to the change in l_i is due to the current profile change (~3/4) [16]. The location of ECH deposition and the plasma first-pass power absorption are computed with the ray tracing code TORAY-GA [17]. The experimental results are compared to those of the fixed boundary transport code PRETOR [18] based on the Rebut-Lallia-Watkins model [18,19]. Both experiment and PRETOR simulation show that the optimal location of the EC power deposition for broadening the current profile is restricted to the region $0.55<\rho_{dep}<0.7$, Fig. 3 [16]. For $\rho_{dep}<0.55$, the current profile broadening effect is reduced, and for $\rho_{dep}<0.4$ the ECH power produces current profile peaking. For $\rho_{dep}>0.75$, the ECH power is both incompletely absorbed in the first-pass and inefficiently confined, reducing its effect on the current profile substantially. The values of the internal inductance computed by LIUQE and the ones computed by PRETOR differ slightly, due to the choice of the current profile functional in the LIUQE reconstructions, optimised for ohmic profiles. Operation at higher current I_N~2, and consequently higher ohmic power, requires proportionally more X2 power to broaden the current profile, hence the need for maximising the efficiency. The dependence of current profile broadening by off-axis X2 ECH on other parameters have been investigated [16].

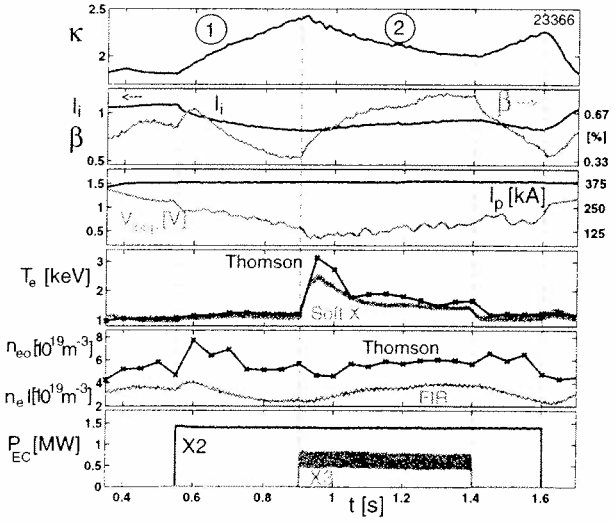

FIG. 1
Phase (1): preparation of a high n_e high κ target with far off-axis ECCD (X2) applied during the current plateau.
Phase (2): addition of X3 (0.63MW average, 50% modulation) to increase the central pressure.

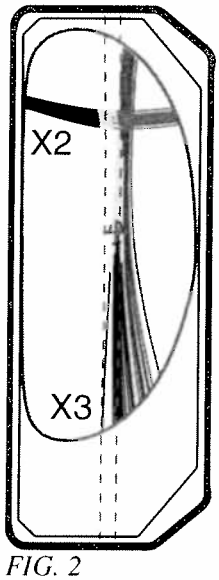

FIG. 2
Far off-axis X2 and X3 beams in elongated plasma (#23366, t=0.95s)

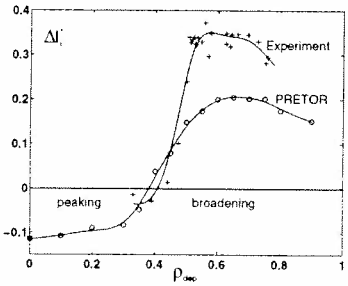

FIG. 3
Current profile change versus radial deposition location ρ_{dep} (I_p=300kA, P_{abs}=1MW, n_{e0}~2.5 $10^{19}m^{-3}$).

Operation at high plasma density, even overdense to X2 in the core, is observed to improve the efficiency of off-axis deposition for increasing plasma elongation, Fig. 4a: for constant injected power, higher elongation is obtained at higher density. This enhancement results firstly from the improvement of confinement with density, which can be seen in the

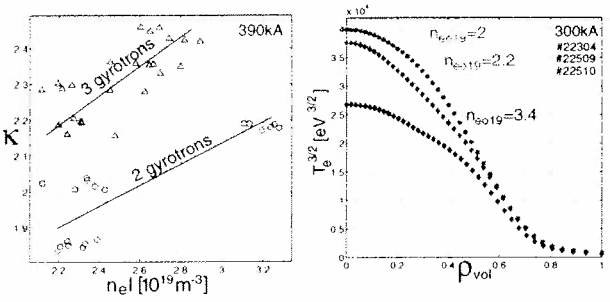

FIG. 4a & 4b High density operation:
a) increase of κ with density at constant EC power,
b) the temperature deduced resistivity profile, an indication of the current profile, is flattened and therefore broadened with density.

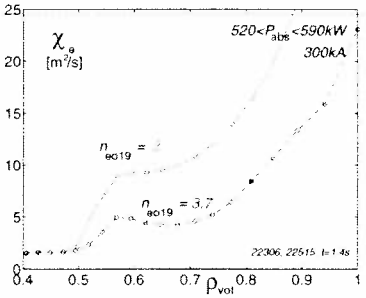

FIG. 5 Current diffusivity χ_e for low (n_{eo}~2 $10^{19}m^{-3}$) and high density (n_{eo}~3.6 $10^{19}m^{-3}$) and at similar absorbed power, respectively P_{abs}~520 and 590kW (ρ_{dep}~0.54).

mal diffusivity profiles obtained from power balance, Fig. 5. At the higher densities, the χ_e profile is comparably reduced outside the deposition location, as expected from the usual improvement of confinement with density. This corresponds to an electron confinement time τ_{Ee} increase from 5 to 6ms. The enhancement results, secondly, from an increase by more than an order of magnitude of the electron to ion power transfer P_{ei} with density, peaked on axis, which tends to flatten the current profile. In the absence of a direct measurement of the current profile, two pieces of evidence seem to confirm this hypothesis. First, the temperature profile (hence the resistivity profile, proportional to $T_e^{3/2}(\rho)$) is flattened, Fig. 4b. The second piece of evidence comes from MHD activity. At low density, with off-axis heating at low current, 300kA, sawteeth are lost during the elongation ramp-up when q_o>1, without noticeable mode activity. At high density, internal mode activity occurs at the q_o~1 crossing, and can persist during the full discharge. Such mode activity is analysed using the MPX [15]. An m=1, 2, 3 mode structure inside the inversion radius, Fig. 6, is found, with a slowly decreasing m-spectrum, where the m=2 and 3 mode amplitude are respectively 70% and 20% of the m=1 amplitude, a typical signature of a flat current profile [20].

A further enhancement of X2 efficiency can be obtained by using ECCD (φ~±10°), thus increasing the suprathermal level.

Optimal conditions for current profile broadening require deposition in a narrow layer 0.55<ρ_{dep}<0.7, high density operation and some toroidal component of the injection angle. The use of far off-axis X2 ECH in high-density discharges, up to 8 $10^{19}m^{-3}$ on axis, twice cut-off density, has allowed us to extend the range of elongated equilibria substantially at intermediate currents, Fig. 7.

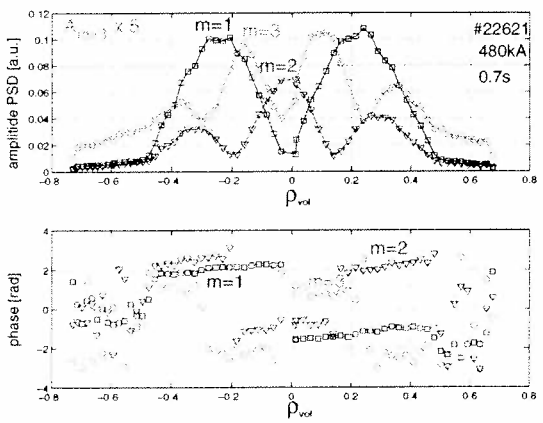

FIG. 6 Mode activity m=1,2,3 inside inversion radius ρ_{inv}=0.4, from the 64 channel soft X-ray multiwire proportional chamber diagnostic.

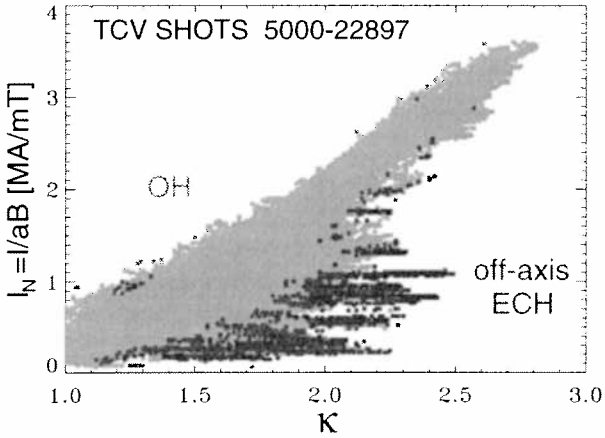

FIG. 7 Range of TCV operation: Ohmic discharges (green) and ECH (red). Off-axis ECH allowed reaching κ=2.48 at low I_N.

4. X3 power deposition in high elongation discharges

High-elongation high-density discharges, overdense to X2 in the core, are developed ultimately for β-limit and confinement studies. They provide the target plasmas for X3 heating and deposition studies. The discharges have high n_eT_e to maximise X3 absorption and high κ to enhance the absorption by the geometrical effect of shallow incidence on the resonance.

In discharge 23366, see Fig. 1 (390kA, φ_{X2}=+10°, n_{eo}~6->7 $10^{19}m^{-3}$, P_{abs_X2}= 1.41MW deposited at ρ_{dep}= 0.7 to 0.5), we apply 0.63MW average X3 power with half of the power modulated at 337Hz. The elongation reached with X2, κ_{max}~2.43, is limited by vertical stability. Later, during the X3 phase, the central deposition peaks the current profile. The resulting increase of l_i and decrease of κ can only be partly compensated by the shaping coils: keeping the elongation constant, while X3 peaks the current profile, leads to an increase of the vertical instability growth rate, limiting the maximal stable elongation.

The optimal poloidal mirror angle θ_{X3} is found by maximising the soft X-ray temperature in a mirror angle sweep. The optimal X3 power modulation frequency (337Hz), yielding reliable results for both the DML and MPX, gives a phase of the response close to 90°.

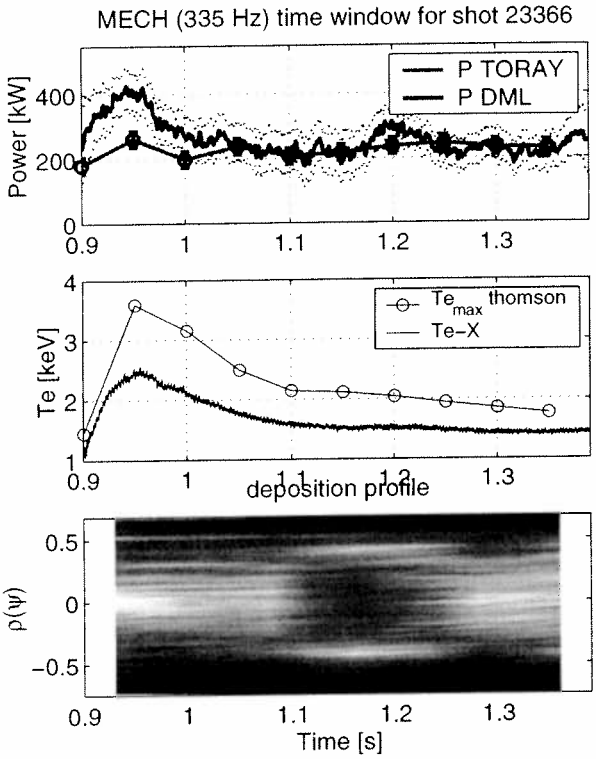

FIG. 8
a) X3 absorbed power from DML and from ray tracing.
b) Electron temperature from Thomson and soft X-ray,
c) Power deposition profile on the MPX, showing different power deposition profile width, from peaked to hollow.

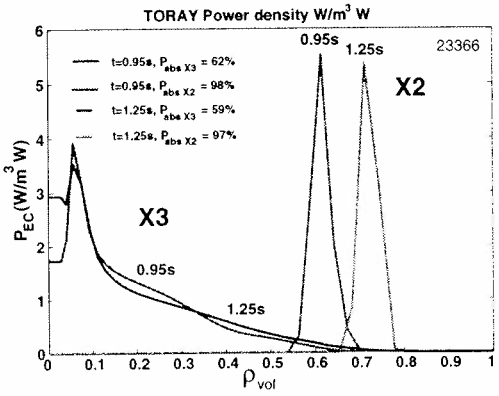

FIG. 9 X2 and X3 beams
a) at start of X3 (n_{eo}= 5.8 $10^{19}m^{-3}$) and
b) at t=1.25s (n_{eo}=6.4 $10^{19}m^{-3}$)

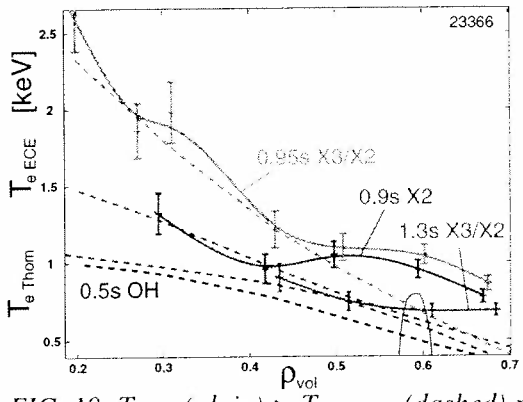

FIG. 10 $T_{e\,ECE}$ (plain) > $T_{e\,Thomson}$ (dashed) profiles indicating suprathermal emission during X2/X3:
1) t=0.5s, ohmic $T_{e\,Thom}$,
1) t=0.9s, X2: $T_{e\,ECE}$ max. just inside ρ_{dep}=0.59, schem. indicated, peaking toward axis, remark $T_{e\,Thom}(\rho)$ broadened by X2,
3) t=0.95s, X3/X2: $T_{e\,ECE}$ ~ $T_{e\,Thom}$ in centre, bigger at ρ_{dep}>0.5; strong X3 bulk heating
t=1.3s, X3/X2: $T_{e\,ECE}$ > $T_{e\,Thom}$ at ρ_{dep}>0.6, centre unknown.

The power deduced from the DML is identical to that from ray tracing for most of the time slices, which implies a fully thermal plasma, Fig 8. For these times the deposition profile, which is similar to the one deduced from ray tracing, is monotonic and peaked on axis, Fig 9. There are exceptions: at the beginning of X3, a remarkably high T_e is reached together with a very peaked MPX deposition profile. Later, at t=1.25s, a second, smaller T_{eX} maximum is observed, this time associated with a very hollow deposition profile, not accounted for by thermal ray tracing calculations. The hollow deposition and $P_{DML}>P_{Toray}$ indicates again suprathermal absorption. The presence of suprathermals is confirmed by $T_{ECE}/T_{Thomson}>1$, already during X2, and extends over most of the X3 heating period. The T_{ECE} profile evolution in Fig. 10 shows that the maximum of suprathermals during X2 peaks just inside the X2 deposition location and toward the centre of the discharge. At the beginning of X3, the profile rises everywhere, correlated with full absorption as measured by the DML. Later, an annular suprathermal emission forms at ρ_ψ=0.65, simultaneous with the annular deposition measured at ρ_ψ~0.4 on the MPX.

These experiments show that the absorption is very sensitive to the mirror angle θ_{X3}. Differences of mirror angle of 0.2° and variations of the plasma parameters modify the absorbed power significantly, which justifies the development of a feedback system to maintain full power absorption throughout the discharge [1]. However, under these conditions and at half of the nominal power, 630kW, a substantial increase of T_e is measured in the discharge of Fig. 1, with β and $T_i(t)$ profiting from the high density operation.

4. Conclusions

With the help of far off-axis X2 power deposition to broaden the current profile and to elongate the plasma, discharges of high elongation, κ~2.5, at I_N,~1.05, centrally overdense to X2, have been created and sustained. Higher values of κ and I_N will be achievable with the full X2 power (4 beams) from the upper lateral ports. In these plasmas, X3 power absorption close to 100% has been reached, with typically 60-70% deposited centrally on the bulk, and 20-30% on suprathermal electrons with a broader or hollow radial distribution in presence of suprathermal electrons.

This work was partially supported by the Swiss National Science Foundation.

References

[1] Porte, L., et al., 19th IAEA FEC Conf. IAEA 2002, Lyon, EXP/P5-15.

[2] Hofmann, F., et al., Phys. Rev. Lett. **81**, (1998) 2918.

[3] Ericsson, G, Bondeson, A, Ward, D.J., Hofmann, F., Villard, L., Proc. 19th EPS 1992, Vol 16C, Part I, 343.

[4] Pochelon, A. et al., Proc. 18th IAEA FEC, Sorrento, Italy, IAEA-CN-77 (EXP3/10), (2000) 155.

[5] Pochelon, A., et al., Nucl. Fusion **41** (2001) 1663.

[6] Hofmann, F., et al., Plasma Physics and Controlled Fusion, **43** (2001) A161.

[7] Hofmann, F., et al., Nucl. Fusion **42**, 743-749 (2002).

[8] Pochelon, A., et al., Proc. 29th EPS Conf, Montreux, June 2002, ECA Vol. 26B (2002) P2.075.

[9] Alberti, S., et al., Nuclear Fusion **42**, 42 - 45 (2002).

[10] Blanchard, P., Plasma Phys. and Contr. Fusion, **44** (2002) 2231.

[11] Alberti, S., et al., Proc. 29th EPS Conf, Montreux, June 2002, ECA Vol. 26B (2002) P2.073.

[12] Arnoux, G., et al. Proc. 29th EPS Conf, Montreux, June 2002, ECA Vol. 26B (2002) P2.076.

[13] Manini, A., Moret, J.-M., Alberti, S., et al. Plasma Physics and Controlled Fusion, **44** (2002) 139.

[14] Manini, A., Moret, J.-M., Ryter, F. et al., subm. for publ. to Nucl. Fus.; Manini, A., Thesis, LRP 724 (02).

[15] Sushkov, A. et al., Proc. 29th EPS Conf, Montreux, June 2002, ECA Vol. 26B (2002) P4.118.

[16] Camenen, Y., et al., Proc. of EC-12, Aix-en-Provence, France, May 2002, 407.

[17] Matsuda, K., IEEE Trans. Plasma Science. **17** (1989) 6.

[18] Angioni, C., et al., Theory of Fus. Plasmas, Varenna 2000, ISSP-19 (Ed. Comp, Bologna, 2001) 73.

[19] Boucher, D., et al., IAEA TCM Adv. in Simul. & Model. Thermonucl. Plasmas, Montreal (1993) 142.

[20] Duperrex, P-A., et al., Nucl. Fusion **32** (1992) 1161.

Third Harmonic X-mode Electron Cyclotron Resonance Heating on TCV using Top Launch

L. Porte, S. Alberti, G. Arnoux, Y. Martin, J.P. Hogge, T.P. Goodman, M.A. Henderson, E. Nelson-Melby, A. Pochelon, M.Q. Tran

Centre de Recherches en Physique des Plasmas, Ecole Polytechnique Fédérale de Lausanne, Association EURATOM-Confédération Suisse, CH-1015, Switzerland

Email contact of main author : laurie.porte@epfl.ch

Abstract. A third harmonic electron cyclotron resonance heating system (X3) has been installed, commissioned and brought into service on the Tokamak à Configuration Variable (TCV). It comprises three 118Hz, 0.5MW gyrotrons designed to produce pulses up to 2 seconds long. In the present configuration, 1.0MW is launched vertically from the top of the vessel into the plasma and the remaining 0.5MW is launched horizontally from the low field side. X3 has been used to heat plasmas at density exceeding the 2nd harmonic cut-off significantly extending the operational space of additionally heated TCV plasmas. Studies have been performed to determine the optimal plasma/launcher configuration for X3 absorption for various plasma conditions and to find methods for real time feedback control of the X3 launcher. First experiments have been performed aimed at heating H-mode plasmas on TCV. First results show that the ELMs in TCV ohmic H-mode plasmas exhibit all characteristics of Type III ELMs. If, at moderate X3 power (<0.3MW), the additional heating is increased and then decreased, the ELM frequency first decreases and then increases again. At higher X3 power (>0.45MW) the Type III ELMs disappear and the H-mode discharge exhibits different MHD phenomena eventually disrupting.

1. Introduction

TCV has had a powerful and versatile 2nd harmonic electron cyclotron heating system (X2) for a number of years [1]. This system has been used to study many aspects of tokamak physics. These studies have been performed at density not exceeding the second harmonic cut-off ($n_e = 4.25 \times 10^{19} m^{-3}$) and in practice the plasma density has been kept $<3.0 \times 10^{19} m^{-3}$ to minimise refraction effects. The 3rd harmonic electron cyclotron heating system (X3) significantly extends TCV operations by allowing access to density up to $\approx 10^{20}$ m^{-3}.

The linear ray tracing code TORAY-GA has proven useful as a tool in designing X3 experiments even at the high density associated with H-mode operation. In particular it is capable of predicting the optimal X3 mirror launch angle for a given plasma configuration. It has become obvious that active feedback control of the X3 launcher mirror is required to maintain X3 absorption. Experiments have been performed to determine which diagnostics are most useful for feedback control and to test methods of real-time signal analysis.

A routinely accessible 'gateway' to the ohmic, quasi-stationary ELMy H-mode regime has been found on TCV [2]. Using this 'gateway' a series of experiments has been performed to determine the best plasma/launcher geometry for heating an ELMy H-mode on TCV and to examine the effects of the heating on ELM behaviour.

In section 2, of this paper, the X3 heating system is briefly described. In section 3, the results of experiments designed to examine the feasibility of real-time feedback control of the launcher mirror are described. In section 4 the preliminary H-mode heating experiments are described. Section 5 presents a summary and conclusions.

2. The X3 heating System

A detailed description of the gyrotrons has been given by Alberti et al in [3]. The entire system is described by J.P. Hogge et al [4]. Three gyrotrons operating at 118 GHz and rated for 500 kW, 2-second-operation have been installed on TCV. A matching optical unit (MOU) is used to manually set the polarisation of the gyrotron output beam with arbitrary, controllable ellipticity. The elliptically polarised beam, from each gyrotron, is transmitted to the tokamak or a calibrated load along ≈40m of evacuated corrugated waveguide. Each gyrotron has its own transmission line. The three separate waveguides of the top launch system converge in the direction of the single launcher mirror that has a focal length of 700mm and is made of copper; Fig 1b. The mirror can be translated, on a shot to shot basis along a major radius between 800mm and 965mm (the vacuum vessel axis is at 880mm) and can be rotated poloidally, during a shot, between 40° and 50°. Figure 1 shows the experimental layout with the beam trajectory following the cyclotron resonance and antenna system.

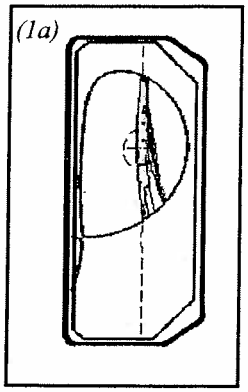

Figure 1: X3 radiation is projected into TCV from the top and traverses the cyclotron resonance; dashed red line in (1a). Radiation is delivered to the top launcher along three separate evacuated waveguides that converge to a point behind the single mirror (see 1b) of the top launcher.

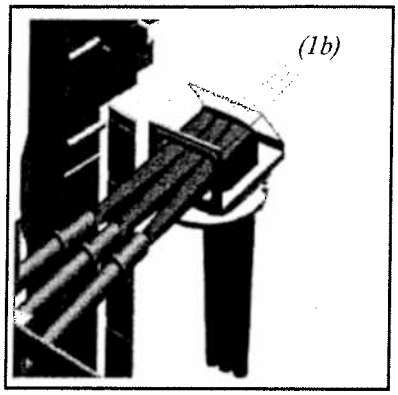

3. Launcher Optimisation and Feedback Control

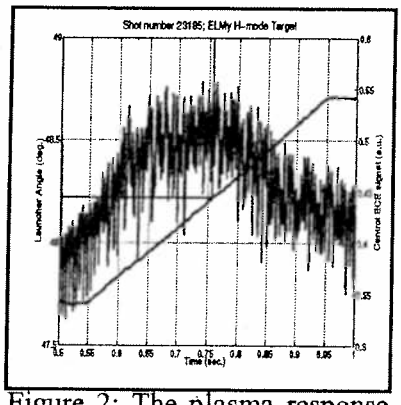

Figure 2: The plasma response measured using a central ECE channel is plotted with the X3 launcher angle.

With a long narrow resonance layer (see Figure 1a) it is important that one can, a priori, predict the optimal launcher angle for X3 and control the mirror launch angle in real time to adapt to changes in the plasma profiles. TORAY-GA has been used to predict the optimal launch angle and experiments have been performed to study the best means of real time mirror control.

Sweeping the X3 poloidal launch angle while heating stationary plasma allows one to determine the optimal launcher angle. By comparing the experimentally deduced optimal launcher angle with the TORAY-GA predicted angle one can benchmark the code for the plasma parameter range of interest. This has been done for steady-state H-mode plasma. Figure 2 shows the plasma response measured using a central ECE channel that has a line of sight through the plasma centre. The peak in the ECE signal is interpreted as representing the moment of maximum power absorption and the launcher angle at this time is assumed to be the optimal angle. Here the maximum response is at a launcher angle of ≈48.2°; TORAY-GA predicted an optimal angle of 48° for this discharge. TORAY-GA may be used as a tool in designing H-mode experiments with X3 top launch heating.

During the heating phase, plasma profiles change and the position of the maximum electron cyclotron absorption may move. If the launch mirror does not move to accommodate this, the absorbed power may decrease: real time launcher mirror control is required. Experiments were performed to test means of real time data analysis and to determine the best signals for use in real time control. The launcher mirror was swept linearly through the cyclotron resonance but superimposed on the linear sweep were sinusoidal oscillations. The oscillations perturbed the absorption and allowed one to determine the maximum response by examining the phase and amplitude of the perturbations. Figure 3a, top, shows the mirror sweep while 3a, bottom, shows the plasma response measured by a soft X-ray camera with a line of sight through the plasma centre. Figure 3b displays the measured plasma response (top), with filtered perturbation and filtered response signals. Shown, also, is the deduced phase of the response. At the peak of the measured response, the phase of the response attains a value of $\pi/2$ radians and exhibits a π radians phase change as the peak is traversed. Locking the phase response would allow real time control of the mirror. The centrally viewing SXR camera signal can be used as a source for real time control. Algorithms that can be implemented, in real time, on a digital signal processing (DSP) card are being developed.

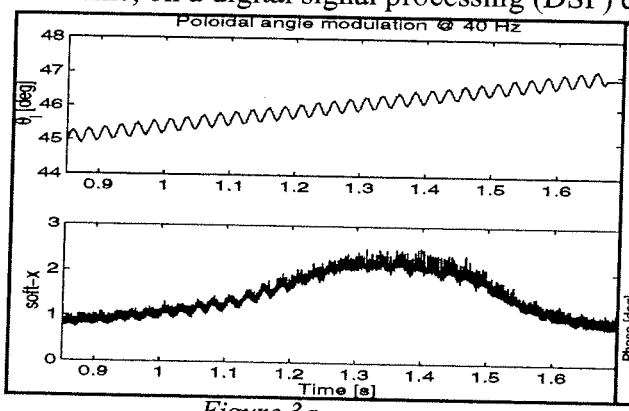

Figure 3a

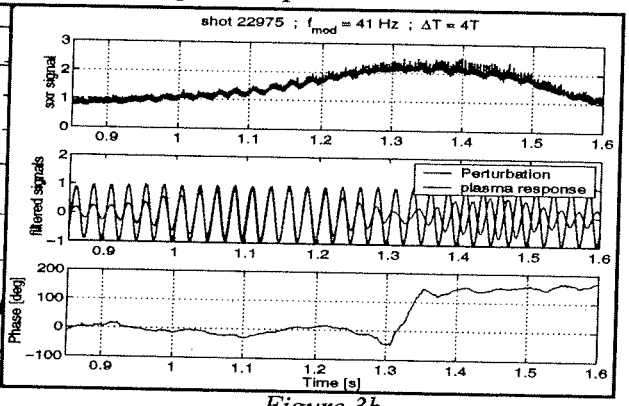

Figure 3b

Figure 3: Fig 3a (top) shows the mirror sweep with the sinusoidal perturbation and 3a (bottom) shows the plasma response measured using a centrally viewing SXR camera. By post processing the SXR signal it is possible to extract the amplitude and phase of the plasma response w.r.t. the imposed perturbation. The phase response is shown in Fig 3b along with the SXR signal and the digitally filtered signals. The deduced phase signal shows where the maximum plasma response is located. By phase locking the response it will be possible to control in real time the launcher mirror.

4. X3 heating of H-mode discharges

Until X3 heating was installed on TCV the only quasi-stationary H-modes that were routinely available were ohmic H-modes that were approached through a narrow gateway in parameter space [2]. Experiments using X2 to heat the plasma, in H-mode, have been performed but these have only been used to heat the extreme plasma edge ($\rho > 0.9$) and have, for machine safety reasons, been limited to ECH pulse lengths no longer than 20ms. Using X3 to heat the core of ELMy H-modes, accessed through the gateway, experiments have been performed to establish quasi-stationary additionally heated ELMy H-modes and to study the effect of heating on the ELMs. Quasi-stationary ELMy and non-stationary ELM free H-modes have been established on TCV at densities far exceeding the X2 cut-off using X3 pulse lengths of several hundred milli-seconds. In all of these discharges the ohmic heating power was ≈500kW. In these experiments it was impossible to measure the coupled X3 power because the ELMs perturbed the diamagnetic measurement too much. Work is continuing to develop means of measuring the absorbed power in the presence of ELMs. Estimates of coupled power, stated in this paper, are from TORAY-GA calculations. Pochelon et al [5] describe experiments where they measure almost full absorption (>90%) of X3 using top launch.

Initial attempts to heat the ELMy H-mode on TCV often led to an ELM free period that transited back to L-mode finally disrupting after the formation of a locked mode: see Figure 4a. These discharges were non-stationary and the disruption limited the heating period to less than ≈200ms. This behaviour prevailed even at low additional heating power; <200kW. By reducing the gas feed ≈100ms before the start of X3 it has been possible to maintain the quasi-stationary H-mode in the presence of X3. The reduced gas feed increased the ELM frequency. The increased ELM frequency balanced the tendency of the heating power to decrease the ELM frequency and permitted the ELMy H-mode to be maintained. The MHD phenomena, that caused the locked mode and disruption, were avoided or at least delayed. Access to longer (> 700ms) additionally heated H-mode discharges was obtained. Figure 4b shows such a discharge.

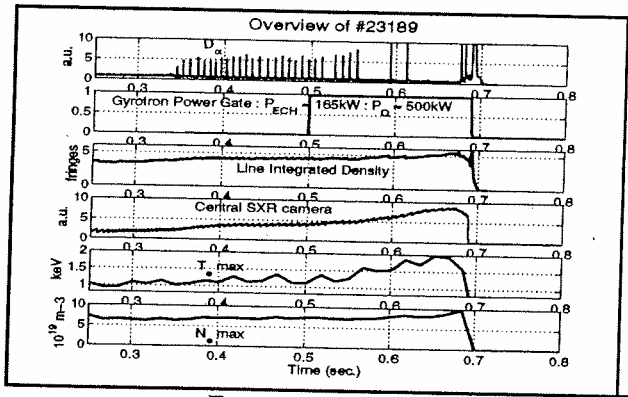

Figure 4a.

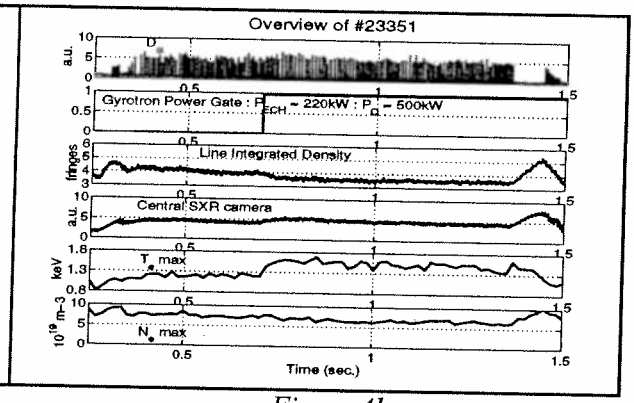

Figure 4b

Figure 4: Fig. 4a shows the evolution of a X3 heated ELMy H-mode that exhibits the typical transition to ELM free H-mode (at ≈0.62sec.), MHD phenomenon (at 0.675sec.) followed immediately by a transition to L-mode and eventually ending in a disruption. Fig. 4b exhibits the modified, more stable behaviour of a X3 heated ELMy H-mode with a modified gas feed. At ≈1.3 times higher additional heating power, the discharge remains ELMy.

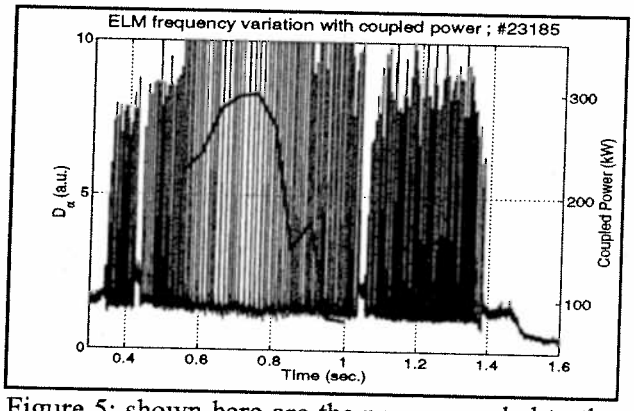

Figure 5: shown here are the power coupled to the plasma (from TORAY-GA) and the D_α signal. In this experiment the launch mirror was swept across the cyclotron resonance resulting heating power that first increased, to ≈300kW, then decreassed. In response to the heating power the ELM frequency first increased and then decreased.

To examine the behaviour of the ELMs typical of a TCV ohmic, ELMy H-mode the X3 launcher mirror was scanned across the cyclotron resonance. With an X3 injected power of ≈420kW, the coupled power first increased from ≈220kW to ≈300kW then decreased to <100kW while the ohmic heating power remained approximately constant. The discharge stayed in the ELMy regime similar to that of the ohmic H-mode but the ELM frequency first increased then decreased with the ECH power. The relative energy loss per ELM was measured to be ≈6%. ELMs in TCV ohmic H-mode exhibit the characteristics of the so-called Type III ELMs [6]. Chord averaged measurements from a soft X-ray camera reveal that, typically, these ELMs effect only the plasma edge ($\rho > 0.6$).

Experiments where $P_{ECH} \approx P_\Omega$, have been performed to explore the H-mode in a regime where the ohmic H-mode ELMs disappear. Figure 6 shows the overview of a typical discharge. The coupled power remained approximately constant at ≈520 kW (840kW launched power). The

'ohmic H-mode ELMs' disappeared after ≈50 msec. of heating. They were replaced by an event that caused a rapid loss of particles and energy and that affected the whole minor radius. Figure 6b shows the effect on the plasma of this instability as measured using a high-resolution soft X-ray camera. There is rapid (<150 μsec.) loss of particles and energy at normalised radii $\rho > 0.55$. At radii $\rho < 0.55$ the loss of energy and particles starts at the same time but the decay is somewhat longer (> 300 μsec.). Typically, the high power discharges end in a disruption after the formation of a locked mode.

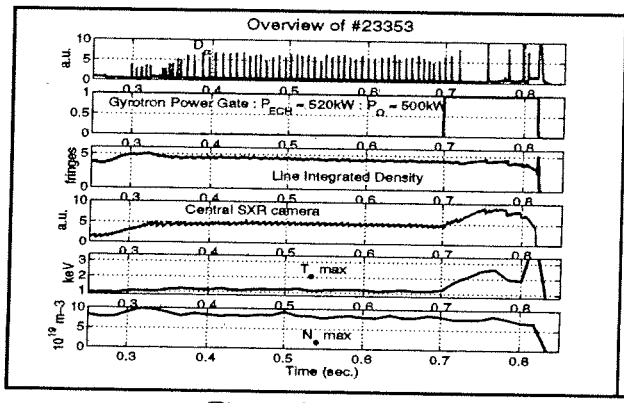

Figure 6a

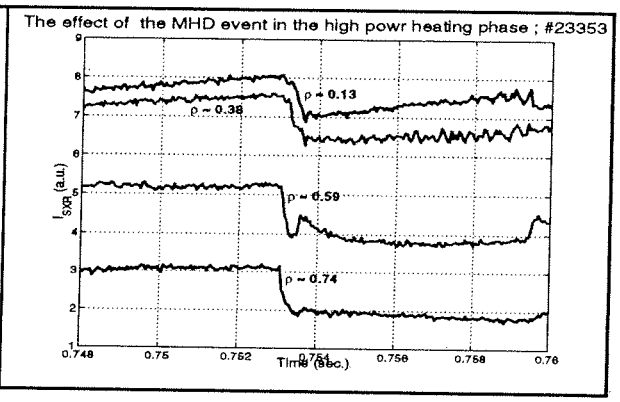

Figure 6b

Figure 6: 6a shows the overview of an ELMy H-mode subject to high additional heating power. The ohmic ELMs disappear after ≈50msec to be replaced by an instability that affects the whole minor radius. The new instability has no measured precursor and measurements show the loss of energy starts at the same time in the centre as in the edge. The heat loss from the edge happens more quickly than from the centre; see Fig 6b.

5. Summary and Conclusions

A 3rd harmonic ECRH system (X3) has been installed and commissioned on TCV. TORAY-GA has been found adequate for use in designing X3 in H-mode experiments. Real time launcher position control is required and experiments have been performed to explore data analysis techniques suitable for real time control and to decide which diagnostics are most useful. Soft X-ray cameras are promising candidates. Experiments have been performed to use X3 to heat H-mode in TCV. By varying the coupled X3 power in an ELMy H-mode plasma it has been observed that ELMs, of the sort observed in a TCV ohmic H-mode, exhibit the characteristics of Type III ELMs. Increasing the X3 power resulted in the H-mode going into an ELM-free phase and exhibiting MHD instability that affected the whole minor radius.

This work was partially sponsored by the Swiss National Science Foundation.

Appendix 1: References

[1] M.A. Henderson et al; Proc. 4th Int. Workshop on Strong Microwaves in Plasmas, Nizhny Novgorod, 1999.
[2] Y. Martin et al; 'ELMing H-mode Accessibility in Shaped TCV Plasmas'; Proceedings of the 18th IAEA Conference on Fusion Energy, Sorrento, Italy, October 14 – 19 ; 2000.
[3] S. Alberti et al; 'European High Power CW Gyrotron Development for ECRH Systems'; Fusion Engineering and Design **53** (2001) 387 – 397.
[4] J.P. Hogge et al; Proc. EC-12 Workshop; Aix-en-Provence, May 2002.
[5] A. Pochelon et al; Paper EX/P5-14 this conference
[6] H. Zohm; 'Edge Localised Modes (ELMs)'; Plasma Physics and Controlled Fusion, **30** (1996); 105 – 128.

Steady-state fully non-inductive reverse shear scenarios with electron ITB and dominant bootstrap current

O.Sauter, R. Behn, P. Bosshard, S. Coda, I. Condrea, T.P. Goodman, M.A. Henderson, P.Nikkola

Centre de Recherches en Physique des Plasmas, Association EURATOM-Confédération Suisse, CH-1015 Lausanne, EPFL, Switzerland.
e-mail contact of main author ; olivier.sauter@epfl.ch

Abstract. The relation between the safety factor profile, q, the electron transport and the bootstrap current is of crucial importance for predicting advanced scenarios in burning plasmas which will have dominant electron heating and small momentum input. In recent experiments in the Tokamak TCV, the full plasma current has been sustained with only off-axis co-current drive and bootstrap current. As soon as the EC power is turned on, the inductive current is set to zero. Therefore the current profile evolves from the original ohmic profile to the one driven by the off-axis beams without any externally applied loop voltage. Due to the resulting reverse shear profile an electron internal transport barrier (eITB) is formed and the bootstrap current increases up to 50% of the total plasma current. Adding heating or counter CD in the center exhibits clear difference in the time evolution of the electron temperature profile. With less current driven in the center, and therefore a more reversed q profile, the eITB is more pronounced and better global electron energy confinement time is obtained. Increasing plasma density and EC power, electron internal transport barrier discharges with up to 80% bootstrap current have been sustained in steady-state with no ohmic current.

1. Introduction

In the last few years studies of advanced scenarios have been mainly focused on internal transport barriers (ITB) observed in the ion temperature profile and on the effects of momentum input and q profile on the barrier formation. In addition these ITBs have been obtained using fast current ramps. Electron ITBs have also been reported in several tokamaks, JET, RTP, FTU, AUG, DIII-D, JT60-U, and T10 [1], however they are usually weaker or more difficult to sustain and most of them rely on early heating in current ramp-up scenarios.

In the tokamak TCV we have been able to create electron ITBs without fast current ramp and without momentum input, solely with the help of electron cyclotron (EC) wave particle interactions. The EC beams are aimed at specific location in either heating (ECH), co- or cntr-current drive (CD), such as to create and sustain the pressure and current profiles required to obtain significant electron confinement improvement.

The experimental set-up and the typical properties of these new steady-state reverse shear eITB scenarios are described in Sec. 2. It is also shown that it is the bootstrap (BS) current which sustains the hollow current profile. The relation between these experiments and the improved core electron confinement (ICEC) discharges obtained with central cntr-CD beams and ECH off-axis pre-heating are discussed in Sec. 3. In Sec. 4 we show that even in BS dominated discharges the barrier location does not evolve, although the bootstrap current determines the q profile and the position of q_{min}.

2. Experimental set-up of fully sustained reverse shear scenarios

The tokamak TCV is equipped with a very flexible EC system which allowed stable fully sustained non-inductive discharges thanks to the ability to position the beams where desired [2]. This flexibility was also instrumental in obtaining the so-called ICEC regime with off-axis pre-heating and on-axis cntr-CD [3]. The latter regime is characterised by very peaked electron temperature, up to 14keV, and flat or slightly reversed q profile. The temperature rise in the center re-inforces the ohmic current density due to the increased conductivity. This effect has to be compensated by counter-ECCD. Thus the total current density in the center is

the result of two large counter-acting components, which makes it difficult to widen the region of reversed q profile and improved confinement. Therefore a new scenario has been developed where off-axis co-CD beams sustain the full plasma current [4]. It removes the ohmic contribution and the aim was also to drive off-axis ECCD to obtain advanced scenarios. However due to the size and plasma parameters of TCV and the relatively large EC power density, radial diffusion of the fast electrons has to be considered when calculating the driven ECCD [5]. Using the CQL3D Fokker-Planck code to simulate these scenarios, it was found that the actual ECCD profile is nearly flat or slightly hollow, even though the power deposition is clearly off-axis [6]. The value of the diffusion coefficient assumed in the simulations in order to obtain the correct total driven current I_{CD} is consistent with standard L-mode confinement scaling and with the results of specific experiments using a pinhole hard X-ray camera [7]. The radial and velocity dependence of this diffusion coefficient is still under investigation [8].

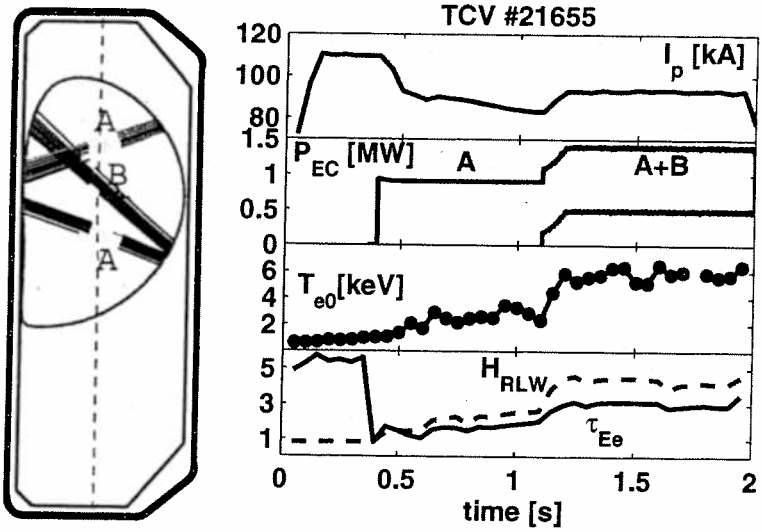

Fig. 1 (left) : Two beams off-axis in co-CD (A), then one beam on-axis in cntr-CD (B). The ohmic transformer is set constant from 0.42s. Note that τ_{Ee} increases albeit a 50% increase in input power, yielding factors $H_{RLW} \geq 4$, and $H_{IT98L} \sim 1.6$.

In Fig. 1 we show the typical experimental set-up of these fully sustained reverse shear scenarios. First a stationary ohmic plasma is created at low plasma current. At 0.4s two or more off-axis co-CD beams are turned on (A). The externally applied ohmic current is set to zero by imposing a constant current in the ohmic transformer as in the full ECCD scenarios [2b]. After the current profile has evolved, the second EC cluster is turned on mainly to provide central power deposition in order to probe the presence of an eITB. As seen in Fig. 1, adding 0.45MW in the center, in this case with a small cntr-CD component, leads to an increase of the electron energy confinement time, τ_{Ee}, confirming the very good confinement in the center. In general we compare τ_{Ee} with the RLW scaling law [9] as it correctly predicts τ_{Ee} during ohmic heating, whereas the ITER98-L mode scaling [10] predicts twice the experimental value in ohmic and is not really appropriate when the ions are cold.

In Fig. 2 we show the current density profiles in the high performance phase shown in Fig. 1, 1.2s-1.8s, as calculated with CQL3D using $I_{CD}=I_p-I_{BS}$ as a constraint to determine the diffusion coefficient [5]. We also show the BS current density, calculated from the experimental profiles and using the formulae in Ref. [11]. The resulting q profile is then obtained using the total current density and pressure profiles as source terms of a fixed boundary equilibrium code, Fig. 2(b). It is interesting to note that the q profile obtained from the magnetic reconstruction, LIUQE, is very similar over most of the minor radius [4b].

As mentioned earlier these scenarios are obtained with no momentum input. In addition as it is argued that the q profile modification is sufficient to create the eITB, we expect the rotation profile to be insignificant with respect to the barrier formation. This is confirmed by the rotation profile measured by the CXRS diagnostic [12] in a scenario similar to the one presented in Fig. 1, but positioned at z=0 to allow better radial coverage. It shows that the rotation actually decreases with respect to the ohmic profile when the EC is turned on. It is essentially flat in the high performance phase as well, similar to T-10 observations [1c]. The ion temperature profile is also shown in the three different phases. During the latest phase, T_{e0}~6keV and T_e/T_i~30 even though it is often assumed that large T_e/T_i ratios prevent eITB formation.

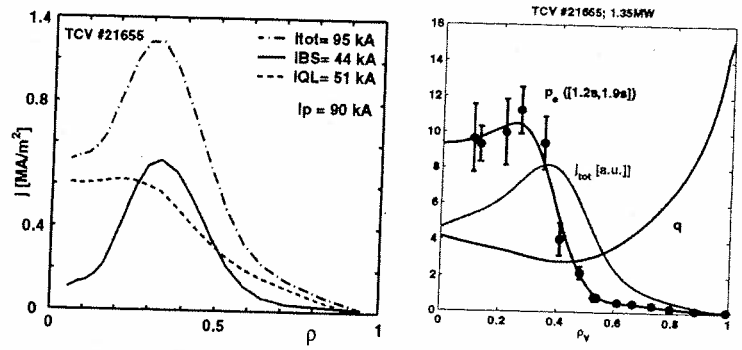

Fig. 2 (bottom): (a) EC, BS and total current density in the [1.2s,1.8s] phase of the discharge shown in Fig. 1. (b) Resulting q profile, with j_{tot} and p_e profiles.

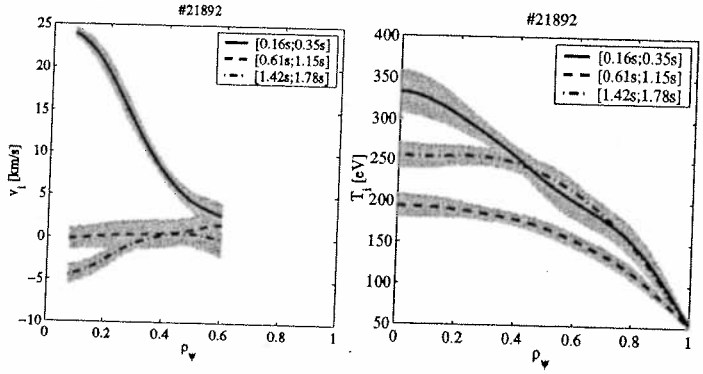

Figure 3: Ion toroidal rotation and ion temperature profiles for a case similar to the #21655 shown in Fig. 1. Profiles in ohmic, off-axis beams and cntr-CD on-axis phases are shown respectively

3. Electron ITB with and without a large ohmic current density

In previous experiments at larger plasma current, ICEC was obtained using off-axis and on-axis beams as mentioned earlier [3]. In this way stationary scenarios with confinement factors above 3 have been obtained. In Fig. 3, the profiles of a fully sustained reverse shear scenario, with P_{EC}=2.2MW, similar to the one in Figs. 1 and 2 with 70-80% BS current are compared with profiles obtained in an ICEC regime as described in Ref. [3] with 2.2MW. Both cases exhibit large localised gradients, however the former has a much broader eITB, which also explains the much larger BS current density. Note that the relative confinement is larger in #22895 due to the broader region of improved transport, however τ_{Ee} (~5ms) is greater for the ICEC case, #19425, due to the larger plasma current (200kA) and density.

In Ref. [3] it was conjectured, based on successful transport simulation and prediction using PRETOR, that the improved confinement was due to reverse shear in the center with a q_{min} value near 1. However the total current density in these cases is difficult to determine as it is the result of the difference of two large contributions: the central ohmic current density, very peaked due to the peaked Te profile (Fig. 3b, #19425), and the central counter ECCD. In the fully sustained reverse shear scenarios, the improved confinement is clearly due to the q profile and occurs in the region of flat and negative shear (Fig. 2). It confirms the effects described in Ref. [3] and explains why the eITB is much narrower since q_{min} is around ρ~0.2

in these cases. However it provides a nice comparison of profiles with different q_{min} position and absolute value.

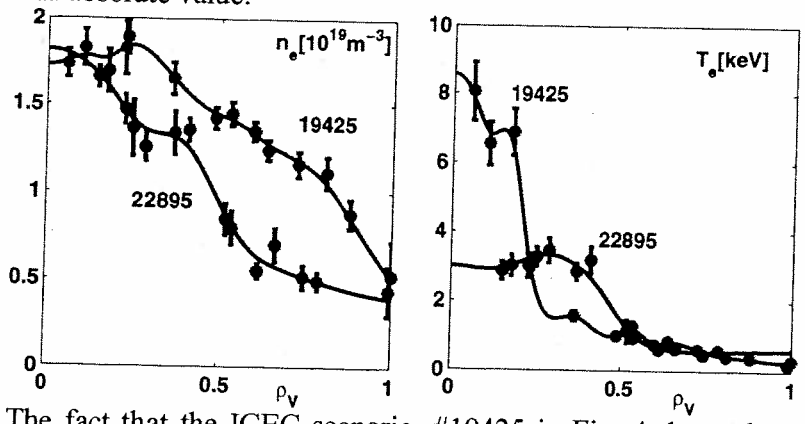

Figure 4: Density and temperature profiles for an ICEC scenario, #19425, and an off-axis co-CD fully sustained reverse shear scenarios, #22895.

The fact that the ICEC scenario, #19425 in Fig. 4, has a large ohmic current contribution, whereas #22895 is fully non-inductive does not seem to influence the effect on electron transport. However, as mentioned above, a too large residual loop voltage will drive a large current peaked in the center in such scenarios due to the large central electron temperature induced by the improved confinement. This will in turn make it difficult to maintain a reverse shear profile and may lead to a "power threshold" to overcome this effect. On the other hand active feedback on the plasma current with small loop voltage allows better control of the discharge.

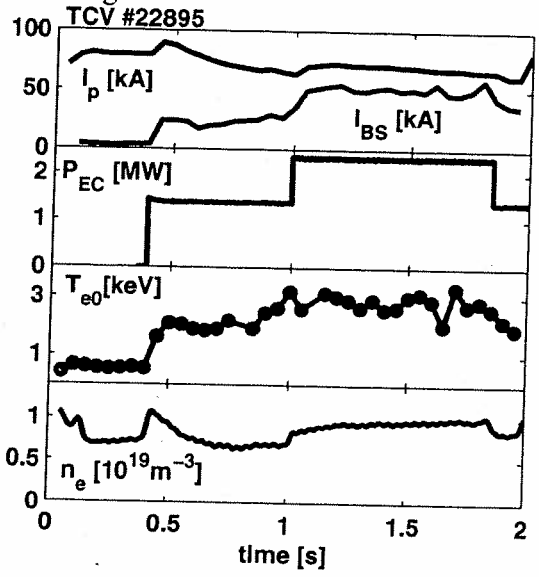

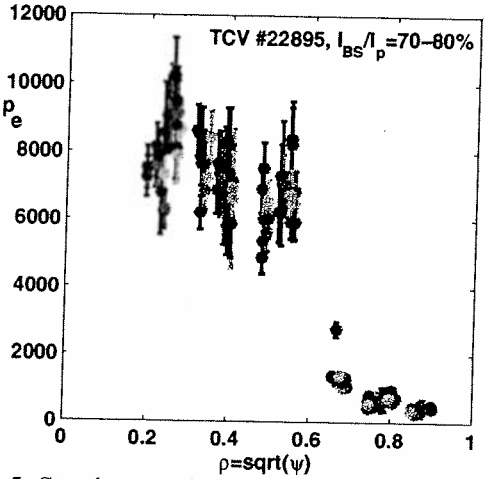

Fig. 5: Steady-state fully sustained eITB scenario with ~70-80% BS current. The ITB position does not evolve for 1.2-1.8s, as seen from p_e profiles.

4. Steady-state eITB with dominant bootstrap current

The reverse shear scenarios described in Sec. 2 are perfect candidates to test the question of bootstrap current alignment in steady-state. As the good confinement region is determined by the q profile, and the non-monotonic current profile is due to the bootstrap current, it is not clear a priori if the self-consistent profiles can be kept in steady-state. For example if the maximum pressure gradient and therefore the maximum current density is well inside q_{min}, this will lead to a new q_{min} position further inside, inhibiting the possibility of reaching a steady-state in bootstrap current dominated discharges. Therefore we have increased the plasma density and EC power in order to increase the bootstrap current fraction. Fig. 5 shows the time trace of the plasma current and bootstrap current, as well as central T_e and line-average electron density. In the first EC phase we have added a central ECH beam, as compared to the case shown in Fig. 1. Then two beams are added, one off-axis ECH and one

on-axis cntr-CD, for a total power of 2.2MW. The eITB is well established as H_{RLW}~4 during the duration of the full power input, 0.6s. This is about 300 confinement times and 4 current redistribution times. The plasma current is not steady because the density is not well controlled and the ECCD is decreasing. However the bootstrap current stays nearly constant and contributes on average to 70-80% of the total plasma current. Therefore the non-monotonic current density profile is clearly sustained by the bootstrap current density. In Fig.5b we show all the density and temperature measurements between 1.2s and 1.8s. First, the barrier is very steep as it occurs essentially in between two data points (3cm apart as projected on the major radius). Therefore $R/L_{Te} \geq 30$, which is at least 3 times larger than the usual value in stiff L-mode scenarios. Second the barrier does not move at all, within the accuracy of our diagnostic, as the two groups of points at top and bottom of the barrier are well separated. We note also that there is a small barrier in the density profile (Fig. 4a), exactly at the same position as for T_e leading to a clear eITB in p_e.

4. Conclusions

New scenarios have been demonstrated for the first time where the plasma current is fully non-inductively sustained with only *off-axis* EC beams. Fokker-Planck calculations indicate that the EC-driven current is nevertheless broad and maximum near the plasma center, despite an off-axis power deposition, due to radial diffusion of fast particles. However the resulting flat or slightly reversed q profile is sufficient to create an electron ITB, which further increases the bootstrap current and therefore strengthens the barrier. In this way wide eITBs have been obtained in steady-state with H_{RLW}~4 (H_{ITS98L}~1.6), with up to 80% bootstrap fraction and β_{pol}~2.

It has also been shown that even with up to 80% bootstrap current, which sustains the non-monotonic q profile and therefore the q_{min} position, the barrier location (which determines the bootstrap current position) does not move and steady-state current and pressure profiles are obtained. Note that these scenarios are obtained without momentum input nor fast current ramps. These results are important for steady-state advanced scenarios in ITER-like plasmas where the main heating source will be electron heating with low momentum input and where large bootstrap fraction are required.

This work is supported in part by the Swiss National Science Foundation.

References

[1] HOGEWEIJ G.M.D. et al, Plasma Phys. Contr. Fus. **44** (2002) 1155 and refs. therein; IDE S. et al, ibidem p. A137; RAZUMOVA K.A. et al, ibidem **42** (2000) 973.
[2] SAUTER O. et al, Phys. Rev. Lett. **84** (2000) 3322; CODA S. et al, Plasma Phys. Contr. Fus. **42** (2000) B311.
[3] PIETRZYK Z. A. et al, Phys. Rev. Lett. 86 (2001) 1530.
[4] SAUTER O. et al, Proc. 29th EPS Conf. on Controlled Fusion and Plasma Physics (Montreux 2002), Europhys. Conf. Abstr. **26B** (2002) P2-087.; GOODMAN T. P. et al, ibidem, P2-081.
[5] HARVEY R. W. et al, Phys. Rev. Lett. **88** (2002) 205001.
[6] NIKKOLA P. et al, Proc. IAEA Technical Committee Meeting on ECRH Physics and Technology for Fusion Devices and EC-12, Aix-en-Provence, France, 2002, p.257.
[7] CODA S. et al, to be published in Plasma Phys. Contr. Fus. **44** (2002) B.
[8] NIKKOLA P. et al, to be published in Theory of Fusion Plasmas, edited by J.W. Connor, O. Sauter and E. Sindoni, ISPP-20 (Bologna, Editrice Compositori) (2002).
[10] ITER PHYSICS BASIS, chapter 2, Nucl. Fusion **39** (1999) 2175.
[11] SAUTER O. et al, Plasma Phys. 6 (1999) 2834; Errata in Phys. Plasmas (2002).
[12] BOSSHARD P. et al, Proc. 27th EPS Conf. on Controlled Fusion and Plasma Physics (Madeira 2001), Europhys. Conf. Abstr. **25A** (2001) 365, P1-094.

Experimental Study of the Stability of Alfvén Eigenmodes on JET

D.Testa[1,2], A.Fasoli[2,1], G.Fu[4], A.Jaun[3], D.Borba[5], P.de Vries[6], and JET-EFDA contributors*
[1] Plasma Science and Fusion Center, Massachusetts Institute of Technology, Boston, USA
[2] CRPP, Association EURATOM – Confédération Suisse, EPFL, Lausanne, Switzerland
[3] NADA VR – Euratom Association, Royal Institute of Technology, Stockholm, Sweden
[4] Princeton Plasma Physics Laboratory, Princeton, New Jersey, USA
[5] Associacão EURATOM/IST, Portugal; EDFA – CSU, Culham Science Centre, UK
[6] Association EURATOM FOM – Rijnhuizen, TEC, 3430 BE Nieuwegein, NL
E-mail contact of main author: dtesta@jet.uk

Abstract. Over the last few years, experiments have been performed on JET to study the dependence of the AE stability limits on the main plasma parameters in different operating scenarios. The measurements are compared with theoretical models with the aim of improving the prediction capabilities for burning plasma experiments, such as ITER. An increase in the edge magnetic shear provides a significant stabilising contribution for AEs in plasmas characterised by a monotonic q-profile. Conversely, with non-monotonic q-profiles and Internal Transport Barriers, multiple weakly damped modes exist in the Alfvén frequency range even in the presence of a high edge magnetic shear, with possible negative implications for the AE stability in ITER. The dependence of the frequency and damping rate of n=1 TAEs on the bulk plasma β was also analysed using NBI heating in limiter plasmas. The mode frequency decreases for increasing β, in agreement with fluid and gyrokinetic predictions. Conversely, contrary to fluid predictions for intermediate and high-n TAEs, for low NBI powers we observe a splitting in the n=1 TAE frequency spectrum, accompanied with a reduction of the mode damping rate. The dependence of the damping rate for n=1 TAEs on the Larmor radius ρ_i has been investigated for plasmas characterised by a low magnetic shear in the core. In these plasmas the coupling between AEs and kinetic Alfvén waves is predicted to contribute significantly to the total damping rate for n=1 TAEs. This mechanism is accounted for by the *radiative damping model* in the NOVA-K code, and is a strong function of ρ_i. Whereas NOVA-K reproduces accurately the measured mode frequency, it is found that the calculated damping rate is too small to account for the measured value under these experimental conditions.

1. Introduction

One of the main issues on the way to a magnetic fusion reactor is the stability of plasma collective modes. Fast particle driven modes, such as Alfvén Eigenmodes (AEs), may cause losses of fast ions, such as fusion born alpha particles in DT plasmas, significantly degrading the plasma performance. The JET tokamak combines the capability of producing reactor-relevant plasmas characterised by significant populations of fast particles with a unique active mode excitation technique [1]. Information on the AE stability limits and its dependence on background plasma parameters can be inferred in different plasma operating scenarios. This paper presents recent data obtained with the AE active diagnostic system on JET. The measurements are compared with various theoretical models, with the aim of improving the prediction capabilities for future burning plasma experiments such as ITER.

2. The Effect of the Plasma Shape on the TAE Stability in the Conventional and Advanced Tokamak Scenario

The dependence of the AE damping rate on the edge plasma shape has been systematically investigated in the limiter phase of a number of discharges with a monotonic q-profile. In agreement with the predictions of the gyrokinetic code PENN [2,3], it was found that the increase in the edge magnetic shear, elongation and triangularity contributes to increasing the damping rate γ/ω for global, antenna-driven, stable n=1 TAEs [4].

---

* See annex 1 of J.Pamela et al., "*Overview of Recent JET Results*", OV-1/1.4, Fusion energy 2002 (Proc. 19th International Conference, Lyon, 2002) IAEA, to be published.

Figures 1 and 2 show the results of recent experiments aimed at measuring the AE excitation threshold, using the drive provided by resonant NBI ions with $v_{||NBI} \approx v_A$, for $n=3 \div 10$ TAEs, as a function of the edge magnetic shear. These modes are expected to be more easily destabilised by the fast particles in ITER than $n=1 \div 2$ TAEs. We compare plasmas with low and high edge magnetic shear, in limiter and X-point configuration, respectively. For similar background plasma conditions, one needs 30% less NBI power ($P_{NBI}=5.3MW$ compared to $P_{NBI}=8MW$), and further away from the resonance ($v_{||NBI} \approx 0.8 v_A$ compared to $v_{||NBI} \approx 0.95 v_A$ due to a different plasma density) to destabilise TAEs with intermediate n's in plasmas with low edge magnetic shear than with high edge magnetic shear. On the other hand, for plasmas with similar low edge magnetic shear and monotonic q-profile, $P_{NBI}=5.3MW$ is not sufficient to destabilise $n=0 \div 2$ TAEs for $v_{||NBI} \approx 0.8 v_A$. This result confirms earlier predictions and measurements on the stabilising effect of edge magnetic shear for TAEs in plasmas with monotonic q-profiles. As expected, this effect appears to be weaker for radially localised $n=5 \div 7$ TAEs than for global $n=1 \div 2$ TAEs.

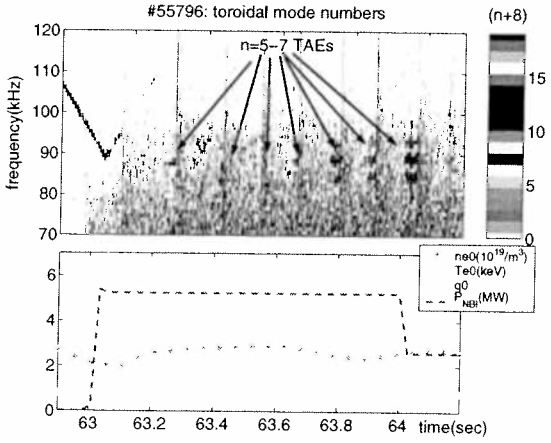

Figure 1. Limiter plasma with monotonic q-profile: $n=5 \div 7$ TAEs become unstable at $P_{NBI}=5.3MW$, with $|v_{||NBI}| \approx 0.8 v_A$.

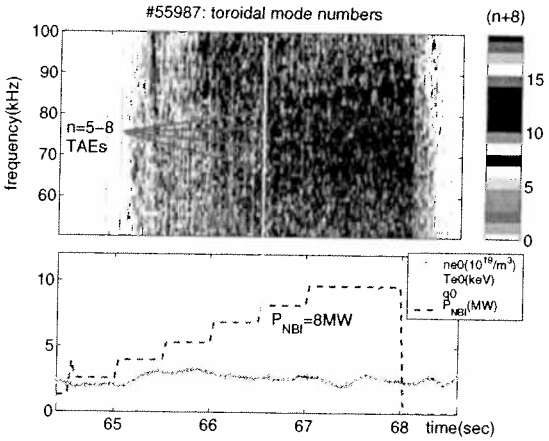

Figure 2. X-point plasma with monotonic q-profile: $n=5 \div 8$ TAEs become unstable at $P_{NBI}=8MW$, with $|v_{||NBI}| \approx 0.95 v_A$.

In X-point plasmas with high edge magnetic shear but non-monotonic q-profile and a core transport barrier, produced in the JET Reverse Shear scenario, a lower NBI power, $P_{NBI}=4.5MW$, is sufficient to destabilise $n=3 \div 5$ modes in the AE frequency range. Energy well below the MeV range (which is needed to destabilise TAEs in conventional scenarios), with $v_{||NBI} \approx 0.3 v_A$, seem to be sufficient [5]. This could be due to the coupling between kinetic and drift Alfvén waves in plasmas with a deeply non-monotonic q-profile, a high value of q_0 and negative magnetic shear in the core [6].

3. The Effect of the NBI Heating Power and Plasma β on the Frequency and Damping Rate of n=1 TAEs

One important question to address to accurately predict the TAE stability in ITER is the effect of the plasma normalised pressure, $\beta=2\mu_0 p/B^2$, on the mode frequency and damping rate [7]. Figure 3 shows the measured mode frequency and γ/ω for a n=1 TAE in #52191 during the NBI heating phase. As predicted by fluid [8] and gyrokinetic models [9], the mode frequency decreases with increasing β. We also notice a clear decrease in the damping rate when P_{NBI}, hence β, increases, up to $P_{NBI}=3 \div 4MW$. For these levels of NBI power no major changes are

observed in the plasma profiles (q, pressure, density and temperature), which maintain the characteristic L-mode shape.

Moreover, we observe a second n=1 TAE for increasing P_{NBI}, up to $P_{NBI}\approx 4MW$. These two modes are very closely spaced in frequency, $|\omega_1-\omega_2|/\omega_{TAE}\approx 0.05$, where ω_{TAE} is the centre of the TAE gap. Figures 4a and 4b show an example of this observation during the NBI phase of #52191, for $P_{NBI}=0\rightarrow 3MW$. Fluid models predict an increase of γ/ω with β for high-n AEs as the mode frequency decreases and the wavefield gets localised close to the gap. Therefore the observed decrease in γ/ω for increasing β is not consistent with these predictions. Similarly, the appearance of two n=1 TAEs very closely spaced in frequency for $2<P_{NBI}(MW)<4$ is not consistent with the prediction of a transition from a single TAE to multiple kTAEs proposed in Ref.[10].

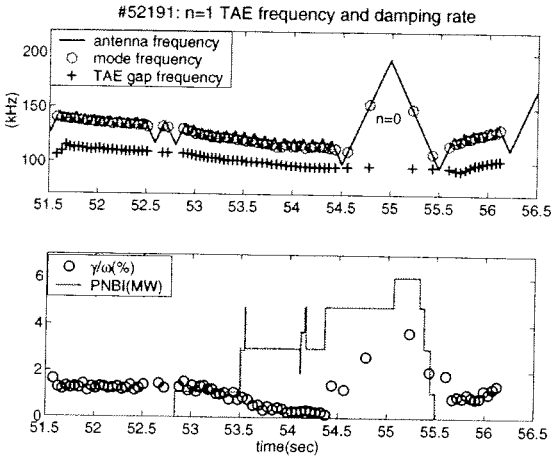

Figure 3. *The measured damping rate for a n=1 TAE during the NBI heating phase of #52191. For $P_{NBI}>2MW$ two distinct modes appear in the frequency spectrum, but only the evolution of one mode is plotted here for clarity.*

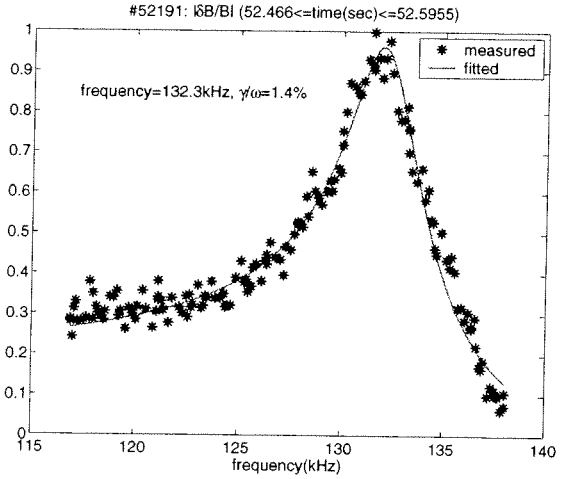

Figure 4a. *The n=1 TAE frequency spectrum before the beginning of the NBI heating phase of #52191: here one single mode is found.*

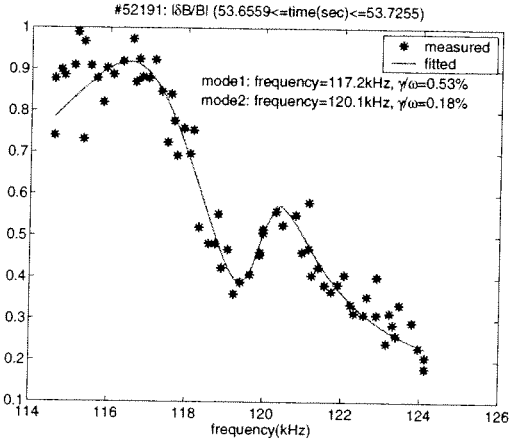

Figure 4b. *The n=1 TAE frequency spectrum during in #52191 for $P_{NBI}=3MW$: here two modes are clearly visible in the spectrum.*

The mode frequency measured during the NBI heating phase is very close to that at the centre of the toroidal gap, whereas the models reported in [10] could reproduce the observed splitting only if the mode frequency was close to that at the top of the toroidal gap. Only in such cases would the frequency separation between the two modes observed for $P_{NBI}<4MW$, be consistent with the predictions of Ref.[10]. On the other hand, the results presented in Ref.[11] show that multiple weakly damped kAEs can appear closely spaced around the n=1 TAE frequency for a fixed background plasma when the ion temperature increases from $T_{i0}=1keV$ to $T_{i0}=3keV$. This prediction could be consistent with the results presented here, but needs to be further refined because the q-profile used in the calculations is much flatter than the experimental one, and, more importantly, the measured ion temperature increase is at least a factor of two smaller than that assumed in the calculation. The effect of beam ions on the dispersion relation for the shear Alfvén wave could give rise to two modes closely spaced in

frequency [7]. By introducing in the cold plasma dielectric tensor a low-density, $n_b/n_i<<1$, sub-Alfvénic, $v_b<<v_A$, population of fast ions moving along the direction of the magnetic field, two solutions of the Alfvén wave dispersion relation are obtained pertubatively around the Alfvén frequency as $\omega_{1,2}=\omega_A(1\pm n_b v_b \Omega_i/n_i v_A \omega_A)^{1/2}=\omega_A\pm\omega_b$, with $\omega_b/\omega_A\approx 0.05$.

4. Test of the *Radiative Damping* Model for n=1 TAEs

The dependence of γ/ω for n=1 TAEs on the ion Larmor radius ρ_i has been investigated in plasmas with low magnetic shear to assess the significance of a damping mechanism resulting from the coupling between TAEs and kinetic Alfvén waves [12]. This mechanism is modelled as *radiative damping* in the kinetic code NOVA-K [13]. The radiative damping rate γ/ω_{RAD} is predicted to depend on ρ_i through the parameter $\lambda_{GAP}=4(2/5)^{3/2}(m\sigma\rho_i/r)(R/r)^{3/2}(3/4+T_e/T_i)^{1/2}$, evaluated at the gap position [13,14]. In the limit of small magnetic shear, $\sigma<<\sqrt{8}/\pi$, we have $\gamma/\omega_{RAD}=(\pi^2/8)\varepsilon_m\sigma_{GAP}{}^2 exp(-\pi^3\sigma_{GAP}{}^2/2^{7/2}\lambda_{GAP})$. Here $\varepsilon_m=5r_{GAP}/2R_{GAP}$, and R_{GAP} is the mode radial position along the major radius. In addition to the radiative damping, γ/ω_{RAD}, NOVA-K includes the Landau damping due to the trapped electrons, γ/ω_{ELE}, but does not include continuum damping [15] nor a variety of toroidal mode conversion mechanisms, which require a gyrokinetic modelling of the global wavefield [3].

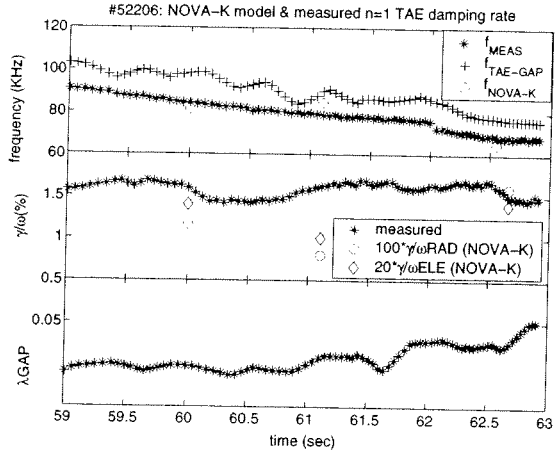

Figure 5. The measured frequency and damping rate for a n=1 TAE during the ohmic heating phase of #52206, compared with the radiative and trapped electron contribution, as computed by NOVA-K.

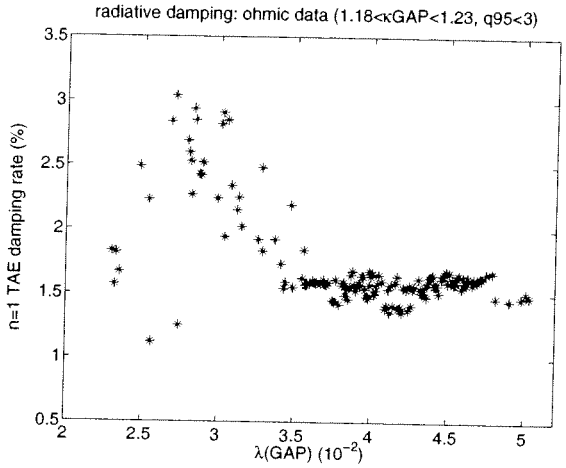

Figure 6. The dependence of the measured γ/ω for n=1 TAEs upon λ_{GAP} in the ohmic phase of the five discharges considered here: $\gamma/\omega\approx 1/\lambda$ for $2.5\leq\lambda(10^{-2})\leq 3.5$, whereas it becomes practically independent on λ at higher λ, $3.5\leq\lambda(10^{-2})\leq 5$.

Figure 5 shows the measured and computed damping rates for a m/n=2/1 TAE during the ohmic phase of a JET limiter discharge. The reduction of the mode frequency with the toroidal magnetic field is well reproduced by the NOVA-K calculation. Conversely, the computed damping rate (mainly from electron Landau damping) is about a factor 20 smaller than the measured one, with the radiative damping being even smaller.

Figure 6 show an overview of the data considered for this comparison at fixed plasma shape and magnetic shear, $q_0\approx 0.8$, $2.5\leq q_{95}\leq 3$ and $0.2\leq\sigma_{GAP}\leq 0.3$. The database covers a wide range in the electron temperature and density at the gap location, respectively $1.6\leq T_{eGAP}(keV)\leq 2.5$ and $1.5\leq n_{eGAP}(10^{19}m^{-3})\leq 2.9$, which is the origin for the observed scatter in the data. We notice the decrease in $\gamma/\omega_{MEAS}\approx 1/\lambda_{GAP}$ for $2.5\leq\lambda_{GAP}(10^{-2})\leq 3.5$, whereas γ/ω_{MEAS} becomes practically

independent on λ_{GAP} at higher λ_{GAP}, $3.5 \leq \lambda_{GAP}(10^{-2}) \leq 5$. Further work is needed to resolve the discrepancy between the theoretical damping models analysed here and the experimental results. To improve the modelling of the low-n TAE stability limits in JET, the missing damping mechanism needs to be identified for the experimental conditions reported here. To this aim, detailed comparisons with other models could be useful. Second, according to the NOVA-K predictions, the radiative damping is expected to increase with the toroidal mode number and the ion Larmor radius. Thus the radiative damping model needs to be further tested in these experimental conditions.

5. New high-n TAE antennas

The present JET Saddle Coil system can only excite low-n AEs. This system has been unique in providing large amounts of data on the frequency, damping rates and mode structure of AEs in a variety of plasma conditions. As discussed in this presentation such data is important to understand the physics of wave-particle interaction in the AE range of frequencies, and specifically to benchmark theoretical predictions for the stability of low-n AEs in ITER. However, AEs with intermediate to high mode numbers are also expected to be important in ITER. Building on the existing system, a new set of antennas to drive AEs with intermediate-n (up to $n \approx 10 \div 15$) is being designed for future installation on JET.

The authors would like to acknowledge the contribution of the whole JET experimental team, particularly T.Bolzonella, C.Giroud, T.C.Hender, F.Milani, S.D.Pinches, V.Riccardo, O.Sauter, and K.-D.Zastrow. This work has been conducted under the European Fusion Development Agreement. D.Testa and A.Fasoli were partly supported by DoE contract No. DE-FG02-99ER54563.

References

[1] A.Fasoli et al., *Phys. Rev. Lett.* **75**, 645 (1995).
[2] A.Jaun et al., *Comput. Phys. Commun.* **92** (1995), 153.
[3] A.Jaun et al., *Phys. Plasmas* **5**, 2952 (1998); A.Fasoli et al., *Phys. Lett.* **A265**, 288 (2000).
[4] D.Testa, A.Fasoli, *Nucl. Fusion* **41**, 809 (2001).
[5] A.Jaun et al., *Collective Modes and Fast Particle Confinement in ITER*, CT/P-06, this Conference.
[6] A.Jaun et al., *Plasma Phys. Contr. Fusion* **43**, 207 (2001).
[7] D.Testa et al., *Measurement of the damping rate of n=1 Toroidal Alfvén Eigenmodes as a function of the neutral beam heating power and plasma β on JET*, submitted to *Nucl. Fusion Letters*, June 2002.
[8] L.Villard et al., *Nucl. Fusion* **35**, 1173 (1995); G.Fu et al, *Phys. Plasmas* **2**, 1029 (1995); S.Sharapov et al., *Nucl. Fusion* **39**, 373 (1999).
[9] A.Jaun et al., *Nucl. Fusion* **40**, 1343 (2000).
[10] J.Candy, M.Rosenbluth, *Phys. Plasmas* **1**, 356 (1994); H.Berk et al., *Phys. Fluids* **B5**, 3969 (1993); B.Breizman, S.Sharapov, *Plasma Phys. Control. Fusion* **37**, 1057 (1995).
[11] A.Jaun et al., *Plasma Phys. Control. Fusion* **39**, 549 (1997).
[12] D.Testa et al., *Experimental test of damping models for n=1 Toroidal Alfvén Eigenmodes in JET*, submitted to *Phys. Lett. A*, September 2002.
[13] C.Cheng, *Phys. Rep.* **211**, 1 (1992); G.Fu et al., *Phys. Plasmas* **3**, 4036 (1996).
[14] S.Sharapov, *MHD Modelling of Alfvén Eigenmodes in Tokamaks*, Proceedings of the 6th Easter Plasma Meeting, Turin, 16-19 April 2000, to be published.
[15] F.Zonca, L.Chen, *Phys. Rev. Lett.* **68** (1992), 592.